Filipe Manuel Almeida Veloso

Study of ATLAS sensitivity to FCNC top quark decays

CERN-THESIS-2008-106
12/11/2008

· U  C ·

July 2008

· U  C ·

Study of ATLAS sensitivity to FCNC top quark decays

Filipe Manuel Almeida Veloso

(mestre)

Dissertação de Doutoramento em Física,
Especialidade de Física Experimental,
apresentada à Faculdade de Ciências e Tecnologia da
Universidade de Coimbra

Orientador: Professor Doutor João Carlos Lopes de Carvalho

Co-orientador: Professor Doutor António Joaquim Onofre de Abreu Ribeiro Gonçalves

Coimbra, Julho de 2008

Resumo

De acordo com o Modelo Padrão das Partículas Elementares (SM), as razões de decaimento (BR) através de correntes neutras com troca de sabor (FCNC) do *quark top*, i.e. $t \to qX, X = \gamma$, Z ou q são extremamente pequenas (10^{-14} a 10^{-12}). No entanto, existem várias extensões ao SM que prevêem valores mais elevados para estas razões de decaimento (até $\sim 10^{-4}$).

Este trabalho é dedicado ao estudo da sensiblidade da experiência ATLAS aos decaimentos FCNC do *quark top* em acontecimentos $t\bar{t}$ produzidos pelo *Large Hadron Collider* (LHC) do CERN. Foram desenvolvidas análises probabilísticas para alta ($L = 10$ fb^{-1} e $L = 100$ fb^{-1}) e baixa ($L = 1$ fb^{-1}) luminosidades, recorrendo a simulações de Monte Carlo e usando quer a simulação rápida do detector ATLAS, quer a simulação completa. Várias fontes de erros sistemáticos foram consideradas.

Para uma luminosidade integrada igual a 10 fb^{-1}, ATLAS conseguirá observar a produção dos decaimentos FCNC do *quark top*, com uma significância igual a 5σ, se as BR forem superiores a 9.4×10^{-5}, 4.4×10^{-4} ou 4.3×10^{-3}, para os canais de decaimento $t \to q\gamma$, $t \to qZ$ e $t \to qg$, respectivamente. Na ausência de sinal, poder-se-ão estabelecer, com um nível de confiança igual a 95%, os seguintes limites: 4.1×10^{-5}, 3.1×10^{-4} e 1.3×10^{-3}, para os mesmos canais. Os resultados obtidos a baixa luminosidade são compatíveis com estes valores desde que se considerem as diferenças nas luminosidades, nas eficiências de reconstrução de leptões e de fotões, nas eficiências de *trigger* e nas secções eficazes dos fundos.

Estes resultados foram comparados com outros estudos feitos anteriormente, quer para ATLAS, quer para CMS (outro detector genérico instalado no LHC). Concluiu-se que para o canal $t \to q\gamma$, os resultados são melhores do que os obtidos anteriormente por ATLAS e do que os de CMS. Os resultados para o canal $t \to qZ$ são semelhantes. Os limites esperados para estes dois canais são duas ordens de grandeza melhores que os resultados experimentais actuais. Para o canal $t \to qg$ conclui-se que, apesar de o resultado esperado ser cerca de uma ordem de grandeza melhor que o limite experimental actual, as análises baseadas na produção simples do *quark top* serão mais sensíveis.

Mesmo que o SM preveja BR muito mais pequenos que os limites obtidos, várias extensões ao SM poderão ser testadas, rejeitando-as ou reduzindo o espaço dos parâmetros.

Palavras chave

LHC, ATLAS, *quark top*, decaimentos, FCNC

Abstract

According to the Standard Model (SM), the top quark Branching Ratios (BR) through Flavour Changing Neutral Currents (FCNC), $t \to qX, X = \gamma$, Z or q are extremely small (10^{-14} to 10^{-12}). Nevertheless there are several extensions to the SM which predict higher values for these FCNC BR (up to $\sim 10^{-4}$).

This work is dedicated to the study of the ATLAS experience sensitivity for the FCNC top quark decays in $t\bar{t}$ events produced at the Large Hadron Collider (LHC) at CERN. Probabilistic analyses were developed for high ($L = 10$ fb^{-1} e $L = 100$ fb^{-1}) and low ($L = 1$ fb^{-1}) luminosities, using Monte Carlo simulations. Fast and full ATLAS simulations were used. Several sources of systematic uncertainties were studied.

With an integrated luminosity of 10 fb^{-1}, ATLAS will be able to observe FCNC top quark decays, with a 5σ significance, if these decays have a BR larger than 9.4×10^{-5}, 4.4×10^{-4} or 4.3×10^{-3}, for the $t \to q\gamma$, $t \to qZ$ e $t \to qg$ decay channels, respectively. If no signal evidence is found, the following 95% confidence level limits on the BR can be derived: 4.1×10^{-5}, 3.1×10^{-4} and 1.3×10^{-3}, for the same channels. The expected limits for low luminosity are compatible with these, if the differences in luminosities, in lepton and photon identification efficiencies, in trigger efficiencies and in background cross sections are taken into account.

These results were compared with previous analyses from ATLAS, as well from CMS (another general purpose detector at LHC). For the $t \to q\gamma$ channel, the obtained results for the BR are better than the previous ones from ATLAS, and those from CMS. For the $t \to qZ$ channel, the results are similar. The expected limits for these two channels are about two orders of magnitude better than the present experimental limits. For the $t \to qg$ the expected result is about one order of magnitude better then the current limit from Tevatron, although the results from the single top production analyses could be even better.

Even if the SM predicts much lower BR than the expected limits, some extensions of the SM can be probed, rejecting them or constraining their parameters space.

Key words

LHC, ATLAS, top quark, decays, FCNC

Acknowledgement

I would like to thank:

- my supervisors, Dr João Carvalho and Dr António Onofre, for giving me the opportunity to do this work, they were excelent supervisors as they guided me during the last four years and provided me with good advice;
- Dr Amélia Maio of the Laboratório de Instrumentação e Física Experimental de Partículas, the Team Leader of the Portuguese ATLAS group, for providing the means needed for this work, namely a grant during the early months;
- Dr Juan Antonio Aguilar Saavedra, Dr Pedro Ferreira, Dr Rui Santos and Dr Orlando Oliveira for their valuable advices;
- Dr Pedro Teixeira-Dias, who received me in the Royal Holloway, University of London, during my stay there;
- Dr Miguel Oliveira, for is help with Milipeia at LCA and the ATLAS cluster at LIP;
- my collegues, in particular to Nuno Castro, my collegue since the begining, and to Cláudio Silva, Filipa Balau, Matilde Castanheira and Rita Monteiro, for their companionship and
- my family and Margarida, for their love and support.

Part of this work has been performed in the HPC Milipeia center at the Laboratório de Computação Avançada of the University of Coimbra.

This work was also supported by Fundação para a Ciência e a Tecnologia, through the grant SFRH/BD/18762/2004 (POCI 2010 — Formação Avançada para a Ciência —- Medida IV.3)

UNIÃO EUROPEIA
Fundo Social Europeu

Ciência.Inovação 2010 Programa Operacional Ciência e Inovação 2010
MINISTÉRIO DA CIÊNCIA, TECNOLOGIA E ENSINO SUPERIOR

Contents

List of Figures

List of Tables

Introduction

The top quark was discovered by the Fermilab experiments CDF and DØ in 1995. Its discovery completed the three-generation structure of fundamental particles of the Standard Model (SM). Several properties of the top quark have already been explored by the Tevatron experiments like the mass, the charge, its lifetime, the rare decays through Flavour Changing Neutral Currents (FCNC) and the production cross-sections. The structure of the Wtb vertex and the top main decay mode within the SM ($t \to bW$) were also investigated together with the measurements of the W helicity fractions. The available centre of mass energy and the collected luminosity have not yet allowed for precise measurements of these properties, except for the mass.

At the LHC (unlike the Tevatron) the total production cross section will be dominated by the gluon fusion process which amounts to 90% of the total $t\bar{t}$ production. According to the SM, top quarks can also be significantly produced through electroweak single top production. The LHC will operate with a centre-of-mass energy of 14 TeV, and, in the $l = 10^{33}$ cm^{-2}s^{-1} luminosity phase, around 8 millions $t\bar{t}$ pairs and another few million single top events will be produced per year and experiment.

Due to its large mass, much higher than any other known fermion, the top quark is a very good laboratory to look for physics beyond the SM. FCNC are strongly suppressed in the SM due to the Glashow-Iliopoulos-Maiani mechanism. Although absent at tree level, small FCNC contributions are expected at one loop level, according to the Cabibbo-Kobayashi-Maskawa mixing matrix. In the top quark sector of the SM, these contributions limit the FCNC decay branching ratios to the gauge bosons, $BR(t \to qX, X = Z, \gamma, g)$, to less than 10^{-12}.

FCNC processes associated with the production and decay of top quarks have been studied at colliders, nevertheless the amount of top quark data collected up to now is not comparable with the statistics expected at the LHC. This work is devoted to the study of the ATLAS experiment sensitivity to top quark decays via FCNC ($t \to qX, X = \gamma, Z, g$), using $t\bar{t}$ events produced at the LHC. While one of the top quarks is expected to follow the dominant SM decay ($t \to bW$), the other decays through an FCNC channel, *i.e.*, $t \to q\gamma$, $t \to qZ$ or $t \to qg$. Cut-based analyses, followed by probabilistic type of analysis, were developed.

This thesis is organised as follows. After the theoretical introduction to the subject in Chapter 1, a description of the LHC accelerator and of the ATLAS detector is presented in Chapter 2. Chapter 3 is devoted to the studies done for the high luminosity phase (integrated luminosities of $L = 10$ fb^{-1} and $L = 100$ fb^{-1}), performed with the fast simulation of the ATLAS detector. It includes the description of the generation and the simulation of the signal and the background samples, the selection criteria applied to each FCNC channel, the obtained results and the study of the systematic uncertainties. At a later stage, these studies were also done for just $L = 1$ fb^{-1} with the full simulation and Chapter 4, which has a similar structure, is devoted to explain them. In Chapter 5, the results are compared with previously published ones. In Chapter 6 the final conclusions are presented. Throught this thesis, natural units will

be used ($\hbar = c = 1$) and, unless stated otherwise, energies, masses and momenta will be given in GeV.

1

Theoretical models

The Standard Model (SM) has a great success in the description of the available particle physics experimental data [1]. Nevertheless, there is also the conviction that it might not be complete and that it is an effective model, which is valid only at the presently accessible energies. The top quark is the heaviest of all known quarks, which makes it the more difficult to produce and the least studied one. This chapter reviews briefly the theoretical aspects most relevant to this work. Section 1.1 describes the SM, while Section 1.2 is dedicated to the top quark, focusing on its properties, decay modes and production mechanisms. At the end, the expected signal and background events for this work at the LHC are described.

1.1 The Standard model

The field theory with local symmetry breaking of the $SU(2) \times U(1)$ group, proposed by Glashow [2], Salam [3] and Weinberg [4], is known as the model of the electroweak interactions. This theory reproduces the present experimental data with great precision [1] and unifies the weak and the electromagnetic interactions. The strong interaction is described in a similar way by using the $SU(3)$ symmetry group [5]. The model which describes the electroweak and strong interactions is the one which is usually named SM of particle physics.

The SM Lagrangian is composed of different sectors,

$$\mathscr{L}_{\mathrm{SM}} = \mathscr{L}_{\mathrm{gauge}} + \mathscr{L}_{\mathrm{fermions}} + \mathscr{L}_{\mathrm{Higgs}} + \mathscr{L}_{\mathrm{Yukawa}}, \tag{1.1}$$

which are discussed below.

The Standard Model components

The particles responsible for the interactions are described by a sector with twelve vector fields, $\mathscr{L}_{\mathrm{gauge}}$. After the spontaneous symmetry breaking (see for example [6]), these fields correspond to the massive W^+ and W^- charged bosons, responsible for the charged electroweak currents, to the Z and γ neutral bosons, responsible for the neutral electroweak currents, and to the eight gluons, g_i, $i = 1, \ldots, 8$, responsible for the strong interaction.

The kinetic terms of "matter particles" are described by the fermionic sector $\mathscr{L}_{\mathrm{fermions}}$. It is known experimentally that there are different types of fermions. The ones that are sensitive to the strong force are named quarks, while the others, which are $SU(3)$ singlets, are called leptons. Several types of quarks and leptons (flavours) are known and can be grouped in

	leptons			quarks			
	electronic						
1st family	neutrino	electron		up		down	
	ν_{eL}	e_L^-	e_R^-	u_L	u_R	d_L	d_R
	muonic						
2nd family	neutrino	muon		charm		strange	
	$\nu_{\mu L}$	μ_L^-	μ_R^-	c_L	c_R	s_L	s_R
	tauonic						
3rd family	neutrino	tau		top		bottom	
	$\nu_{\tau L}$	τ_L^-	τ_R^-	t_L	t_R	b_L	b_R
T	1/2	1/2	0	1/2	0	1/2	0
T_3	1/2	−1/2	0	1/2	0	−1/2	0
Q	0	−1	−1	2/3	2/3	−1/3	−1/3
Y	−1	−1	−2	1/3	4/3	1/3	−2/3

Table 1.1: Known quarks and leptons (fermions).

families, as described in Table 1.1. The fields associated to the fermions are described in terms of the chirality components — doublets of left-handed components and singlets of right--handed components. This way, for the first family, one has:

$$\left[\begin{array}{c} \nu_e \\ e^- \end{array}\right]_L, \quad e_R, \quad \left[\begin{array}{c} u \\ d \end{array}\right]_L, \quad u_R, d_R. \tag{1.2}$$

The states from each multiplet are eigenstate of the weak isospin operator T, generator of the $SU(2)$ group. The generator corresponding to $U(1)$ is the hypercharge operator Y. The electric charge is defined as $Q = T_3 + \frac{1}{2}Y$. The quantum numbers that correspond to the known fermions are shown in Table 1.1. The SM is build with left handed neutrinos only. Therefore SM neutrinos are massless[1]. Recent results from the Super-Kamiokande [7], K2K [8], SNO [9] and KamLAND [10] collaborations show evidence for neutrino oscillation, which indicate that neutrinos are massive. This subject lays out of the scope of this thesis and will not be discussed here (for a review see, for example, [11]).

The fermionic and gauge sectors do not have mass terms, since their introduction into the Lagrangian would break the gauge invariance. Instead, the bosonic mass terms are obtained in the SM by adding new scalar fields — the Higgs sector, $\mathscr{L}_{\text{Higgs}}$, which includes the scalar kinetic terms and the Higgs potential. After the symmetry breaking, these fields originate mass terms for the $W^{\pm}$ and Z bosons and only one scalar field remains, the Higgs boson. Fermionic mass terms are obtained from the Lagrangian last sector, $\mathscr{L}_{\text{Yukawa}}$, which couples the Higgs boson to the fermions through Yukawa couplings. Due to spontaneous symmetry breaking, the mass eigenstates for quarks (the states represented in Table 1.1) are different

[1]Since neutrinos do not have the right handed helicity component, the corresponding Dirac mass term vanish. Nevertheless, considering only the left handed helicity component, if antineutrinos are identified with neutrinos (Majorana neutrinos), then neutrinos could be massive.

from the gauge states (the ones before symmetry breaking). The different quark states are related by unitary 3×3 matrices:

$$U'_L = S^U_L U_L, \quad U'_R = S^U_R U_R, \quad D'_L = S^D_L D_L, \quad D'_R = S^D_R D_R, \tag{1.3}$$

where $S^{U,D}_{L,R}$ are unitary matrices; $U = [u, c, t]$ and $D = [d, s, b]$; U' and D' represent the gauge states.

The flavour changing neutral currents

Due to the rotation between the gauge and the mass states, the charged currents are not diagonal for these states:

$$\begin{aligned} J^c_\mu &\propto \bar{u}'_L \gamma_\mu d'_L + \bar{c}'_L \gamma_\mu s'_L + \bar{t}'_L \gamma_\mu b'_L \\ &= \bar{U}'_L \gamma_\mu D'_L \\ &= \bar{U}_L \gamma_\mu S^{U\dagger}_L S^D_L D_L \\ &= \bar{U}_L \gamma_\mu V D_L \\ &= \bar{U}_L \gamma_\mu D''_L \\ &= \bar{u}_L \gamma_\mu d''_L + \bar{c}_L \gamma_\mu s''_L + \bar{t}_L \gamma_\mu b''_L, \end{aligned} \tag{1.4}$$

where $V = S^{U\dagger}_L S^D_L$ is the Cabibbo-Kobayashi-Maskawa (CKM) [12] unitary matrix, which relates the mass states with the states that diagonalize the charged currents, d'', s'', b'':

$$\begin{bmatrix} d'' \\ s'' \\ b'' \end{bmatrix} = V \begin{bmatrix} d \\ s \\ b \end{bmatrix} = \begin{bmatrix} V_{ud} & V_{us} & V_{ub} \\ V_{cd} & V_{cs} & V_{cb} \\ V_{td} & V_{ts} & V_{tb} \end{bmatrix} \begin{bmatrix} d \\ s \\ b \end{bmatrix}. \tag{1.5}$$

So, due to the CKM matrix, the charged currents allow interactions between quarks of different families. The same does not happen at tree level with the neutral currents. In fact, the neutral current J^n_μ is:

$$\begin{aligned} J^n_\mu &\propto \bar{u}' \gamma_\mu u' + \bar{c}' \gamma_\mu c' + \bar{t}' \gamma_\mu t' + \bar{d}' \gamma_\mu d' + \bar{s}' \gamma_\mu s' + \bar{b}' \gamma_\mu b' \\ &= \bar{U}' \gamma_\mu U' + D' \gamma_\mu D' \\ &= \bar{U}'_L \gamma_\mu U'_L + \bar{U}'_R \gamma_\mu U'_R + \bar{D}'_L \gamma_\mu D'_L + \bar{D}'_R \gamma_\mu D'_R \\ &= \bar{U}_L \gamma_\mu S^{U\dagger}_L S^U_L U_L + \bar{U}_R \gamma_\mu S^{U\dagger}_R S^U_R U_R + \bar{D}_L \gamma_\mu S^{D\dagger}_L S^D_L D_L + \bar{D}_R \gamma_\mu S^{D\dagger}_R S^D_R D_R \\ &= \bar{U}_L \gamma_\mu U_L + \bar{U}_R \gamma_\mu U_R + \bar{D}_L \gamma_\mu D_L + \bar{D}_R \gamma_\mu D_R \\ &= \bar{U} \gamma_\mu U + \bar{D} \gamma_\mu D \\ &= \bar{u} \gamma_\mu u + \bar{c} \gamma_\mu c + \bar{t} \gamma_\mu t + \bar{d} \gamma_\mu d + \bar{s} \gamma_\mu s + \bar{b} \gamma_\mu b, \end{aligned} \tag{1.6}$$

i.e., the flavour changing neutral currents (FCNC) are suppressed at tree level in the SM Lagrangian. At higher orders, loop contributions generate neutral currents of the type:

$$\sum_q \sum_{q' \neq q''} V_{qq'} V^*_{qq''} \bar{q}'' \left(\frac{i}{\not{p} - m_q} \right) q', \tag{1.7}$$

where $q = u, c, t$ and $q', q'' = d, s, b$. These contributions are canceled out for degenerate quark masses by the unitarity of the CKM matrix. If the quark masses are not degenerate, the

FCNC will be more suppressed for smaller mass differences. This result is known as the GIM mechanism [13] and led to the theoretical prediction of the charm quark, in a time where only the up, down and strange quarks were known.

Despite the great success achieved by the SM, it has nineteen free parameters and several issues that were not experimentally verified yet or justified: the existence of the Higgs boson, the mechanism responsible for the particles mass and its hierarchy, and the number of quark families and leptons, for example.

1.2 The top quark

The top quark is the heaviest known elementary particle. It is as heavy as the most abundant isotope of the Rhenium atom, $^{187}\mathrm{Re}_{75}$, which is a bound state of 636 light elementary particles (up and down quarks and electrons). The first indirect evidence for the top quark came from electroweak fits to data collected by several experiments, mainly from the LEP accelerator with centre-of-mass energy ($\sqrt{s}$) around the Z boson mass [14]. The top quark was discovered in 1995 by the CDF [15] and DØ [16] experiments in $p\bar{p}$ collisions ($q\bar{q} \to t\bar{t}$ and $gg \to t\bar{t}$) with $\sqrt{s} = 1.8$ TeV at the Tevatron collider, at Fermilab. The present combined value of the measured top quark mass is $m_t = 172.6 \pm 1.4$, as shown in Figure 1.1. The individual values, from different analyses and collaborations, are also shown in this figure. Due to its large mass, which is close to the electroweak symmetry breaking scale, its small lifetime (which does not allow bound-states of the top quark to be formed [17]) and to the fact that it decays almost exclusively to bW, the top quark is a very intriguing particle, which can be used to study SM predictions and probe new physics beyond the SM. A recent review about the top quark can be found in [18].

Up to present day, the top quark was observed only at the Tevatron. Apart from the top quark mass, several properties were already studied: its production cross-sections [20, 21], width [22], lifetime [23], branching ratios (BR) [24, 21] and charge [25, 26], as well as the structure of the Wtb vertex [27, 28]. Although the luminosity collected by the Tevatron experiments was enough to observe the top quark, the statistical error is the dominant contribution to the total error of these studies.

FCNC top quark decays

Figure 1.2 shows the dominant decay of the top quark, as well as the FCNC top quark decays into a photon, a Z boson and a gluon. Only the top quark decays into known particles are considered in this work, *i.e.*, decays into Higgs bosons or new supersymmetric particles will not be taken into account.

Within the Standard Model

Although absent at tree level due to the GIM mechanism, the FCNC top quark decays can occur in the SM at loop level, due to the differences between the masses of the top quark and of other quarks. The resulting branching ratios are smaller than 10^{-12} [29, 30, 31, 32], many orders of magnitude smaller than the dominant decay mode into bW, or even the sW or dW decays, which have branching ratios of $\sim 1.6 \times 10^{-3}$ and $\sim 1 \times 10^{-4}$ [33], respectively.

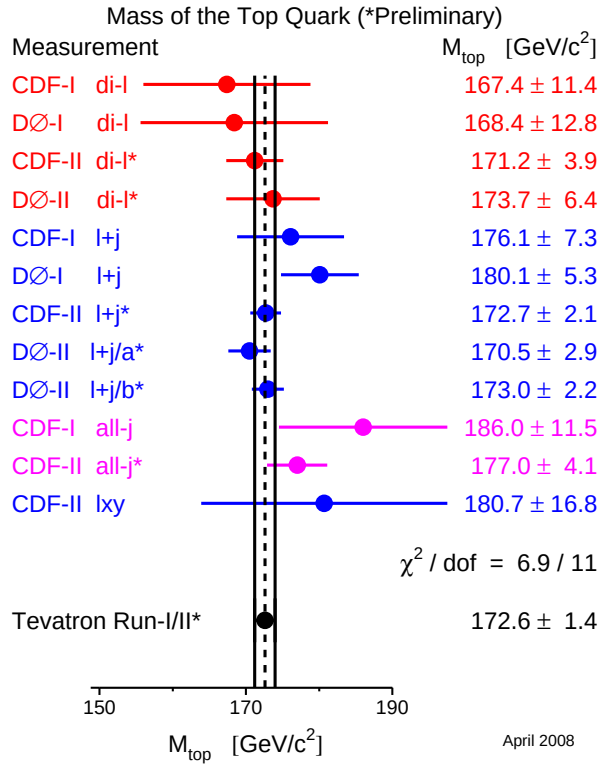

Figure 1.1: Summary of the Tevatron top quark mass measurements and combined results (Taken from [19]).

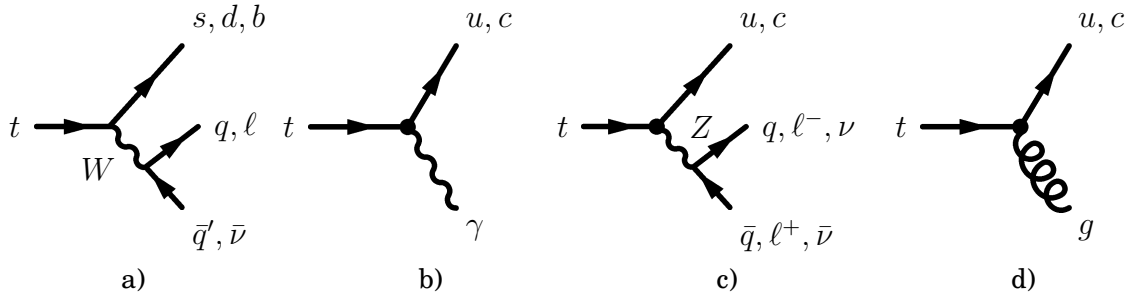

Figure 1.2: Top quark decays: a) the dominant SM decay channel $t \to bW$ and the FCNC channels b) $t \to q\gamma$, c) $t \to qZ$ and d) $t \to qg$, with $q = u, c$. The subsequent W and Z boson decays into leptons or quarks are also represented.

Process	SM	QS	2HDM	FC 2HDM	MSSM	$\not{R}$ SUSY	TC2
$t \to u\gamma$	3.7×10^{-16}	7.5×10^{-9}	—	—	2×10^{-6}	1×10^{-6}	—
$t \to uZ$	8×10^{-17}	1.1×10^{-4}	—	—	2×10^{-6}	3×10^{-5}	—
$t \to ug$	3.7×10^{-14}	1.5×10^{-7}	—	—	8×10^{-5}	2×10^{-4}	—
$t \to c\gamma$	4.6×10^{-14}	7.5×10^{-9}	$\sim 10^{-6}$	$\sim 10^{-9}$	2×10^{-6}	1×10^{-6}	$\sim 10^{-6}$
$t \to cZ$	1×10^{-14}	1.1×10^{-4}	$\sim 10^{-7}$	$\sim 10^{-10}$	2×10^{-6}	3×10^{-5}	$\sim 10^{-4}$
$t \to cg$	4.6×10^{-12}	1.5×10^{-7}	$\sim 10^{-4}$	$\sim 10^{-8}$	8×10^{-5}	2×10^{-4}	$\sim 10^{-4}$

Table 1.2: The maximum values for the branching ratios of the FCNC top quark decays, predicted by the SM, the quark-singlet model (QS), the two-Higgs doublet model (2HDM), the flavour-conserving two-Higgs doublet model (FC 2HDM), the minimal supersymmetric model (MSSM), SUSY with R-parity violation and Topcolour-assisted Technicolour model (TC2) are shown. (Adapted from [34])

Beyond the Standard Model

There are, however, several extensions to the SM that predict the presence of FCNC contributions already at tree level, and which significantly enhance the FCNC decay branching ratios, as compared to the SM predictions [34]. Table 1.2 shows the maximum values for the branching ratios for different SM extensions and for the SM itself.

In models with exotic (vector-like) quarks [32, 35, 36], the three family CKM matrix loses unitarity and, if the new quarks have a charge $2/3|e|$ and are $SU(2)_L$ singlets, the Z neutral currents involving up-type quarks become non-diagonal. The GIM mechanism is thus weakened and the FCNC top quark decays to a Z boson becomes possible at tree level, which gives new contributions at loop level for the other decays (into an up-type quark plus a photon or a gluon). The FCNC top quark BR increase to about 7.5×10^{-9}, 1.1×10^{-4} and 1.5×10^{-7} for the $t \to q\gamma$, $t \to qZ$ and $t \to qg$ decay channels (with $q = u, c$), respectively.

Extensions of the SM like two-Higgs doublet models (2HDM) [37, 38, 39, 40, 41, 42], are characterised by the existence of two complex scalar fields, which after the symmetry breaking originate two neutral CP-even (h,H), one CP-odd (A) and one pair of charged ($H^{\pm}$) Higgs bosons. There are three types of 2HDM models, which depend on the couplings between the Higgs bosons and the fermions. In type I, the fermions couple to only one of the doublets, in type II, down-type quarks and charged leptons couple to one doublet and the other fermions couple to the other doublet, while in type III fermions couple to both doublets. Types I and II impose a symmetry which forbids FCNC at tree level. Nevertheless, the FCNC at loop level are enhanced by charged and neutral Higgs bosons contributions. These models are also called Flavour Conserving 2HDM (FC 2HDM). In type III such restriction does not exist and the resulting FCNC BR are larger.

Supersymmetry (SUSY) is a SM extension that relates fermions to bosons: for each known fermion there is a new, yet undiscovered, boson and in the same way, for each boson there is also a new fermion. SUSY must be a broken symmetry, otherwise the known particles and the corresponding new ones (called superpartners) would have the same mass. R-parity, a new quantum number, is defined in SUSY as $R = (-1)^{3(B-L)+2S}$, where B, L and S are the baryon number, the lepton number and the spin, respectively. The minimal supersymmetric model (MSSM) [43, 44, 45, 46, 47, 48, 49] has two Higgs-doublets, which is the smallest

number required to generate fermion masses with a supersymmetric Yukawa interaction, and conserves R-parity. In MSSM, the new SUSY particles, in particular gluinos (the SUSY partners of gluons), induce new contributions for the $t \to q\gamma$, $t \to qZ$ and $t \to qg$ FCNC decays at loop level. The corresponding BR are about 2×10^{-6}, 2×10^{-6} and 8×10^{-5}, respectively. In SUSY models with R parity violation [50, 51] new baryon number violating interactions arise and the FCNC BR can increase by about one order of magnitude.

The Topcolour-assisted Technicolour (TC2) model [52] relates the top quark to the electroweak symmetry breaking. New particles, three top-pions (Π_t^0, Π_t^+ and Π_t^-) and one top-Higgs (h_t), are predicted. The topcolour interactions are not universal, therefore the GIM mechanism is relaxed and new FCNC couplings are introduced. At the loop level, the BR for the $t \to c\gamma$, $t \to cZ$ and $t \to cg$ can increase up to about 10^{-6}, 10^{-4} and 10^{-4}, respectively.

Even if the LHC does not measure the top quark FCNC BR, it can test some of these models or constrain their parameters space, since any evidence for FCNC top quark decays has to be regarded as coming from physics process beyond the SM.

Effective model

A more general, model independent approach to top quark FCNC decays can be done introducing an effective Lagrangian [53, 54, 33]:

$$\begin{aligned}\mathscr{L}_4 &= -g_s\bar{t}\gamma^\mu T^a t G_\mu^a - \frac{g}{\sqrt{2}}\sum_{q=d,s,b}\bar{t}\gamma^\mu(v_{tq}^W - a_{tq}^W\gamma_5)qW_\mu^+ \\ &\quad -\frac{2}{3}e\bar{t}\gamma^\mu t A_\mu - \frac{g}{2\cos\theta_W}\sum_{q=u,c,t}\bar{t}\gamma^\mu(v_{tq}^Z - a_{tq}^Z\gamma_5)qZ_\mu \end{aligned} \tag{1.8}$$

$$\begin{aligned}\mathscr{L}_5 &= -g_s\sum_{q=u,c,t}\frac{\kappa_{tq}^g}{\Lambda}\bar{t}\sigma^{\mu\nu}T^a(f_{tq}^g + ih_{tq}^g\gamma_5)qG_{\mu\nu}^a - \frac{g}{\sqrt{2}}\sum_{q=d,s,b}\frac{\kappa_{tq}^W}{\Lambda}\bar{t}\sigma^{\mu\nu}(f_{tq}^W + ih_{tq}^W\gamma_5)qW_{\mu\nu}^+ \\ &\quad -e\sum_{q=u,c,t}\frac{\kappa_{tq}^\gamma}{\Lambda}\bar{t}\sigma^{\mu\nu}(f_{tq}^\gamma + ih_{tq}^\gamma\gamma_5)qA_{\mu\nu} - \frac{g}{2\cos\theta_W}\sum_{q=u,c,t}\frac{\kappa_{tq}^Z}{\Lambda}\bar{t}\sigma^{\mu\nu}(f_{tq}^Z + ih_{tq}^Z\gamma_5)qZ_{\mu\nu} \end{aligned} \tag{1.9}$$

plus the hermitian conjugate operators for the flavour changing terms, where $\mathscr{L}_4$ ($\mathscr{L}_5$) represents the dimension 4 (5) top quark interactions, T^a are the Gell-Mann matrices and f, h are complex numbers satisfying, for each term, $|f|^2 + |h|^2 = 1$. The FCNC top quark decays, can be expressed in terms of the κ_{tq}^g, κ_{tq}^γ, $(|v_{tq}^Z|^2 + |a_{tq}^Z|^2)$ and κ_{tq}^Z anomalous couplings to the g, γ and Z bosons respectively [33]:

$$\Gamma(t \to qg) = \left(\frac{\kappa_{tq}^g}{\Lambda}\right)^2 \frac{8}{3}\alpha_s m_t^3, \tag{1.10}$$

$$\Gamma(t \to q\gamma) = \left(\frac{\kappa_{tq}^\gamma}{\Lambda}\right)^2 2\alpha m_t^3, \tag{1.11}$$

$$\Gamma(t \to qZ)_\gamma = \left(|v_{tq}^Z|^2 + |a_{tq}^Z|^2\right)\alpha m_t^3 \frac{1}{4m_Z^2\sin^2 2\theta_W} \times \left(1 - \frac{m_Z^2}{m_t^2}\right)^2\left(1 + 2\frac{m_Z^2}{m_t^2}\right) \text{ and} \tag{1.12}$$

$$\Gamma(t \to qZ)_\sigma = \left(\frac{\kappa_{tq}^Z}{\Lambda}\right)^2 \alpha\, m_t^3 \frac{1}{\sin^2 2\theta_W} \times \left(1 - \frac{m_Z^2}{m_t^2}\right)^2\left(2 + \frac{m_Z^2}{m_t^2}\right). \tag{1.13}$$

	LEP	HERA	Tevatron
$Br(t \to qZ)$	7.8% [55, 56, 57, 58, 59]	49% [60]	3.7% [61]
$Br(t \to q\gamma)$	2.4% [55, 56, 57, 58, 59]	0.75% [60]	3.2% [62]
$Br(t \to qg)$	17% [33]	13% [63, 64, 60]	$0.1 - 1$ % (estimated from [65, 63])

Table 1.3: Present experimental limits on the branching ratios of the FCNC top quark decays channels.

The energy scale associated with this new physics is represented by Λ, while α_s and α are, respectively, the strong and electromagnetic coupling constants. The electroweak mixing angle is represented by θ_W and the top quark and Z boson masses are represented, respectively, by m_t and m_Z.

Present experimental limits

FCNC processes associated with the production and decay of top quarks have been studied at colliders and the current direct limits on the branching ratios are shown in Table 1.3. The statistics of top quark relevant data collected up to now are not comparable with the ones expected at the LHC.

Production of top quarks at the LHC

The LHC was designed to collide protons at $\sqrt{s} = 14$ TeV and to deliver an unprecedented luminosity to its experiments. It will be, for these reasons, a top quark factory and the ideal place to study the top quark properties. At the LHC, the top quark will be produced mainly in particle-anti-particle pairs and through electroweak single top production. The corresponding lowest order Feynman diagrams are shown in Figures 1.3 and 1.4.

Parton Distribution Functions

In order to compute the LHC cross-sections of these processes, it is necessary to convolute the partonic cross-sections with the probabilities of obtaining the quarks and the gluons from the colliding protons. Considering that the protons are made of partons (quarks and gluons) and its composition can be described by structure functions [66], then the Parton Density Functions (PDF) describe the distribution of the proton momentum fraction x carried by the partons, as a function of Q^2, the squared four-momentum transfer carried by the exchanged boson in

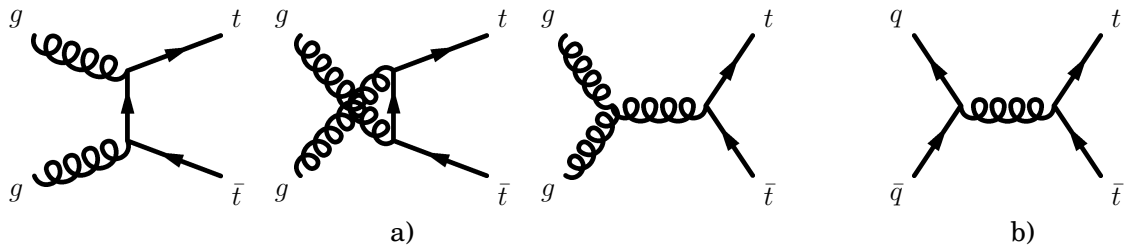

Figure 1.3: Lowest order Feynman diagrams for $t\bar{t}$ production at LHC: a) $gg \to t\bar{t}$ and b) $q\bar{q} \to t\bar{t}$.

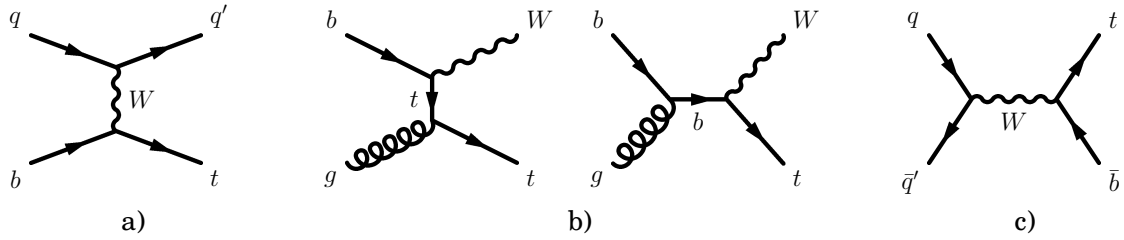

Figure 1.4: Lowest order Feynman diagrams for single top quark production at LHC: a) t-channel b) Wt associated production and c) s-channel processes.

the scattering process. The PDF are evaluated through the measurement of deep-inelastic scattering and jet production at colliders [67], since they cannot be calculated perturbatively. HERA data was acquired and fitted by the ZEUS and H1 experiments to extract parton densities at low x, the region dominated by the gluons [68, 69]. Figure 1.5 shows PDF sets evaluated by the CTEQ Collaboration [70], which include data from HERA and Tevatron.

Pair production

The expected next-to-leading-order (NLO) cross-section for top pair production, including next-to-leading logarithm (NLL) soft gluon resummation, is 833±100 pb [71, 33], for m_t = 175 GeV and $\sqrt{s}$ = 14 TeV. The total uncertainty, coming from the renormalisation and factorisation scales and PDF dependence, is 12% [33]. The gluon fusion process corresponds to about 90% of the NLO cross-section, while the quark-anti-quark annihilation process correspond to about 10%. Updated predictions for the cross-section [72, 73, 74] give compatible values within

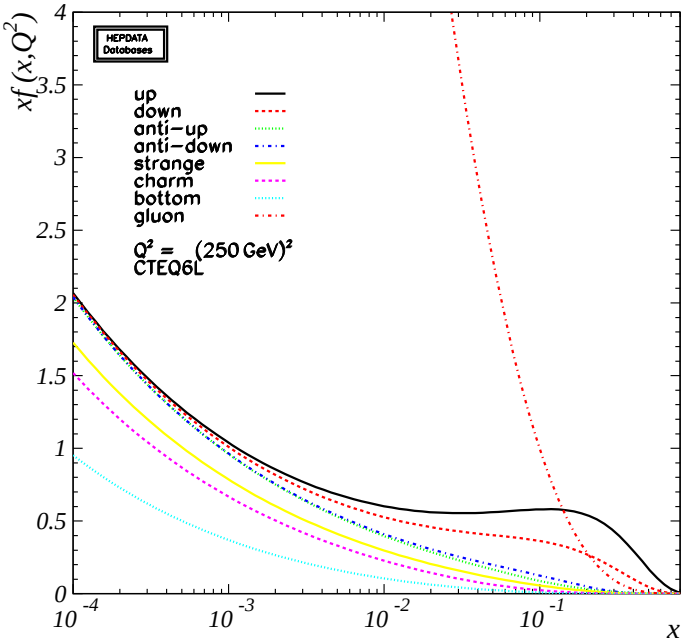

Figure 1.5: The CTEQ 6L PDF set distributions evaluated by the CTEQ Collaboration for $Q^2 = (250\ \text{GeV})^2$.

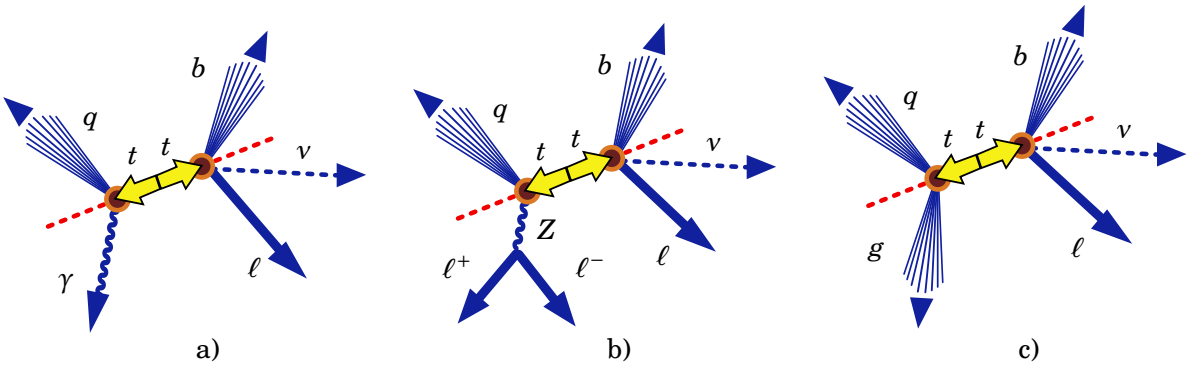

Figure 1.6: Representation of the final state topologies for the signal events of the: a) $t \to q\gamma$, b) $t \to qZ$ and c) $t \to qg$ channels. Initial and final state radiations are not represented.

errors.

Single top quark production

The single top quark production occurs through the t-channel, the Wt associated production and the s-channel processes, which have NLO cross-sections values of 245±12 pb [75], 66±2 pb [76] and 11±1 pb [75], respectively. Therefore the total NLO cross-section for single top production at the LHC is 322±12 pb.

1.3 Expected signals and backgrounds at the LHC

The top quark pair production, in which one of the top quarks decays through the dominant SM channel ($t \to bW$) and the other through FCNC channel ($t \to q\gamma$, $t \to qZ$ or $t \to qg$), is considered as signal. Figure 1.6 shows schematic representations of the signal event topologies. For each event, the quarks and gluons of the final state will not be observed directly due to colour confinement [77]. Instead, they will produce hadrons, through a non-perturbative process called hadronization. It is simulated using Monte Carlo (MC) methods based on phenomenological models [78] like, for example, the cluster [79, 80] or the string [81] models. The produced particles will be grouped in a hadronic jet. Therefore, signal events are characterised by a certain number of jets, isolated leptons and isolated photons, which depend on the produced neutral boson and on the decay channels of the W and Z bosons.

Figure 1.7 shows the cross-sections of the dominant processes expected at the LHC as a function of the centre-of-mass energy. For $\sqrt{s} < 4$ TeV, a $p\bar{p}$ collider is considered, like the Tevatron, while for $\sqrt{s} > 4$ TeV, it is a pp collider, as for example the LHC. For this reason a discontinuity is observed for 4 TeV. As can be seen in this plot, the production cross-sections expected at LHC are larger than those at Tevatron (up to two orders of magnitude). Due to Initial State Radiation (ISR), Final State Radiation (FSR), particle conversions or detection effects, these processes can have topologies similar to those of the signal. Thus the $t\bar{t}$ production (in which both top quarks decay via SM), single top quark production (again with the SM decay of the top quark), W+jets and Z+jets production, diboson production (WW, WZ and ZZ, refered also as WZ pairs) and QCD production will be background to the analyses presented here.

In order to improve the signal to background ratio due to the overwhelming QCD backgrounds, only the signal events in which the W (and Z) boson decays to charged leptons were

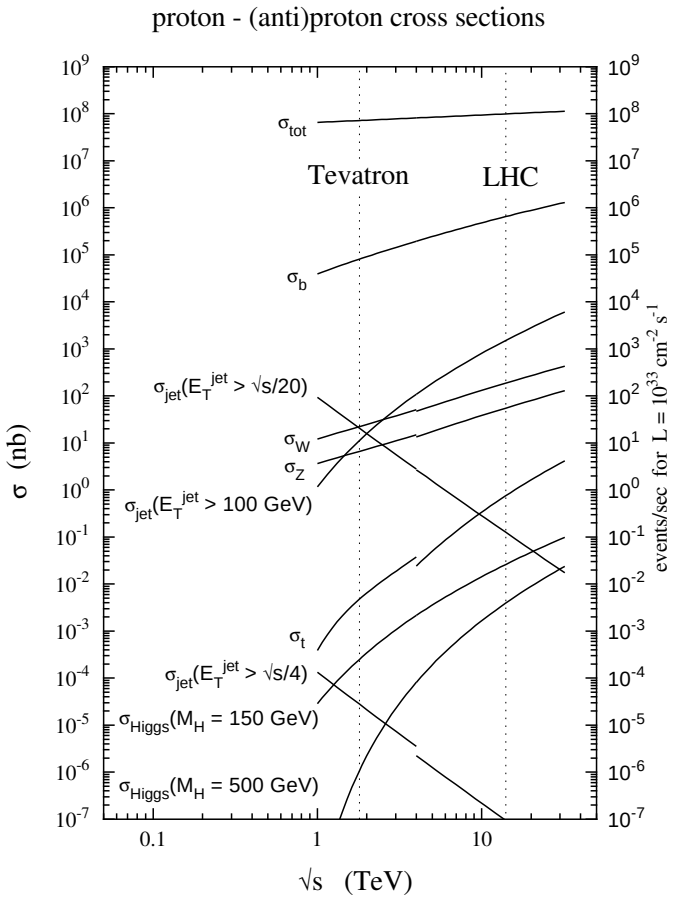

Figure 1.7: Expected cross-sections for the dominant processes at the Tevatron and LHC colliders, as a function of the centre-of-mass energy. (Taken from [82])

considered.

2

The LHC and the ATLAS detector

This chapter is dedicated to the description of the LHC and of the ATLAS detector, focusing in the LHC acceleration network, the ATLAS subdetectors, the trigger and the data acquisition systems.

2.1 Large Hadron Collider

The Large Hadron Collider (LHC) [83, 84, 85] is being installed by the European Organization for Nuclear Research (CERN) and it is predicted to start operation by September 2008. CERN is located between the French and Swiss borders, near Geneva. A detailed description of the LHC can be found in [83, 84, 85].

The LHC is physically installed in a 27 km long circular tunnel and will accelerate proton bunches in both directions. The LHC will also accelerate heavy-ion bunches, but that is beyond the scope of this thesis. Figures 2.1 and 2.2 show schematic views of the LHC and of the accelerator chain. The bunches will be produced by the Linac2 and accelerated to 7 GeV by the chain Proton Synchrotron Booster (PSB), Proton Synchrotron (PS), Super Proton Synchrotron (SPS) and LHC. The beams collide at four interaction points, where particle detectors are installed. These are the ATLAS detector in point 1, the ALICE detector in point 2, the CMS detector in point 5 and the LHCb detector in point 8. The design luminosity is $l = 10^{34}$ cm^{-2}s^{-1}, which corresponds to an integrated luminosity of about $L = 100$ fb^{-1} per year of operation. The bunch crossing time will be 25 ns. About twenty collisions are expected per bunch crossing. During the first data taking period, the expected luminosity will be one order of magnitude smaller. Relevant LHC parameters are shown in Table 2.1.

The proton bunches will be defleted by 1232 dipoles (in the curved LHC section) and focused by 392 quadrupoles (in the straight sections) magnets made of super-conducting Nb-Ti. These magnets will operate at 1.9 K, use super-fluid He, and reach a magnetic field of 8 T. Figure 2.3 shows a diagram with a cross-section of one of the LHC dipoles.

2.2 ATLAS

In order to characterise the final state of the events under study, it is necessary to use an hermetic detector able to measure the properties of the final state particles, allowing for their identification. For this purpose, the ATLAS (acronym for A Toroidal LHC ApparatuS) detector [86, 87] is, like almost all the other high energy physics detectors, a set of cylindric

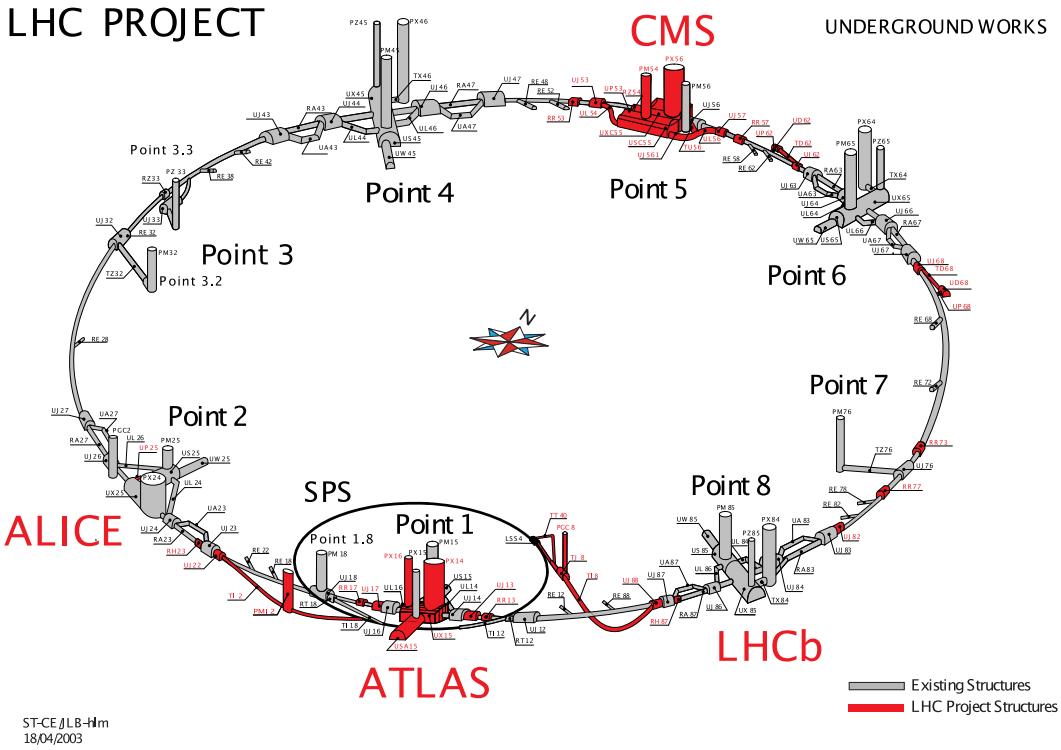

Figure 2.1: The LHC accelerator. (Adapted from [84])

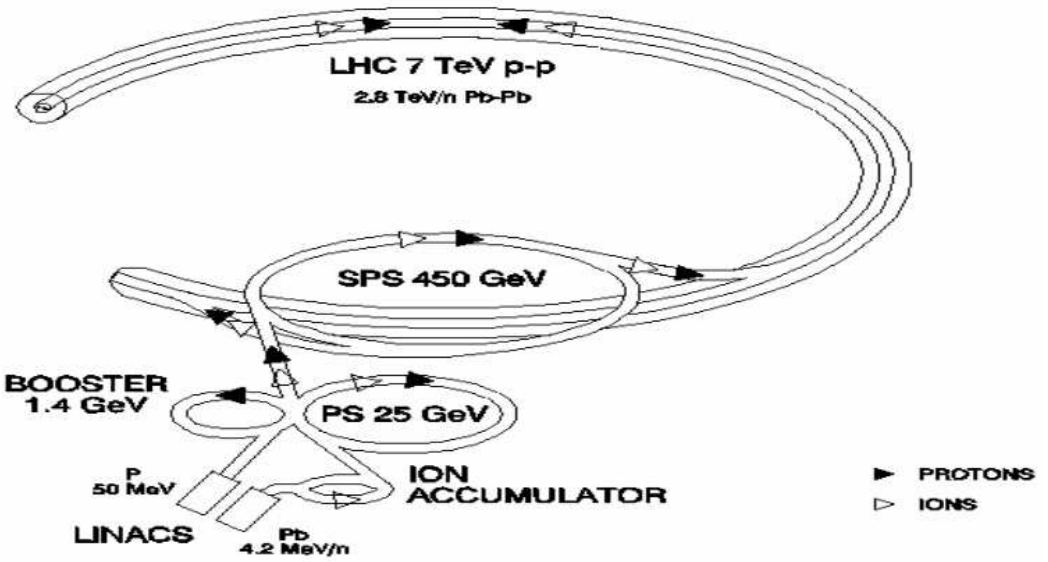

Figure 2.2: The LHC accelerator chain. (Taken from [85])

	Injection	Collision
Beam data:		
Proton energy	450 GeV	7000 GeV
Relativistic gamma	479.6	7461
Number of particles per bunch	1.15×10^{11}	
Number of bunches	2808	
Circulating beam current	0.582 A	
Stored energy per beam	23.3 MJ	362 MJ
Peak luminosity related data:		
RMS bunch length	11.24 cm	7.55 cm
RMS beam size at the IP1 and IP5	375.2 μm	16.7 μm
RMS beam size at the IP2 and IP8	279.6 μm	70.9 μm
Peak luminosity in IP1 and IP5	—	1.0×10^{34} cm^{-2}s^{-1}
Peak luminosity per bunch crossing in IP1 and IP5	—	3.56×10^{30} cm^{-2}s^{-1}
Total beam and luminosity lifetimes:		
Luminosity lifetime (due to beam-beam)	—	29.1 h
Beam lifetime (due to rest-gas scattering)	100 h	100 h
Beam current lifetime (beam-beam, rest-gas)	—	18.4 h
Luminosity lifetime (beam-beam, rest-gas, IBS)	—	14.9 h

Table 2.1: Relevant LHC parameters. (Adapted from [83])

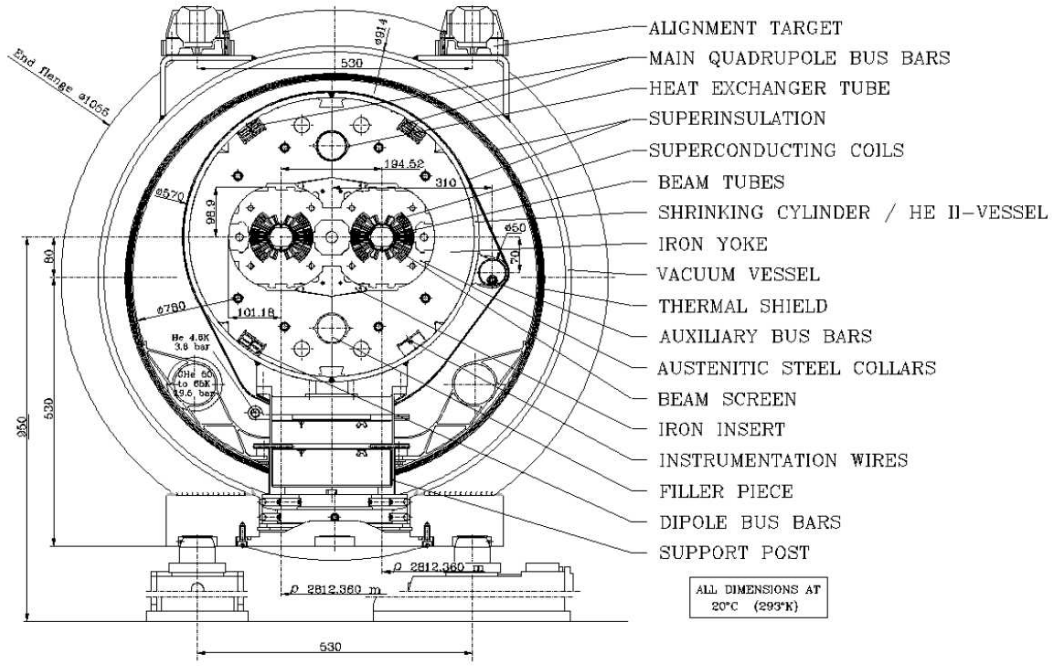

Figure 2.3: Cross-section of one of the LHC dipoles. (Taken from [83])

sub-detectors, which covers almost the full solid angle around the interaction point. The basic detector shape, which has a forward-backward symmetry with respect to the interaction point at the center, is completed by two end-caps in the bases of the cylinder. The sub-detectors of the end-caps are disc shaped, centred in the beam pipe. A schematic representation of the ATLAS detector can be seen in Figure 2.4. The detector weights seven kilotonnes and its overall dimensions are twenty two metres high and forty two metres wide. For detailed descriptions of the ATLAS detector see [86, 87].

Figure 2.5 shows the coordinate system used at ATLAS. It is a right-handed orthonormal reference system with origin in the interaction point and defined in such a way that the x-axis points to the centre of the LHC, the y-axis points to the surface and the z-axis points to LHC Point 8. As usual, ϕ is the azimuthal angle, which is measured in relation to the x axis and ranges between $-\pi$ and $+\pi$. The polar angle θ is the angle from the positive z axis and varies from 0 to π . The pseudorapidity η is related to θ by the following expression:

$$\eta = -\ln\left(\tan\left(\frac{\theta}{2}\right)\right). \tag{2.1}$$

The xy plane is called the transverse plane and the quantities such as the transverse momentum (p_T) or the transverse energy (E_T) are measured with respect to this plane. The ΔR distance is defined as

$$\Delta R = \sqrt{\Delta\eta^2 + \Delta\phi^2}. \tag{2.2}$$

The main sub-detector systems of ATLAS are:

- the magnet system, which curves the charged particles so their momenta can be measured,

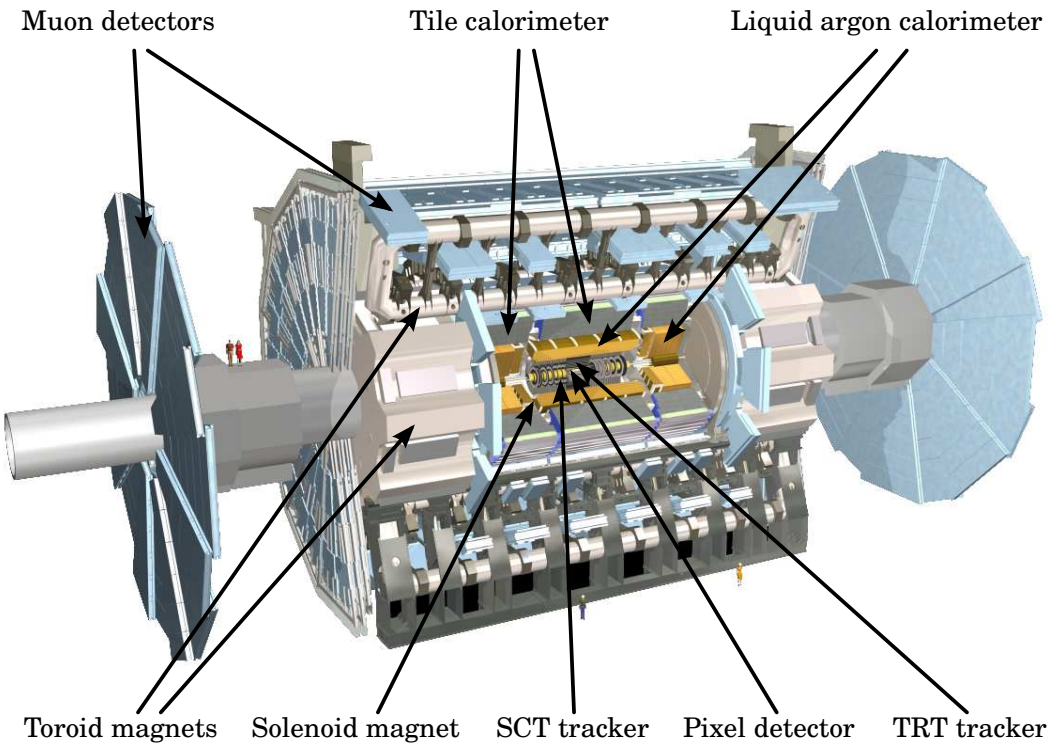

Figure 2.4: The ATLAS detector. (Adapted from [87])

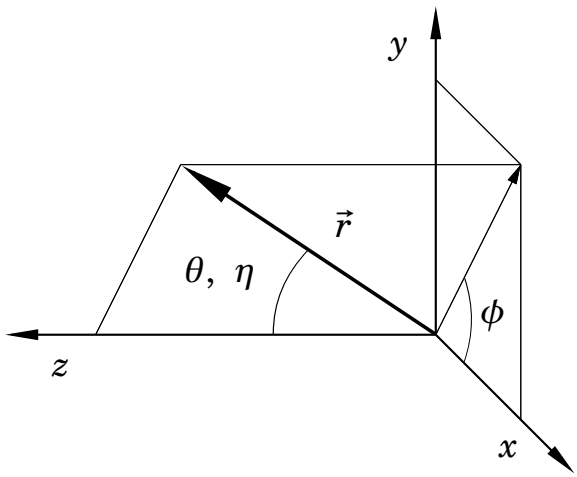

Figure 2.5: The ATLAS Coordinate System. See text for details.

Detector component	Required resolution	η coverage	
		Measurement	Trigger
Tracking	$\sigma_{p_T}/p_T = 0.05\%\ p_T \oplus 1\%$	± 2.5	
EM calorimetry	$\sigma_E/E = 10\%/\sqrt{E} \oplus 0.7\%$	± 3.2	± 2.5
Hadronic calorimetry (jets)			
barrel and end-cap	$\sigma_E/E = 50\%/\sqrt{E} \oplus 3\%$	± 3.2	± 3.2
forward	$\sigma_E/E = 100\%/\sqrt{E} \oplus 10\%$	$3.1 < \lvert\eta\rvert < 4.9$	$3.1 < \lvert\eta\rvert < 4.9$
Muon spectrometer	$\sigma_{p_T}/p_T = 10\%$ at $p_T = 1$ TeV	± 2.7	± 2.4

Table 2.2: General ATLAS detector performance goals. (Taken from [87])

- the tracking system, that identifies the passage of charged particles through the detector and measures their momenta,
- the calorimeter system, to measure the energy of particles and
- the muon system, a dedicated tracking system to identify muons.

The general ATLAS detector performance goals are summarised in Table 2.2. It should be noted that the muon system performance shown in this table is independent of the tracking system, for high p_T muons.

2.3 Magnet system

ATLAS has two magnet systems, whose geometries were responsible for the design of the rest of the detector. Figure 2.6 shows this geometry.

The system closer to the beam pipe is a solenoid, which creates a 2 T axial magnetic field in the region were the tracking system is installed. The solenoid has a inner diameter of 2.46 m, a outer diameter of 2.56 m and is 5.8 m long.

The other magnet system is composed of three toroids, one in the barrel zone of the detector, and the other two in each end-cap. Each toroid is composed of eight super-conducting coils, aligned radially and symmetrically around the beam pipe. The end-caps toroids are rotated by 22.5° in relation to the barrel toroid. In this way the magnetic fields overlap. This system provides a toroidal magnetic field of about 0.5 T, for the muon detectors in the barrel region, and of about 1 T, for the muon detectors at the end-caps. The barrel toroid is 25.3 m long and the inner diameter is 9.4 m, while the outer one is 20.1 m.

The main parameters of the ATLAS magnet system are summarised in Table 2.3. Both magnet systems will operate at 4.5 K and will be cooled down with liquid helium.

2.4 Tracking system

The ATLAS tracking system is named Inner Detector (ID) and is composed of three different sub-detectors, which are close to the interaction point. Starting from the inner to the outer, they are: the pixel detector, the semiconductor tracker (SCT) and the transition radiation tracker (TRT). The main purpose of this system is to identify the passage and trajectories of charged particles. Since the ID is submerged in a magnetic field of 2 T, the trajectories of

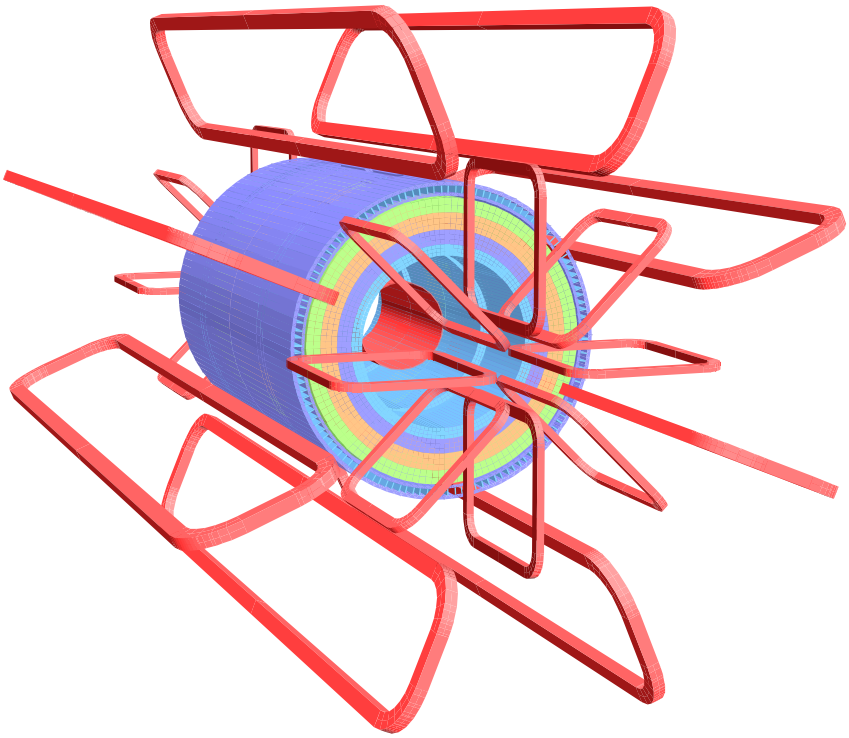

Figure 2.6: Geometry of magnet windings and tile calorimeter steel. The eight barrel toroid coils, with the end-cap coils interleaved are visible. The solenoid winding lies inside the calorimeter volume. The tile calorimeter is modelled by four layers with different magnetic properties, plus an outside return yoke. For the sake of clarity the forward shielding disk is not displayed. (Taken from [87])

Properties and features	Unit	Solenoid	Barred toroid	End-cap toroids
Size:				
Inner diameter	m	2.46	9.4	1.65
Outer diameter	m	2.63	20.1	10.7
Axial length	m	5.29 (cold)	25.3	5.0
Number of coils		1	8	2×8
Mass:				
Conductor	t	3.8	118	2×20.5
Cold mass	t	5.4	370	2×140
Total assembly	t	5.7	830	2×239
Coils:				
Turns per coil		1154	120	116
Nominal current	kA	7.73	20.5	20.5
Magnet stored energy	GJ	0.04	1.08	2×0.25
Peak field	T	2.6	3.9	4.1
Field range	T	0.9–2.0	0.2–2.5	0.2–3.5
Conductor:				
Overall size	mm^2	30×4.25	57×12	41×12
Ratio Al:Cu:NbTi		15.6:0.9:1	28:1.3:1	19:1.3:1
Number of strands (NbTi)		12	38	40
Strand diameter (NbTi)	mm	1.22	1.3	1.3
Critical current (at 5 T and 4.2 K)	kA	20.4	58	60
Critical current margin at 4.5 K	%	20	30	30
Residual resistivity ratio for Al		> 400	> 800	> 800
Temperature margin	K	2.7	1.9	1.9
Number of units × length	m	1×9100	$8 \times 4 \times 1730$	$2 \times 8 \times 2 \times 800$
Total length (produced)	km	10	56	2×13
Heat load:				
At 4.5 K	W	130	990	330
At 60–80 K	kW	0.5	7.4	1.7
Liquid helium mass flow	g/s	7	410	280

Table 2.3: Main parameters of the ATLAS magnet systems. (Taken from [87])

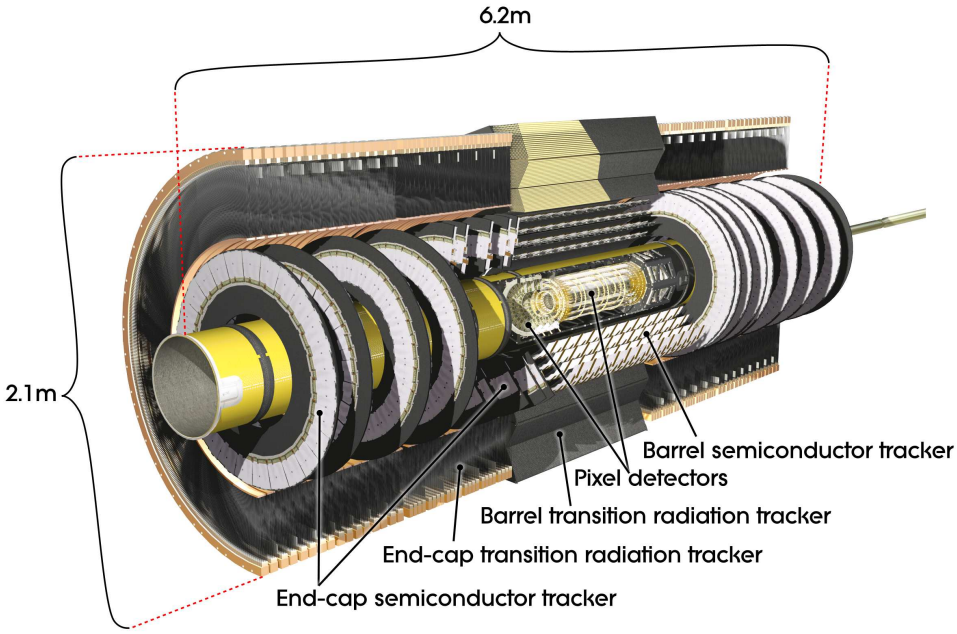

Figure 2.7: Cut-away view of the ATLAS inner detector. (Taken from [87])

these particles are deflected, which makes possible the measurement of their momenta. Figure 2.7 shows a diagram of the ID. Its main parameters are shown in Table 2.4. The total length of the ID is 3512 mm and its radius is 1150 mm.

The pixel detector covers the region defined by $|\eta| < 2.5$, is made of silicon wafers with very small pixel sensors (R–$\phi \times z = 50 \times 400$ μm^2) and achieve the highest granularity of the ATLAS detector. Three concentric cylindric layers are disposed in the central region, while 5 circular layers are placed in each end-cap region. The intrinsic accuracies are 10 μm in (R–ϕ) and 115 μm (in z) in the barrel and 10 μm (in R–ϕ) and 115 μm (in R) in the end-caps. There are about 80.4 million readout channels in the pixel detector.

The SCT is made of semiconductor strips. When charged particles cross these strips, they radiate electrons, which, in turn, due to the presence of an electric field, drift to the edge of the strips, where the anodes are located. The strips are arranged in 8 layers, which can give information of four space points for each track. The strips are joined in pairs with angles of 40 mrad in order to measure both R–ϕ coordinates. The intrinsic accuracies per module in the barrel are 17 μm and 580 μm, for R–ϕ and z respectively. In the disks they are 17 μm and 580 μm, for R–ϕ and R respectively. The SCT has about 6.3 million readout channels.

The last tracking sub-detector of the ID is the TRT. It consists of 4 mm diameter straw tubes and provides 36 hits per track with information on R–ϕ. The accuracy is of 130 μm per straw. The length of the straws is 144 cm in the barrel zone and 37 cm in the end-caps. The total number of readout channels in this sub-detector is about 351 thousand. The TRT will also be used to distinguish electrons from pions.

System and position	Area (m^2)	Resolution σ (μm)	Channels (10^6)	η coverage
Pixels:				
1 removable barrel layer (B-layer)	0.2	$R\phi = 12, z = 66$	16	± 2.5
2 barrel layers	1.4	$R\phi = 12, z = 66$	81	± 1.7
5 end-cap disks on each side	0.7	$R\phi = 12, z = 77$	43	1.7–2.5
Silicon strips:				
4 barrel layers	34.4	$R\phi = 16, z = 580$	3.2	± 1.4
9 end-cap wheels on each side	26.7	$R\phi = 16, z = 580$	3.0	1.4–2.5
TRT:				
Axial barrel straws		170 (per straw)	0.1	± 0.7
Radial end-caps straws		170 (per straw)	0.32	0.7–2.5

Table 2.4: Parameters of the inner detector. The resolutions quoted are typical values; the actual resolution in each detector depends on the impact angle. (Taken from [86])

2.5 Calorimeter system

In the ATLAS detector there are two calorimeters for energy measurements. One of these sub-detectors is dedicated to identify electrons and photons, the electromagnetic calorimeter, and the other one is dedicated to the identification of hadrons, the hadronic calorimeter. A cut-away view of the ATLAS calorimeters is shown in Figure 2.8 and the main parameters of the ATLAS calorimeters are summarised in Tables 2.5 and 2.6.

The ATLAS electromagnetic calorimeter is made of accordion-shaped lead layers with thickness ranging between 1.1 mm and 2.2 mm. Between the lead layers, liquid argon (LAr) is used as the active material. It is divided into three sub-calorimeters: one in the barrel, which covers the pseudorapidity $|\eta| < 1.475$, and two in the end-caps, which cover the pseudorapidity $1.375 < |\eta| < 3.2$. The end-caps calorimeters are also divided into two parts at $|\eta| = 2.5$. The goal resolution for the electromagnetic calorimeter is $\sigma_E/E = 10\%/\sqrt{E} \oplus 0.7\%$.

The hadronic calorimeter of ATLAS is in reality made of three different sub-detectors. They are the tile calorimeter (TileCal), the LAr hadronic end-cap calorimeter (HEC) and the LAr forward calorimeter (FCal). The first one has steel as the absorbing material and scintillating tiles as the active material. It is divided into two regions, the barrel ($|\eta| < 1.0$) and the extended barrel ($0.8 < |\eta| < 1.7$). Each zone has an inner radius of 2.28 m, an outer radius of 4.25 m and 64 modules. The TileCal has 9.7 interaction lengths (λ) at $\eta = 0$. Wavelength shifting optical fibres, connected to photomultiplier tubes, are used to read the scintillating tiles. The HEC extends from $|\eta| = 1.5$ to $|\eta| = 3.2$. Copper plates are used as absorbing material, while LAr is used again as active material. The inner radius of the HEC is 0.475 m and the outer one is 2.03 m. The FCal are located in each end-cap of ATLAS and are divided into three modules. The first one has copper as passive material, while the other two have tungsten. The active

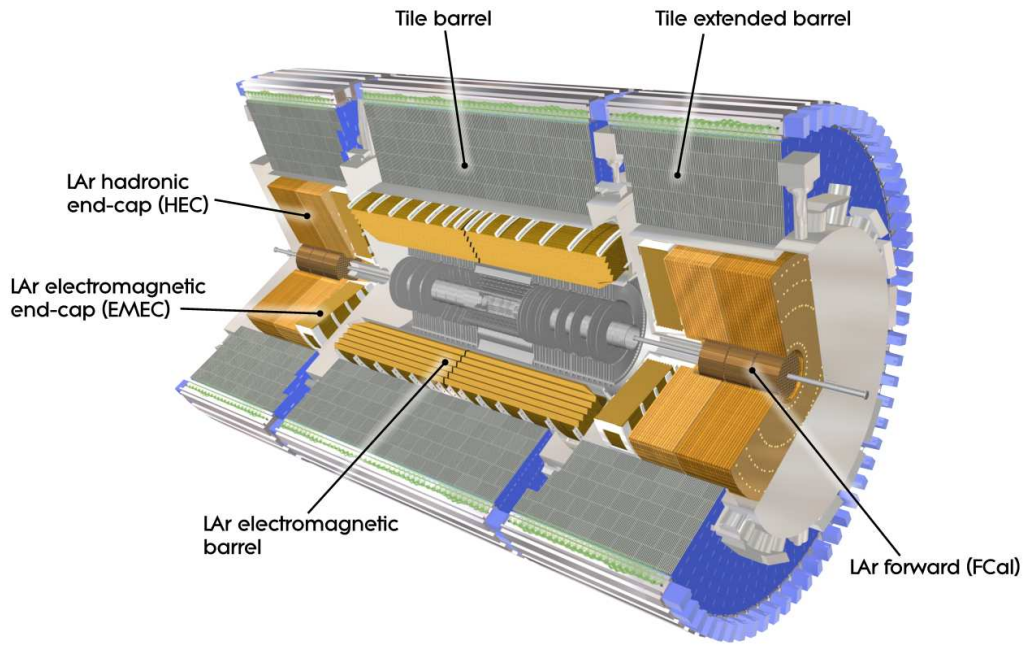

Figure 2.8: Cut-away view of the ATLAS calorimeter system. (Taken from [87])

material is, once more, LAr. The total radiation length of this calorimeter is about 10 λ. The goal resolution for the hadronic calorimeter is $\sigma_E/E = 50\%/\sqrt{E} \oplus 3\%$ in the barrel and end-caps and is $\sigma_E/E = 100\%/\sqrt{E} \oplus 10\%$ in the forward regions.

2.6 Muon system

The last set of ATLAS sub-detectors is the muon spectrometer. Due to the total large value of λ of the previous systems, muons are the only charged particles expected to reach this detector. The muons are bended by the magnetic field of the barrel toroid in the $|\eta| < 1.4$ region and by the end-cap toroids in the $1.6 < |\eta| < 2.7$ regions (the magnetic field in the region defined by $1.4 < |\eta| < 1.6$ is a combination of the ones produced by both toroids). There are three layers of sub-detectors either in the barrel and in the end-caps. The monitored drift tubes (MDT) and the cathode strip chambers (CSC) were designed for muon tracking up to $|\eta| < 2.7$, while the resistive plate chambers (RPC) and the thin gap chambers (TGC) will be used primarily with the trigger system ($|\eta| < 2.4$). The system is shown in Figure 2.9, while Table 2.7 gives a summary of its main parameters. The goal resolution of the muon spectrometer is $\sigma_{p_T}/p_T = 10\%$ at $p_T = 1$ TeV.

2.7 Trigger and data acquisition systems

The ATLAS Trigger and data acquisition systems were designed to reduce the event rate from about 1 GHz to ~200 Hz. They are based on signatures of high p_T particles and missing transverse energy, and are divided into three parts as represented in Figure 2.10: the first level trigger (LVL1), the High Level Trigger (HLT) and the Data Flow system, which buffers

	Barrel		End-cap	
Number of layers and $\|\eta\|$ coverage:				
Presampler	1	$\|\eta\| < 1.52$	1	$1.5 < \|\eta\| < 1.8$
Calorimeter	3	$\|\eta\| < 1.35$	2	$1.375 < \|\eta\| < 1.5$
	2	$1.35 < \|\eta\| < 1.475$	3	$1.5 < \|\eta\| < 2.5$
			2	$2.5 < \|\eta\| < 3.2$
Granularity $\Delta\eta \times \Delta\phi$ versus $\|\eta\|$:				
Presampler	0.025×0.1	$\|\eta\| < 1.52$	0.025×0.1	$1.5 < \|\eta\| < 1.8$
Calorimeter 1st layer	$0.025/8 \times 0.1$	$\|\eta\| < 1.4$	0.050×0.1	$1.375 < \|\eta\| < 1.425$
	0.025×0.025	$1.4 < \|\eta\| < 1.475$	0.025×0.1	$1.425 < \|\eta\| < 1.5$
			$0.025/8 \times 0.1$	$1.5 < \|\eta\| < 1.8$
			$0.025/6 \times 0.1$	$1.8 < \|\eta\| < 2.0$
			$0.025/4 \times 0.1$	$2.0 < \|\eta\| < 2.4$
			0.025×0.1	$2.4 < \|\eta\| < 2.5$
			0.1×0.1	$2.5 < \|\eta\| < 3.2$
Calorimeter 2nd layer	0.025×0.025	$\|\eta\| < 1.4$	0.050×0.025	$1.375 < \|\eta\| < 1.425$
	0.075×0.025	$1.4 < \|\eta\| < 1.475$	0.025×0.025	$1.425 < \|\eta\| < 2.5$
			0.1×0.1	$2.5 < \|\eta\| < 3.2$
Calorimeter 3rd layer	0.050×0.025	$\|\eta\| < 1.35$	0.050×0.025	$1.5 < \|\eta\| < 2.5$
Number of readout channels				
Presampler	7808		1536 (both sides)	
Calorimeter	101760		62208 (both sides)	

Table 2.5: Parameters of the ATLAS electromagnetic calorimeter system. (Adapted from [87])

	Barrel	End-cap	
Scintillator tile calorimeter (TileCal):			
$\|\eta\|$ coverage	$\|\eta\| < 1.0$	$0.8 < \|\eta\| < 1.7$	
Number of layers	3	3	
Granularity $\Delta\eta \times \Delta\phi$	0.1×0.1	0.1×0.1	
	0.2×0.1	2.2×0.1	
Readout channels	5760	4092 (both sides)	
LAr hadronic endcap (HEC):			
$\|\eta\|$ coverage		$1.5 < \|\eta\| < 3.2$	
Number of layers		4	
Granularity $\Delta\eta \times \Delta\phi$		0.1×0.1	$1.5 < \|\eta\| < 2.5$
		0.2×0.2	$2.5 < \|\eta\| < 3.2$
Readout channels		5632 (both sides)	
LAr forward calorimeter (FCal):			
$\|\eta\|$ coverage		$3.1 < \|\eta\| < 4.9$	
Number of layers		3	
Granularity $\Delta x \times \Delta y$ (cm)		FCal 1	3.0×2.6
		FCal 2	2.3×4.2
		FCal 3	5.4×4.7
Readout channels		3524 (both sides)	

Table 2.6: Parameters of the ATLAS hadronic calorimeter system. (Adapted from [87])

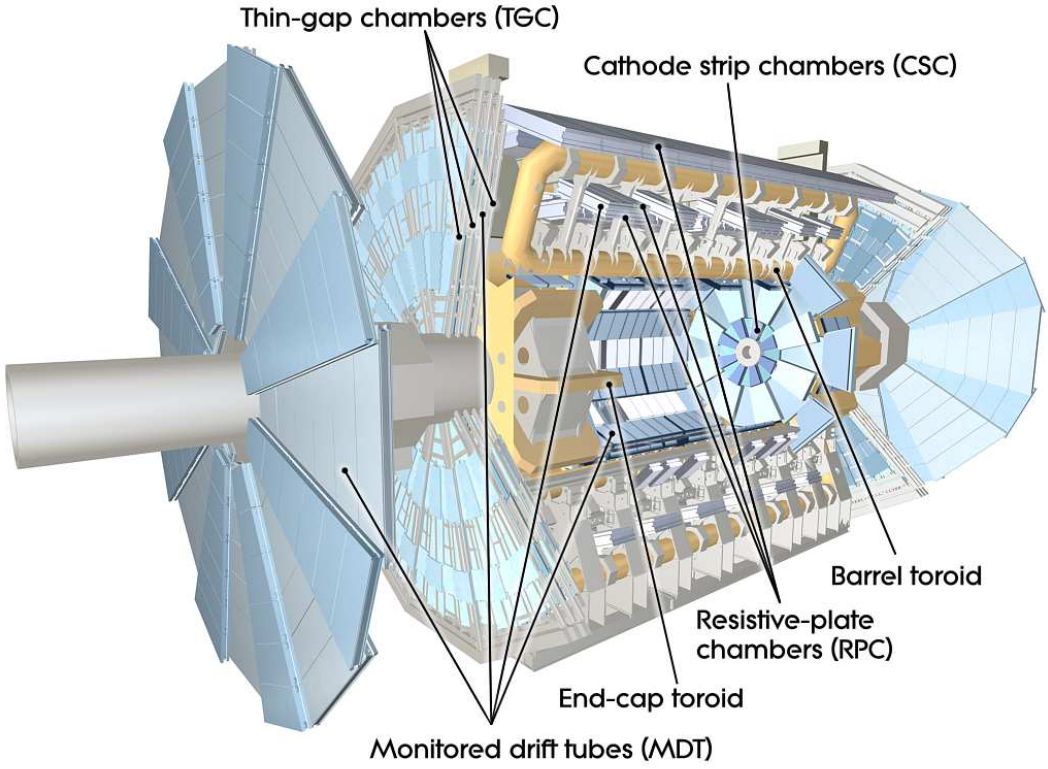

Figure 2.9: Cut-away view of the ATLAS muon system. (Taken from [87])

Monitored drift tubes (MDT):	
Coverage	$\lvert\eta\rvert < 2.7$ (innermost layer: $\lvert\eta\rvert < 2.0$)
Number of chambers	1088 (1150)
Number of channels	339000 (354000)
Function	precision tracking
Cathode strip chambers (CSC):	
Coverage	$2.0 < \lvert\eta\rvert < 2.7$
Number of chambers	32
Number of channels	31000
Function	precision tracking
Resistive plate chambers (RPC):	
Coverage	$\lvert\eta\rvert < 1.05$
Number of chambers	544 (606)
Number of channels	359000 (373000)
Function	triggering, second coordinate
Thin gap chambers (TGC):	
Coverage	$1.05 < \lvert\eta\rvert < 2.7$ (for triggering: $\lvert\eta\rvert < 2.4$)
Number of chambers	3588
Number of channels	318000
Function	triggering, second coordinate

Table 2.7: Main parameters of the ATLAS muon spectrometer. Numbers in brackets for the MDT and the RPC refer to the final configuration of the detector in 2009. (Adapted from [87])

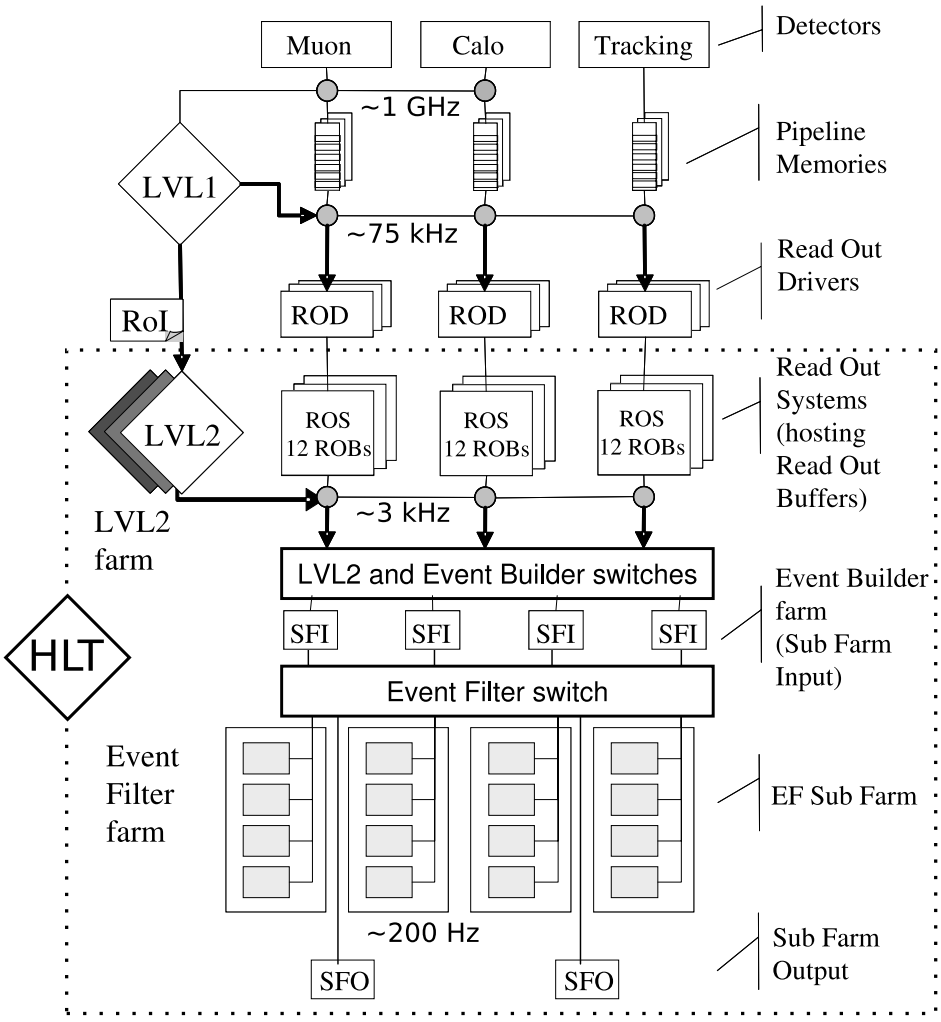

Figure 2.10: The ATLAS trigger and data acquisition systems. (Adapted from [88])

data and passes it to the HLT and storing systems.

The LVL1 takes decisions within 2.5 μs by looking into the calorimeter system coarse data and the fast muon chambers (RPC and TGC). Meanwhile, the front-end electronics of the several sub-detectors keep the complete data in the pipeline memories. The data is then moved to the Readout Buffers (ROB) via the Readout Drivers (ROD). The event rate after LVL1 is about 75 kHz.

The HLT is divided into two trigger levels, the second level trigger (LVL2) and the Event Filter (EF). The LVL2 receives a list with Regions of Interest (RoI), which contains the positions of the objects selected by LVL1. In this way, the LVL2 only needs to access about 2% of the full event data in order to take its decision. After this level, which has a a latency of $\mathcal{O}(10)$ ms, the event rate is about 3 kHz. The event information is then passed to the Sub-Farm Input (SFI), which provides the full data to the EF. This filter has a latency of $\mathcal{O}(1)$ s and achieves a event rate of about 200 Hz. The selected events are then moved into the Sub-Farm Output (SFO) and stored to be analysed later.

The trigger requirements are labeled with letter codes (which correspond to the type of

triggered objects) and numbers (which correspond to the p_T cut for which the trigger is 95% efficient and to the multiplicity of objects). The letter "i" is used to indicate that the object must be isolated. For example, the "2e15i" menu means that the efficiency for triggering an event with two isolated electrons with p_T higher than 15 GeV is 95%.

3

Analyses with high luminosity

This chapter describes the analyses done to study the ATLAS sensitivity to the FCNC top quark decays in $t\bar{t}$ events with an integrated luminosity of $L = 10$ fb^{-1} (the results are also extrapolated to $L = 100$ fb^{-1}). Similarly with what happened at the Tevatron, the background cross-sections will be measured with high precision. It is also expected that the MC generation and the detector simulation will describe with high accuracy the underlying physics and detector performance. The ATLAS fast simulation, which allows to handle large Monte-Carlo (MC) samples, was therefore used to estimate the experiment sensitivity for this luminosity and the associated systematic uncertainties. The following topics will be covered: the signal and background generation, the ATLAS fast simulation, the event selection, the results of the analyses and a discussion about the systematic uncertainties and the analyses stability. The work presented in this chapter was published and described in [89, 90, 91].

3.1 Signal and background generation

The MC generation of signal samples, corresponding to $t\bar{t}$ events, where one of the top quarks decays via charged currents into bW and the other one decays through FCNC into $q\gamma$, qZ or qg, was done with the TopReX 4.05 program [92]. The anomalous couplings to the γ, Z and g bosons were set to

$$\kappa_{tq}^{\gamma} = \sqrt{|v_{tq}^{Z}|^2 + |a_{tq}^{Z}|^2} = \kappa_{tq}^{Z} = \kappa_{tq}^{g} = 0.1, \tag{3.1}$$

Λ was set to 1 TeV and the top quark mass to 175 GeV. For the $t \to qg$ channel, TopReX returns a total top quark width of $\Gamma_t = 1.581$ GeV, which is very similar to the one predicted considering only the SM decays ($\Gamma_t = 1.553$ GeV). Other values were also tested. Smaller values of κ_{tq}^{g} give total widths more similar to the SM prediction. Changing Λ to 2 TeV (500 GeV) results in $\Gamma_t = 1.560$ GeV ($\Gamma_t = 1.667$ GeV). No significant differences were observed in relevant kinematic distributions given by the generator.

The Monte-Carlo (MC) generation of the QCD ($b\bar{b}$), W+jets, Z/γ^*+jets, WW, ZZ and ZW background processes was done with the PYTHIA 6.206 [93] library. The SM top quark pair production and single top quark production were generated with TopReX. No SUSY backgrounds or other contributions beyond the SM were considered in the present analyses.

All events were hadronized using PYTHIA. Initial and final state radiation (ISR and FSR, respectively) were also handled by PYTHIA. The minimum p_T of the $2 \to 2$ hard process (defined in the rest frame of the hard interaction) was set to 5 GeV. The CTEQ 5L PDF [94] were

process	generator	σ (pb)	no. events	L (fb^{-1})
regular samples:				
$t\bar{t} \rightarrow bWq\gamma$	TopReX	5.28×10^{-1}	1.00×10^{6}	1.90×10^{3}
$t\bar{t} \rightarrow bWqZ$	TopReX	8.87×10^{-1}	1.00×10^{6}	1.13×10^{3}
$t\bar{t} \rightarrow bWqg$	TopReX	8.91×10^{0}	1.00×10^{6}	1.12×10^{2}
$t\bar{t} \rightarrow bWbW$	TopReX	8.33×10^{2}	6.00×10^{6}	7.20×10^{0}
single top (t-channel)	TopReX	2.68×10^{2}	2.00×10^{6}	7.47×10^{0}
single top (Wt channel)	TopReX	5.13×10^{1}	1.50×10^{6}	2.93×10^{1}
single top (s channel)	TopReX	6.86×10^{0}	1.50×10^{6}	2.19×10^{2}
$Z/\gamma^{*}+j$	PYTHIA	6.09×10^{4}	8.50×10^{7}	1.40×10^{0}
$W+j$	PYTHIA	1.48×10^{5}	3.50×10^{7}	2.37×10^{-1}
WZp	PYTHIA	7.46×10^{2}	4.75×10^{7}	6.38×10^{1}
$b\bar{b}$	PYTHIA	1.57×10^{8}	3.75×10^{8}	2.39×10^{-3}

Table 3.1: The MC generator, cross-section and luminosity is shown for each generated regular sample used in the analyses. All the hadronic and leptonic decays of the W and Z bosons were considered, with the exception of the $t\bar{t} \rightarrow bWqZ$ channel, where only the decay of the Z boson to charged leptons was allowed. The NLO cross-section values were used for the $t\bar{t} \rightarrow bWbW$ sample. No K factors were used for the other samples.

used. No pile-up was taken into account. The generated samples are listed in Table 3.1. K factors, which are the ratio between the NLO and the leading order (LO) cross-sections, where used for the $t\bar{t} \rightarrow bWbW$ sample. No K factors were used for the other samples. The cross-sections given for the signal channels are the LO ones as computed by TopReX. The generated particles will be labeled "true particles".

Different values for the top quark mass, 170 GeV and 180 GeV, were also generated for the study of systematic uncertainties, as explained in section 3.4. A different PDF set, CTEQ 4M [95], was used for systematic uncertainties studies. The generated samples are listed in Table 3.2.

3.2 Fast simulation

The generated background and signal events were passed through the ATLAS fast simulation packages ATLFAST [96] and ATLFAST-B [96]. The fast simulation is based on the smearing of the energies and momenta of the stable final state particles generated and no specific detector effects are simulated. Thus, the fast simulation of MC events is rapid. For the generated samples, it typically spent between 0.02 s to 0.06 s per MC event, depending on the process. Therefore, with ATLFAST it is possible to simulate large samples, with several millions of events, in order to control the statistical error and study the systematic uncertainties. No identification efficiencies or mistag rates are considered in the fast simulation, although a charged lepton efficiency of 90% will be considered in later steps of the analyses. Similarly, the trigger was not simulated, but it is supposed that events with at least one isolated charged lepton (with p_T >25 GeV) will be selected by the trigger.

process	generator	σ (pb)	no. events	L (fb^{-1})
$m_t = 170$ GeV:				
$t\bar{t} \rightarrow\ bWq\gamma$	TopReX	6.13×10^{-1}	1.00×10^{6}	1.63×10^{3}
$t\bar{t} \rightarrow\ bWqZ$	TopReX	1.01×10^{0}	1.00×10^{6}	9.94×10^{2}
$t\bar{t} \rightarrow\ bWqg$	TopReX	1.03×10^{1}	1.00×10^{6}	9.68×10^{1}
$t\bar{t} \rightarrow\ bWbW$	TopReX	9.40×10^{2}	5.50×10^{6}	5.85×10^{0}
single top (t-channel)	TopReX	2.80×10^{2}	2.00×10^{6}	7.15×10^{0}
single top (Wt channel)	TopReX	5.53×10^{1}	1.50×10^{6}	2.71×10^{1}
single top (s channel)	TopReX	7.62×10^{0}	1.50×10^{6}	1.97×10^{2}
$m_t = 180$ GeV:				
$t\bar{t} \rightarrow\ bWq\gamma$	TopReX	4.56×10^{-1}	1.00×10^{6}	2.19×10^{3}
$t\bar{t} \rightarrow\ bWqZ$	TopReX	7.84×10^{-1}	1.00×10^{6}	1.28×10^{3}
$t\bar{t} \rightarrow\ bWqg$	TopReX	7.71×10^{0}	1.00×10^{6}	1.30×10^{2}
$t\bar{t} \rightarrow\ bWbW$	TopReX	7.20×10^{2}	6.00×10^{6}	8.33×10^{0}
single top (t-channel)	TopReX	2.56×10^{2}	2.00×10^{6}	7.80×10^{0}
single top (Wt channel)	TopReX	4.76×10^{1}	1.50×10^{6}	3.15×10^{1}
single top (s channel)	TopReX	6.20×10^{0}	1.50×10^{6}	2.42×10^{2}
CTEQ 4m:				
$t\bar{t} \rightarrow\ bWq\gamma$	TopReX	7.26×10^{-1}	1.00×10^{5}	1.39×10^{2}
$t\bar{t} \rightarrow\ bWqZ$	TopReX	1.22×10^{0}	1.00×10^{5}	8.22×10^{1}
$t\bar{t} \rightarrow\ bWqg$	TopReX	1.22×10^{1}	1.00×10^{5}	8.17×10^{0}
$t\bar{t} \rightarrow\ bWbW$	TopReX	8.33×10^{2}	3.50×10^{6}	4.20×10^{0}
single top (t-channel)	TopReX	3.11×10^{2}	1.00×10^{6}	1.60×10^{0}
single top (Wt channel)	TopReX	6.70×10^{1}	5.00×10^{5}	7.46×10^{0}
single top (s channel)	TopReX	7.67×10^{0}	5.00×10^{5}	6.52×10^{1}
$Z/\gamma^{*} + j$	PYTHIA	6.23×10^{4}	5.00×10^{7}	8.03×10^{-1}
$W + j$	PYTHIA	1.55×10^{5}	2.25×10^{7}	1.45×10^{-1}
WZp	PYTHIA	8.03×10^{2}	1.50×10^{7}	1.87×10^{1}
$b\bar{b}$	PYTHIA	1.11×10^{8}	1.50×10^{8}	1.35×10^{-3}

Table 3.2: The MC generator, cross-section and luminosity is shown for each generated sample used to study systematic uncertainties. All the hadronic and leptonic decays of the W and Z bosons were considered, with the exception of the $t\bar{t} \rightarrow\ bWqZ$ channel, where only the decay of the Z boson to charged leptons was allowed. The NLO cross-section values were used for the $t\bar{t} \rightarrow bWbW$ sample. No K factors were used for the other samples.

Energy clusters

For each event, the ATLFAST package begins by simulating the energy deposition by all the stable particles in the calorimeter cells. The $\Delta\eta \times \Delta\phi$ dimensions of the cells are:

$$\Delta\eta \times \Delta\phi = \begin{cases} 0.1 \times 0.1, & |\eta| < 3 \\ 0.2 \times 0.2, & 3 < |\eta| < 5 \end{cases} \tag{3.2}$$

The calorimeter cells are clustered within a cone of $\Delta R = 0.4$. Cells with $E_T > 1.5$ GeV are used as cluster seeds and the cone algorithm is applied in decreasing order of E_T. Only clusters with $E_T > 5$ GeV are considered.

Muons

The momentum of each muon is smeared according to a resolution which depends on the p_T, $|\eta|$ and ϕ:

$$p^{\mu}_{\text{smeared}} = \frac{p^{\mu}_{\text{true}}}{(1+\sigma)}. \tag{3.3}$$

The transverse momentum resolution of muons with $p_T < 100$ GeV is $\sigma p_T / p_T \lesssim 2\%$.

Electrons and photons

The polar angle and the energy of photons are smeared according to Gaussian parameterizations:

$$\frac{\sigma(E_\gamma)}{E_\gamma} = \frac{0.10}{\sqrt{E_\gamma}} \oplus \frac{0.245}{E^T_\gamma} \oplus 0.007, \tag{3.4}$$

$$\sigma(\theta_\gamma) = \begin{cases} \frac{0.065}{\sqrt{E_\gamma}}, & |\eta| < 0.8 \\ \frac{0.050}{\sqrt{E_\gamma}}, & 0.8 < |\eta| < 1.4 \\ \frac{0.40}{\sqrt{E_\gamma}}, & 1.4 < |\eta| < 2.5 \end{cases} \tag{3.5}$$

For electrons, their energies are smeared according to a Gaussian parameterization:

$$\frac{\sigma(E_e)}{E_e} = \frac{0.12}{\sqrt{E_e}} \oplus \frac{0.245}{E^T_e} \oplus 0.007 \tag{3.6}$$

The photon (electron) energy resolution is $\sigma(E)/E < 2.9\%$ (3.3%), for $E > 20$ GeV. Photons, electrons and muons are selected only if they have $|\eta| < 2.5$ and $p_T > 5$ GeV ($p_T > 6$ GeV for muons). They are classified as isolated if the transverse energy of the cluster associated to the particle, inside a cone of $\Delta R = 0.2$, does not exceed in 10 GeV the particle energy, and the ΔR from other energy clusters is above 0.4.

Jets

The clusters of energy depositions not associated to isolated photons, electrons or muons are used for the jet reconstruction. Their energies are smeared according to a Gaussian distribution which depends on $|\eta|$:

$$\frac{\sigma(E_j)}{E_j} = \begin{cases} \frac{0.50}{\sqrt{E_j}} \oplus 0.03, & (|\eta| < 3; \quad \Delta\eta \times \Delta\phi = 0.1 \times 0.1 \text{ cells}) \\ \frac{1.0}{\sqrt{E_j}} \oplus 0.07, & (|\eta| > 3; \quad \Delta\eta \times \Delta\phi = 0.2 \times 0.2 \text{ cells}) \end{cases} \tag{3.7}$$

	C^{c_f}	(c_f)	C^{c_f}	(c_f)	C^{c_f}	(c_f)
c-jets:						
nominal efficiency	9.2%		14.9%		23.3%	
$p_T < 30$ GeV	0.72	(12.7%)	0.76	(19.6%)	0.79	(29.4%)
30 GeV $< p_T <$ 45 GeV	0.91	(10.1%)	0.90	(16.5%)	0.93	(25.0%)
45 GeV $< p_T <$ 60 GeV	1.28	(7.2%)	1.25	(11.9%)	1.30	(17.9%)
60 GeV $< p_T <$ 100 GeV	1.28	(7.2%)	1.18	(12.6%)	1.21	(19.2%)
$p_T > 100$ GeV	1.21	(7.6%)	1.15	(12.9%)	1.02	(22.8%)
u, d, s, g and τ-jets:						
nominal efficiency	0.4%		1.1%		2.9%	
$p_T < 30$ GeV	0.53	(0.8%)	0.48	(2.0%)	0.56	(5.2%)
30 GeV $< p_T <$ 45 GeV	1.04	(0.4%)	1.23	(0.8%)	1.09	(2.7%)
45 GeV $< p_T <$ 60 GeV	3.10	(0.1%)	2.30	(0.4%)	2.08	(1.4%)
60 GeV $< p_T <$ 100 GeV	2.27	(0.2%)	1.70	(0.5%)	1.67	(1.8%)
$p_T > 100$ GeV	0.72	(0.6%)	1.08	(0.9%)	1.17	(2.5%)

Table 3.3: The transverse momenta dependent correction factors (C^{c_f}) to be applied to the nominal contamination factors. The corresponding effective contamination factors (c_f) for the c-jets and the light quark, gluon and tau jets are also shown.

Jets are selected if they have $E_T > 10$ GeV. For $E > 20$ GeV, the jet energy resolution is better than 12% ($|\eta| < 3$) and less than 24% ($|\eta| > 3$).

Missing energy

The missing transverse momentum is estimated by summing the transverse momentum of the isolated photons, electrons, muons and jets. The non isolated muons and the clusters of energy deposition not associated to isolated photons, electrons, muons or jets, are also taken into account.

Jet tagging

In the ATLAS experience, it will be possible to identify b-jets with $|\eta| < 2.5$ using b-tagging tools. The jet tagging is handled by the ATLFAST-B package. The algorithm was simulated by setting the b-tagging efficiency to 60%, with contamination factors set to 14.9% (1.1%) for c-jets (light quark, gluon and tau jets). The transverse momenta dependent correction factors of Table 3.3 were applied to the nominal contamination factors. In order to check the dependence of the analysis with the b-tagging efficiencies, different values, 50% and 70% (corresponding to the expected b-tag variation within the interesting signal transverse momentum range), were also considered for the systematic studies, with contamination factors of 9.2% (0.4%) and 23.3% (2.9%) for c-jets (light quark, gluon and tau jets), respectively.

	b-tagged jets		light jets	
	$p_T < 55$ GeV	$p_T > 55$ GeV	$p_T < 45$ GeV	$p_T > 45$ GeV
a_0	$+1.2791$	$+1.18$	$+1.5085$	$+1.1512$
a_1	$+1.2314 \times 10^{-1}$	-1.6672×10^{-3}	$+3.1468 \times 10^{-2}$	-1.6265×10^{-3}
a_2	-1.0543×10^{-2}	$+4.4414 \times 10^{-6}$	-3.6973×10^{-3}	$+4.3331 \times 10^{-6}$
a_3	$+3.3510 \times 10^{-4}$	—	$+1.1220 \times 10^{-4}$	—
a_4	-4.7739×10^{-6}	—	-1.3921×10^{-6}	—
a_5	$+2.5589 \times 10^{-8}$	—	$+6.1538 \times 10^{-9}$	—

Table 3.4: Coefficients for the 2^{nd} and 5^{th} order polynomials used to calibrate the b-tagged and light jet energies, within the fast simulation.

Jet energy calibration

As a result of the quark hadronisation, the reconstructed energy of the jets can be smaller than the true quark, gluon or hadronic tau energy. After the jet tagging, the total energy of each jet is recalibrated in the fast simulation by using 2^{nd} and 5^{th} order polynomials, whose coefficients are shown in Table 3.4 and are different for b-tagged and light jets.

3.3 Event selection

The $t\bar{t}$ final states corresponding to the different FCNC top quark decay modes lead to different topologies according to the number of jets, leptons and photons. There is however a common characteristic of all channels under study, *i.e.* in all of them one of the top quarks is assumed to decay through the dominant SM decay mode $t \to bW$ and the other is forced to decay via one of the FCNC modes $t \to q\gamma$, $t \to qZ$ or $t \to qg$. The three considered channels, $t\bar{t} \to bWq\gamma$, $t\bar{t} \to bWqZ$ and $t\bar{t} \to bWqg$, will be labeled $t \to q\gamma$, $t \to qZ$ and $t \to qg$, respectively. The leptonic decays of the W ($W \to \ell\nu_\ell, \ell = e, \mu, \tau$) were considered as signal. Figure 1.6 shows schematic representations of the signal event topologies. The analyses of the different channels were divided into two levels, a preselection and a final selection, which are summarised in Table 3.5 and are explained in more detail in the next subsections.

Preselection

$t \to q\gamma$ channel:

The $t\bar{t}$ final states corresponding to the FCNC decay $t \to q\gamma$ are characterised by the presence of a high p_T photon and a light jet from the top quark decay. Since the existence of the photon is not sufficient to reduce the QCD background, only the leptonic decays of the W (originated from the SM decay of the other top quark) were considered. The final states corresponding to these signal events are characterised by a topology with two jets (one b-jet from the SM top quark decay), one high p_T photon, one lepton and missing transverse momentum from the undetected neutrino. The preselection for the $t \to q\gamma$ channel was defined by requiring the events to have at least one photon with $p_T > 50$ GeV and $|\eta| < 2.5$, one isolated lepton with $p_T > 25$ GeV and $|\eta| < 2.5$ and two jets, both with $p_T > 20$ GeV and $|\eta| < 2.5$. A missing transverse momentum greater than 20 GeV was also required. Additionally, in order

to prevent events to be simultaneously assigned to the $t \to qZ$ (which is a three lepton plus jets topology channel) and $t \to q\gamma$ channels, a maximum of two leptons were allowed in the final state.

$t \to qZ$ channel:

The QCD backgrounds at hadron colliders make the search for the signal via the fully hadronic channel (when both the W and Z decay hadronically) very difficult. For this reason only the leptonic decays of the W and Z bosons were considered. The channel in which the W boson decays hadronically ($t\bar{t} \to bqqq\ell\ell$), was studied already in ATLAS, but its sensitivity is about four times smaller [97, 98]. As a starting point, only the $t\bar{t} \to b\ell\nu q\ell\ell$ channel was considered here. The experimental signature of the channel includes three isolated charged leptons, two of which reconstruct a Z boson, large missing transverse energy due to the neutrino, and at least two jets, one of which is tagged as a b-jet. For this channel, the events were required to have at least three isolated leptons (with $p_T > 25$ GeV for the leading lepton and $p_T > 10$ GeV for the other two leptons with highest transverse momenta), and at least two jets with $p_T > 20$ GeV in the final state. All three leptons and the two jets were required to have $|\eta| < 2.5$. Additionally, the transverse missing momentum had to be higher than 20 GeV.

$t \to qg$ channel:

The final states of $t\bar{t}$ events with one of the top quarks decaying into a gluon plus a light quark, $t \to qg$, are characterised by the presence of a high p_T gluon jet and a light jet from the top quark decay. Only the leptonic decays of the W (originated from the SM decay of the other top quark) were taken into account, otherwise the final state would be fully hadronic and the signal would be overwhelmed by the QCD background. The final states are thus characterised by the existence of at least three jets (one b-jet from the SM top quark decay), one lepton and missing transverse momentum from the undetected neutrino. As in this topology the FCNC top quark decay corresponds to a fully hadronic final state, a more restrictive event selection was necessary. At the preselection, the events were required to have only one isolated lepton (with $p_T > 25$ GeV and $|\eta| < 2.5$) and no photons with transverse momentum above $p_T > 5$ GeV, to reject events assigned to the other FCNC channels. The total visible energy (E_{vis}) had to be greater than 300 GeV. At least three jets with $|\eta| < 2.5$ and $p_T > 20$ GeV were required. If the event had at least four jets, the fourth jet should also have $p_T > 20$ GeV and $|\eta| < 2.5$. For the leading jet the cut was increased to 40 GeV. The preselection was completed by requiring only one b-tagged jet in the event. Finally, it was required that the event should have a missing transverse momentum greater than 20 GeV. The events were then classified as "3 jets" or "4 jets" if they had exactly three jets or at least 4 jets, respectively.

Number of selected events and relevant variables:

The selection criteria for these channels are orthogonal. All the background samples were normalised to $L = 10$ fb^{-1}. The number of selected background events and the signal efficiency are shown in Table 3.6. The distribution of relevant variables at this selection level are shown from Figure 3.1 to Figure 3.4

channel	$t\bar{t} \to bWq\gamma$	$t\bar{t} \to bWqZ$	$t\bar{t} \to bWqg$	
			"3 jets"	"4 jets"
preselection	$= 1\ell$ or $= 2\ell$ ($p_T > 25,5$ GeV)	$\geq 3\ell$ ($p_T > 25,10,10$ GeV)	$= 1\ell$ ($p_T > 25$ GeV)	$= 1\ell$ ($p_T > 25$ GeV)
	$\geq 2j$ ($p_T > 20$ GeV)	$\geq 2j$ ($p_T > 20,20$ GeV)	$= 3j$ ($p_T > 40,20,20$ GeV)	$\geq 4j$ ($p_T > 40,20,20,20$ GeV)
	$\geq 1\gamma$ ($p_T > 50$ GeV)	$\not{p}_T > 20$ GeV	$= 1b$	$= 1b$
	$\not{p}_T > 20$ GeV		$= 0\gamma$ ($p_T > 5$ GeV)	$= 0\gamma$ ($p_T > 5$ GeV)
			$\not{p}_T > 20$ GeV	$\not{p}_T > 20$ GeV
			$E_{\text{vis}} > 300$ GeV	$E_{\text{vis}} > 300$ GeV
			has $p_{z\nu}$ solution	has $p_{z\nu}$ solution
final	$p_{T\gamma} > 75$ GeV	$= 1b$ or $= 2b$	$p_{Tg} > 75$ GeV	$p_{Tg} > 100$ GeV
selection	$= 1b$	has $p_{z\nu}$ solution	$m_{qg} > 125$ GeV	$m_{qg} > 150$ GeV
	has $p_{z\nu}$ solution	$p_{Tj_1} > 30$ GeV	$m_{qg} < 200$ GeV	$m_{qg} < 190$ GeV
		2 ℓ same flavour,		
		oppos. charge		

Table 3.5: Selection cuts applied in the analyses with fast simulation. Additionaly, the leptons, photons and jets had to have $|\eta| < 2.5$. For the $t \to qg$ channels, E_{vis}, p_{Tg} and m_{qg} represent the total visible energy, the transverse momentum of the leading non-b-jet and the reconstructed mass of the two non-b-jets with higher transverse momenta, respectively (see text for details).

	Z+jets	W+jets	WZ pairs	$t\bar{t}$	single top	total background	signal efficiency %
after preselection:							
$t \to q\gamma$	584 ± 67	0 ± 42	326 ± 7	2832 ± 69	206 ± 14	3986 ± 106	$23.26\% \pm 0.08\%$
$t \to qZ$	79 ± 23	0 ± 42	30 ± 2	1514 ± 16	24 ± 3	1647 ± 51	$16.98\% \pm 0.07\%$
$t \to qg$ channel ("3 jets")	1357 ± 98	23320 ± 992	427 ± 8	24367 ± 184	11328 ± 100	60799 ± 1018	$1.60\% \pm 0.02\%$
$t \to qg$ channel ("4 jets")	1171 ± 91	12651 ± 730	305 ± 7	216680 ± 548	14263 ± 107	245070 ± 924	$5.65\% \pm 0.04\%$
after final selection:							
$t \to q\gamma$	15 ± 11	0 ± 42	8 ± 1	272 ± 21	23 ± 5	318 ± 49	$6.85\% \pm 0.05\%$
$t \to qZ$	13 ± 9	0 ± 42	2 ± 1	434 ± 9	5 ± 2	454 ± 44	$7.07\% \pm 0.05\%$
$t \to qg$ channel ("3 jets")	157 ± 34	1813 ± 277	22 ± 2	4986 ± 83	1188 ± 36	8166 ± 293	$1.20\% \pm 0.02\%$
$t \to qg$ channel ("4 jets")	64 ± 21	380 ± 127	7 ± 1	9142 ± 113	453 ± 22	10047 ± 172	$1.15\% \pm 0.02\%$

Table 3.6: The number of selected background events, normalised to $L = 10$ fb^{-1}, and signal efficiencies in the $t \to q\gamma$, $t \to qZ$, $t \to qg$ channel ("3 jets") and $t \to qg$ channel ("4 jets") channels for the preselection and final selection levels are shown. No $b\bar{b}$ event within the generated statistics, passed the selection criteria. The statistical error from this background was not considered for the total error. The signal efficiencies were computed taking into account only the decays with charged leptons (e, μ and τ) of the W and Z bosons.

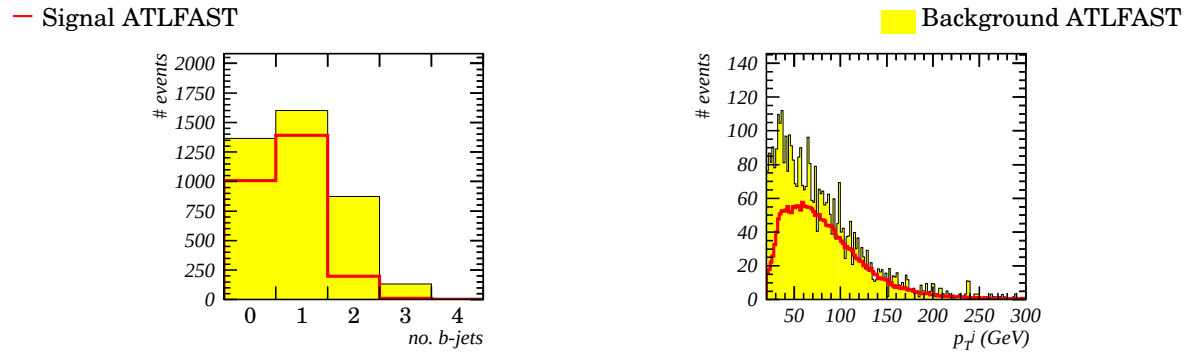

Figure 3.1: The distributions of relevant variables for the $t \to q\gamma$ channel are shown after the preselection level: a) number of b-jets and b) transverse momentum of the leading non-b-jet (p_T^j). The SM background is normalised to $L = 10$ fb^{-1} and the signal has an arbitrary normalization, but the same in all plots of this figure.

Final selection

In order to reduce the background contribution, further selection cuts were applied to the four channels under study.

$t \to q\gamma$ channel:

The final event selection for the $t \to q\gamma$ channel was done by requiring the leading photon to have $p_T > 75$ GeV and one of the two jets with highest p_T to be tagged as a b-jet (only one b-jet was allowed). This selection largely reduces the background, being $t\bar{t}_{SM}$ the dominant contribution, as can be seen in Table 3.6. No QCD ($b\bar{b}$) and W+jets events, within the generated statistics, passed the final selection criteria.

$t \to qZ$ channel:

For the $t \to qZ$ channel, the final event selection was done by requiring the leading jet to have $p_T > 30$ GeV. At least one of the two leading jets had to be tagged as a b-jet. Additionally, in order to be compatible with the $Z \to \ell^+\ell^-$ decay, two of the three leptons present in the final state were required to have opposite charges and the same flavour (electron or muon). The dominant contribution for the single top background is the t-channel. No QCD ($b\bar{b}$) and W+jets events passed the final selection criteria, within the generated statistics (3.75×10^8 and 3.5×10^7 events, respectively).

$t \to qg$ channel:

For the "3 jets" ("4 jets") sample of the $t \to qg$ channel, the final event selection was done by requiring the leading non-b-jet to have $p_T > 75$ GeV ($p_T > 100$ GeV) and the reconstructed mass of the two non-b-jets with higher transverse momenta between 125 GeV (150 GeV) and 200 GeV (190 GeV). No generated QCD ($b\bar{b}$) events passed the final selection criteria for both samples.

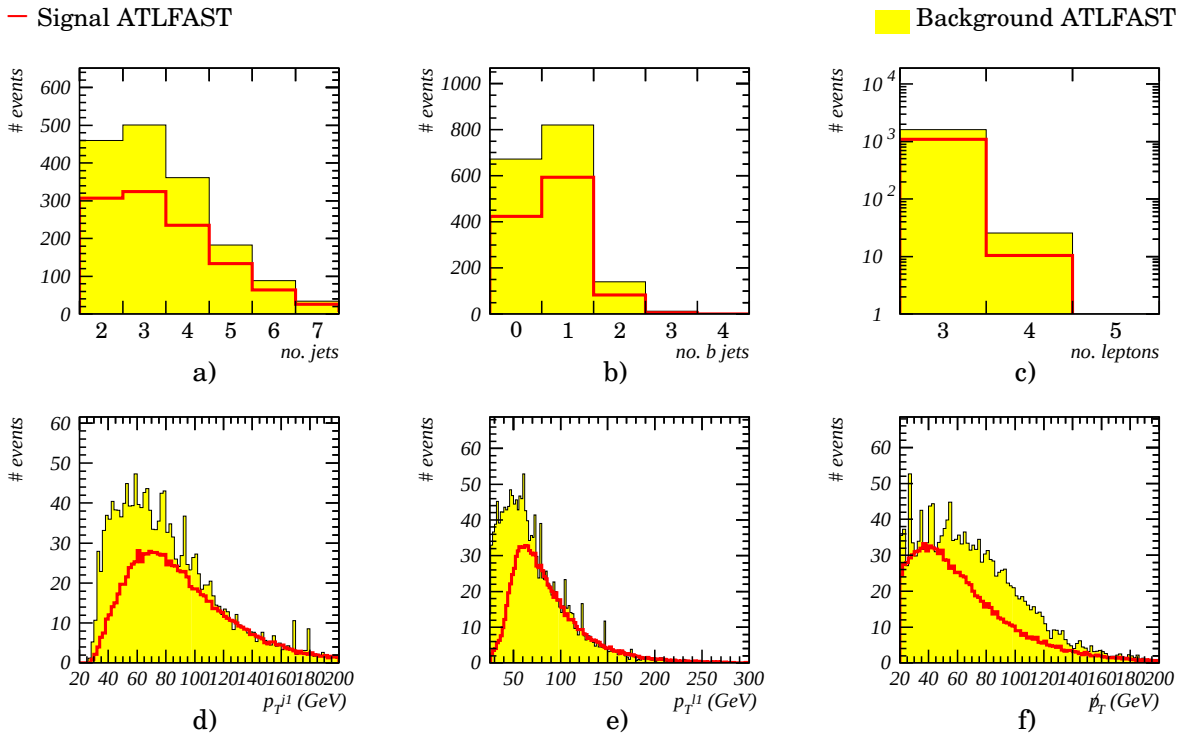

Figure 3.2: The distributions of relevant variables for the $t \to qZ$ channel are shown after the preselection level: a) number of jets, b) number of b-jets, c) number of leptons (log scale), d) transverse momentum of the leading jet ($p_T^{j_1}$), e) transverse momentum of the leading lepton ($p_T^{\ell_1}$) and f) missing transverse momentum ($\not{p}_T$). The SM background is normalised to $L = 10$ fb^{-1} and the signal has an arbitrary normalization, but the same in all plots of this figure.

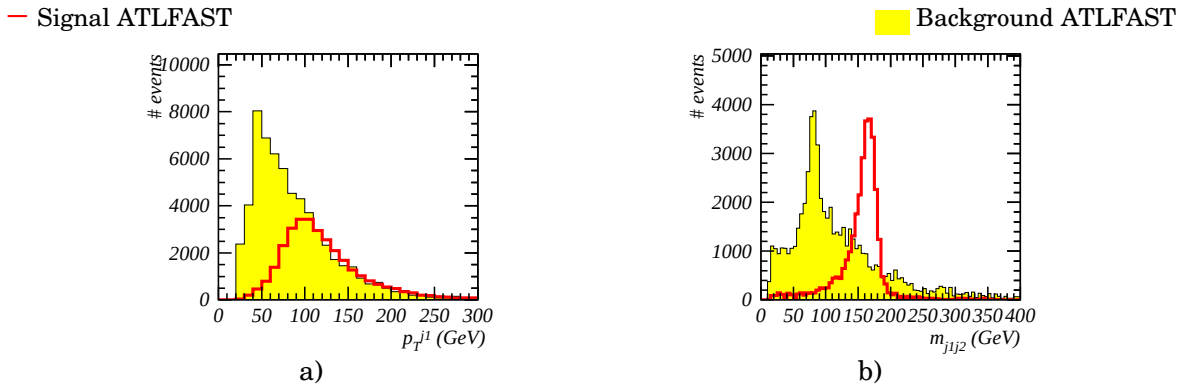

Figure 3.3: The distributions of relevant variables for the $t \to qg$ ("3 jets") channel are shown after the preselection level: a) transverse momentum of the leading non-b-jet ($p_T^{j_1}$), b) the reconstructed mass of the two non-b-jets ($m_{j_1 j_2}$). The SM background is normalised to $L = 10$ fb^{-1} and the signal has an arbitrary normalization, but the same in all plots of this figure.

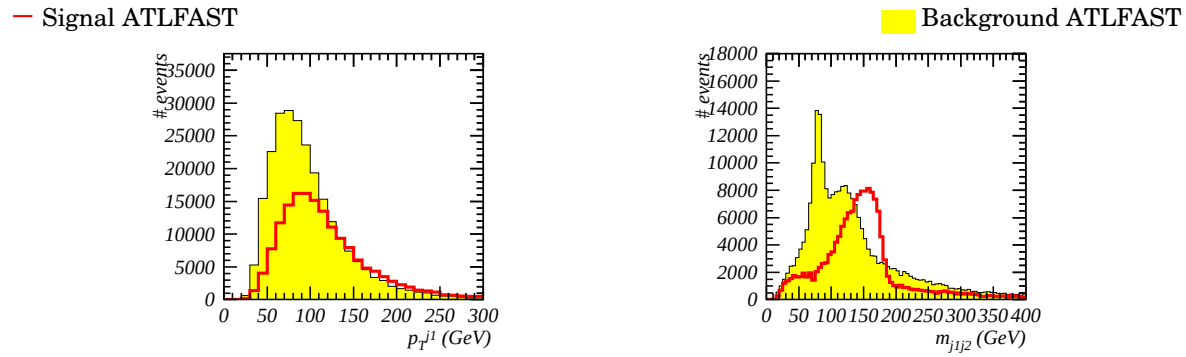

Figure 3.4: The distributions of relevant variables for the $t \to qg$ ("4 jets") channel are shown after the preselection level: a) transverse momentum of the leading non-b-jet ($p_T^{j_1}$) and b) the reconstructed mass of two non-b-jets with highest p_T ($m_{j_1 j_2}$). The SM background is normalised to $L = 10$ fb^{-1} and the signal has an arbitrary normalization, but the same in all plots of this figure.

Number of selected events:

The number of selected background events and the signal efficiency at the final selection level are shown in Table 3.6, for an expected luminosity of 10 fb^{-1}.

Kinematics reconstruction

For all the channels, the top quark with SM semileptonic decay ($t \to b\ell\nu$) cannot be directly reconstructed due to the presence of an undetected neutrino in the final state. Nevertheless, the neutrino four-momentum can be estimated by assuming the missing transverse energy to be the neutrino transverse momentum. The longitudinal component ($p_{z\nu}$) can be determined, with a quadratic ambiguity, by constraining the W mass (calculated as the invariant mass of the neutrino and the most energetic remaining lepton) to its known central value (m_W = 80.4 GeV [99]). Neglecting the lepton mass, the neutrino's longitudinal component $p_{z\nu}$ is given by:

$$\begin{aligned} p_{z\nu} &= \frac{-b \pm \sqrt{b^2 - 4ac}}{2a} \\ a &= \left(\frac{p_{z\ell}}{E_\ell}\right)^2 - 1 \\ b &= 2\left(\frac{p_{x\ell}\,\not{p}_x + p_{y\ell}\,\not{p}_y}{E_\ell} + \frac{m_W^2}{2E_\ell}\right)\frac{p_{z\ell}}{E_\ell} \\ c &= \left(\frac{p_{x\ell}\,\not{p}_x + p_{y\ell}\,\not{p}_y}{E_\ell} + \frac{m_W^2}{2E_\ell}\right)^2 - \not{p}_T^2, \end{aligned} \tag{3.8}$$

where E_ℓ is the lepton's energy; $p_{x\ell}$, $p_{y\ell}$ and $p_{z\ell}$ are the lepton's x, y, and z component, respectively; and $\not{p}_x$ and $\not{p}_y$, are the missing momentum's x and y component, respectively. Due to the resolution of the transverse missing energy, only about 80% of the events have a solution for the neutrino's longitudinal momentum. The top quark is then reconstructed by associating the b-jet with the reconstructed W boson. The quadratic ambiguity was removed

by choosing the solution which gives a top quark mass closer to 175 GeV. The reconstruction of the top quark with FCNC decay depends on the studied channels as follows.

$t \to q\gamma$ channel:

The top quark with FCNC decay in the $t \to q\gamma$ channel was reconstructed using the non-b jet and the photon. In the cases were more than one photon or light jets were available, the one with higher p_T was chosen.

$t \to qZ$ channel:

The reconstruction of the Z mass in the $t \to qZ$ channel, was done by calculating the $\ell^+\ell^-$ invariant mass. In the case where more than one pair of leptons had the same flavour and opposite charges, the pair which had the two leptons with highest p_T was chosen. The reconstruction of the top quark mass which decayed through FCNC was done by associating the non-b jet with the chosen $\ell^+\ell^-$ pair. If more than one non-b jet was present, the one with highest p_T was chosen.

$t \to qg$ channel:

For both "3 jets" and "4 jets" samples of the $t \to qg$ channel, the gluon jet was assumed to be the non-b-jet with the highest transverse momentum. The top quark with FCNC decay was reconstructed from the gluon jet and the light jet with highest p_T (from the remaining ones), *i.e.*, it was reconstructed from the two non-b-jets with higher transverse momenta.

Reconstructed masses:

The obtained distributions of the reconstructed masses of the top quark decaying via FCNC (m_t^{FCNC}), the top quark decaying through SM (m_t^{SM}) and the Z boson (m_Z), for the signal events, are shown in Fig. 3.5. The W boson masses (m_W) are not represented since they were fixed to 80.4 GeV. In order to study the resolution of the kinematics reconstruction, Gaussian functions were fitted to these mass distributions. The obtained values for the Gaussian functions parameters (mass and width of the resonance) are listed in Table 3.7. Due to radiation and jet energy calibration, the reconstructed values for the top quarks are lower than the values used in the generation of the samples (specially in the $t \to qg$ channel, where the combinatorial background between the non b-jets is also important). This effect is not observed in the Z boson since only the charged leptonic decays were considered.

Reconstruction efficiencies:

The reconstruction efficiencies are shown in Table 3.8. Each particle was considered to be well reconstructed if the ΔR distance between the true values and the corresponding reconstructed ones was smaller some fixed value (Table 3.8 shows the results for $\Delta R_{\mathrm{reco}}^{\mathrm{true}} < 0.2$, < 0.4, < 0.8 and < 1.2). It can be seen that the isolated leptons and photons have, as expected by the $\Delta\eta \times \Delta\phi$ ATLAS granularity of 0.1×0.1 ($|\eta| < 3$), high reconstruction efficiency and that in the $t \to qZ$ channel the combinatorial background between the three leptons is about 12%. For jets, composed objects (top quarks and W bosons) and the neutrino reconstruction, the reconstruction efficiencies increase with increasing $\Delta R_{\mathrm{reco}}^{\mathrm{true}}$, as expected. Since the jet clustering was performed within cones of $\Delta R = 0.4$, $\Delta R_{\mathrm{reco}}^{\mathrm{true}} < 0.8$ (2 times higher) was considered as the reference in the interpretation of Table 3.8. The b quarks are correctly identified in about

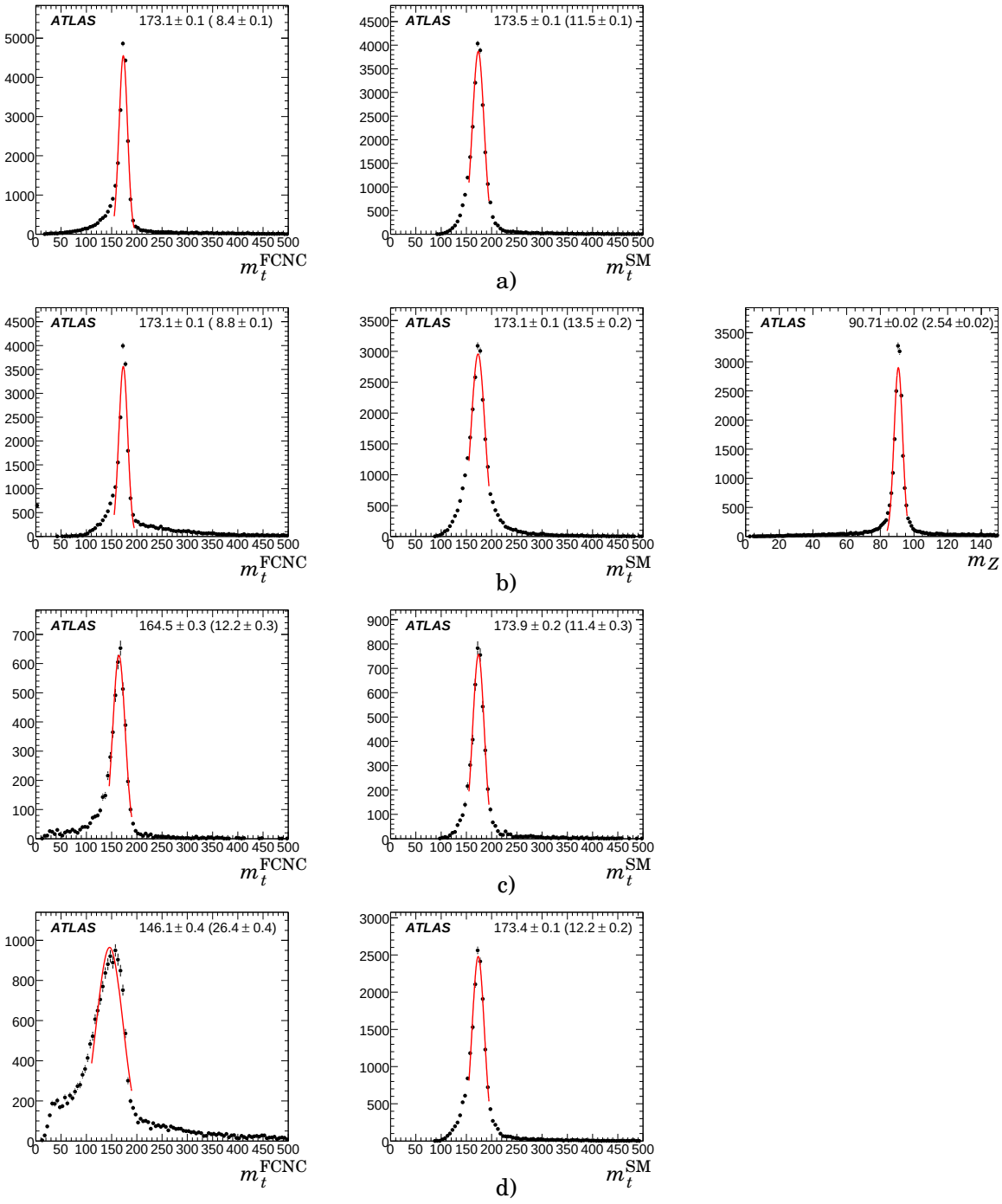

Figure 3.5: Distributions for the simulated signal after the kinematics reconstruction of the a) $t \to q\gamma$, b) $t \to qZ$, c) $t \to qg$ "3 jets" and d) $t \to qg$ "4 jets", of the mass of the reconstructed top quark with FCNC decay (left), the mass of the reconstructed top quark with SM decay (centre) and the mass of the reconstructed Z boson (right, only for the $t \to qZ$ channel). The full lines represent the result of the fitted Gaussian functions to the invariant masses distributions.

	$t \to q\gamma$	$t \to qZ$	$t \to qg$	
			"3 jets"	"4 jets"
m_t^{FCNC}	173.1±0.1	173.1±0.1	164.5±0.3	146.1±0.4
(σ)	(8.4±0.1)	(8.8±0.1)	(12.2±0.3)	(26.4±0.4)
m_t^{SM}	173.5±0.1	173.1±0.1	173.9±0.2	173.4±0.1
(σ)	(11.5±0.1)	(13.5±0.2)	(11.4±0.3)	(12.2±0.2)
m_Z		90.71±0.02		
(σ)		(2.54±0.02)		

Table 3.7: The values of the masses and widths of the top quark decaying via FCNC (m_t^{FCNC}), the top quark decaying through SM (m_t^{SM}) and the Z boson (m_Z), for the simulated signal events, obtained by fitting Gaussian functions to the respective distributions.

90% of the cases. The light quarks have efficiencies higher than 70% for the $t \to q\gamma$ and the $t \to qZ$ channels, while for the two $t \to qg$ channels the values are smaller because it was assumed that the gluonic jet was more energetic than the light jet. Nevertheless, the reconstruction efficiency of the top quark decaying via FCNC is similar for the $t \to q\gamma$ and $t \to qg$ "3 jets" channels, where the small inefficiency comes from the b-jet mistag. As expected, for the $t \to qZ$ and $t \to qg$ "4 jets"channels the efficiencies are smaller due to the combinatorial background between the three leptons and between the three non b-jets, respectively. The neutrino is well reconstructed in about 70% of the cases for all channels but the $t \to qZ$, where the combinatorial background between the three leptons, decreases the reconstruction efficiency to about 65%. The top quark with SM decay and the W boson have similar reconstruction efficiencies (about 80%), and again, they are higher than those for the $t \to qZ$ channel.

Discriminant analysis

Following the final selection, a likelihood-based type of analysis was applied. Signal and background probabilities were computed for each event, $\mathscr{P}_S$ and $\mathscr{P}_B$ respectively. The ratio between these two probabilities discriminates the signal-like events from the background-like ones.

The probabilities were computed using probability density functions (pdf[1]), constructed from relevant physical variables. Assuming uncorrelated variables, the probabilities for each event are:

$$\mathscr{P}_S = \prod_{i=1}^{n} P_i^S(x_i), \qquad \mathscr{P}_B = \prod_{i=1}^{n} P_i^B(x_i), \tag{3.9}$$

where n is the number of used pdf and P_i^S (P_i^B) is the probability of a event to have the x_i value for the physical variable i, which corresponds to the signal (background) pdf. Figure 3.6 shows an example for illustration purposes. The discriminant variable L_R is defined as

$$L_R = \ln\left(\frac{\mathscr{P}_S}{\mathscr{P}_B}\right). \tag{3.10}$$

The L_R value for signal-like events is higher than for background-like events.

[1]These probability density functions (pdf) should not be confused with the parton density functions (PDF).

$\Delta R_{\text{reco}}^{\text{true}}$	<0.2	<0.4	<0.8	<1.2
$t \to q\gamma$:				
ε_q	74.2 ± 0.5	80.4 ± 0.5	84.2 ± 0.6	85.9 ± 0.6
ε_γ	99.3 ± 0.6	99.8 ± 0.6	99.9 ± 0.6	99.9 ± 0.6
$\varepsilon_{t^{\text{FCNC}}}$	71.8 ± 0.5	81.1 ± 0.5	88.3 ± 0.6	92.0 ± 0.6
ε_b	84.9 ± 0.6	90.1 ± 0.6	93.0 ± 0.6	93.9 ± 0.6
ε_ℓ	98.8 ± 0.6	99.7 ± 0.6	99.9 ± 0.6	100.0 ± 0.6
ε_ν	27.0 ± 0.3	48.9 ± 0.4	70.1 ± 0.5	79.6 ± 0.6
ε_W	43.4 ± 0.4	62.4 ± 0.5	79.6 ± 0.5	88.8 ± 0.6
$\varepsilon_{t^{\text{SM}}}$	49.1 ± 0.4	67.9 ± 0.5	84.0 ± 0.6	90.7 ± 0.6
$t \to qZ$:				
ε_q	66.4 ± 0.5	72.0 ± 0.5	75.6 ± 0.5	77.5 ± 0.5
ε_Z	79.2 ± 0.5	82.6 ± 0.6	86.5 ± 0.6	89.8 ± 0.6
$\varepsilon_{t^{\text{FCNC}}}$	54.4 ± 0.5	63.8 ± 0.5	73.9 ± 0.5	80.3 ± 0.6
ε_b	81.4 ± 0.6	87.3 ± 0.6	90.5 ± 0.6	91.6 ± 0.6
ε_ℓ	86.1 ± 0.6	87.4 ± 0.6	88.3 ± 0.6	89.2 ± 0.6
ε_ν	24.3 ± 0.3	44.5 ± 0.4	64.7 ± 0.5	75.0 ± 0.6
ε_W	30.8 ± 0.3	46.3 ± 0.4	62.3 ± 0.5	72.5 ± 0.5
$\varepsilon_{t^{\text{SM}}}$	35.8 ± 0.4	52.0 ± 0.4	69.0 ± 0.5	78.6 ± 0.5
$t \to qg$ "3 jets":				
ε_q	37.7 ± 0.8	40.8 ± 0.9	43.7 ± 0.9	46.3 ± 0.9
ε_g	45.7 ± 0.9	48.1 ± 1.0	49.4 ± 1.0	50.8 ± 1.0
$\varepsilon_{t^{\text{FCNC}}}$	67.1 ± 1.1	81.1 ± 1.2	89.2 ± 1.3	92.7 ± 1.3
ε_b	85.3 ± 1.3	89.4 ± 1.3	91.6 ± 1.3	92.5 ± 1.3
ε_ℓ	99.8 ± 1.4	100.0 ± 1.4	100.0 ± 1.4	100.0 ± 1.4
ε_ν	26.7 ± 0.7	48.4 ± 1.0	70.0 ± 1.2	79.8 ± 1.3
ε_W	43.9 ± 0.9	62.5 ± 1.1	80.0 ± 1.2	89.0 ± 1.3
$\varepsilon_{t^{\text{SM}}}$	46.5 ± 0.9	66.1 ± 1.1	82.3 ± 1.3	88.9 ± 1.3
$t \to qg$ "4 jets":				
ε_q	24.3 ± 0.4	29.1 ± 0.4	34.7 ± 0.4	40.5 ± 0.5
ε_g	32.6 ± 0.4	40.0 ± 0.5	44.7 ± 0.5	48.8 ± 0.5
$\varepsilon_{t^{\text{FCNC}}}$	35.9 ± 0.4	54.4 ± 0.5	72.2 ± 0.6	80.8 ± 0.7
ε_b	77.5 ± 0.6	84.4 ± 0.7	89.3 ± 0.7	90.8 ± 0.7
ε_ℓ	98.5 ± 0.8	99.6 ± 0.8	99.9 ± 0.8	100.0 ± 0.8
ε_ν	25.6 ± 0.4	47.1 ± 0.5	68.0 ± 0.6	78.2 ± 0.7
ε_W	42.0 ± 0.5	61.0 ± 0.6	78.8 ± 0.6	88.3 ± 0.7
$\varepsilon_{t^{\text{SM}}}$	45.5 ± 0.5	64.0 ± 0.6	80.7 ± 0.7	88.4 ± 0.7

Table 3.8: The obtained efficiencies of the kinematics reconstruction for each FCNC channel, after the preselection, for four different matching criteria: $\Delta R_{\text{reco}}^{\text{true}} < 0.2$, < 0.4, < 0.8 and < 1.2.

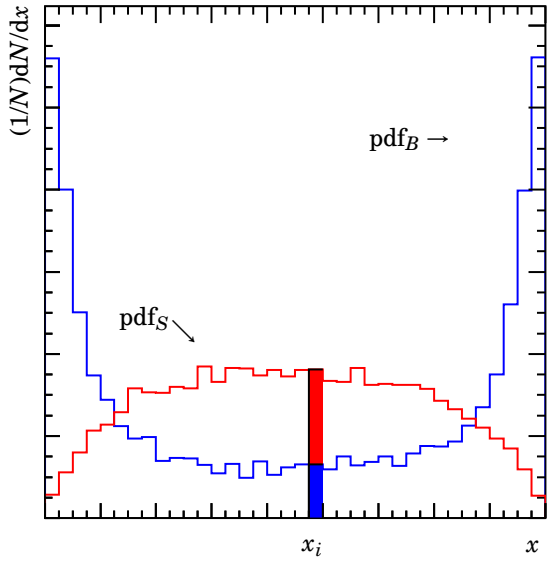

Figure 3.6: An example of computation of the signal and background probabilities discriminant variables is shown. Both distributions are normalised to 1. For this case, the signal-like probability of the event is higher than the background-like probability.

In order to maximise the discrimination, the physical variables, from which the pdf are build, should have different distributions for signal and background. Several physical variables were studied and compared. The chosen ones for each channel (usually momenta, masses or angles between objects) are listed below.

$t \to q\gamma$ channel:

For the $t \to q\gamma$ channel, the probability density functions were built from the following variables (which are shown in Figure 3.7):

- the mass of the top quark with FCNC decay (m_t^{FCNC});
- the transverse momentum of the leading photon (p_T^{γ}) and
- the number of jets.

$t \to qZ$ channel:

For the $t \to qZ$ channel, the probability density functions were constructed from the following physical distributions (see Figure. 3.8):

- minimum invariant mass ($m_{\ell\ell}^{\mathrm{min}}$) of the three possible combinations of two leptons (only the three leading leptons were considered),
- transverse momentum of the third lepton ($p_T^{\ell_3}$),
- the mass of the top quark with FCNC decay (m_t^{FCNC}),
- the transverse momentum of the light quark (p_T^{q}).

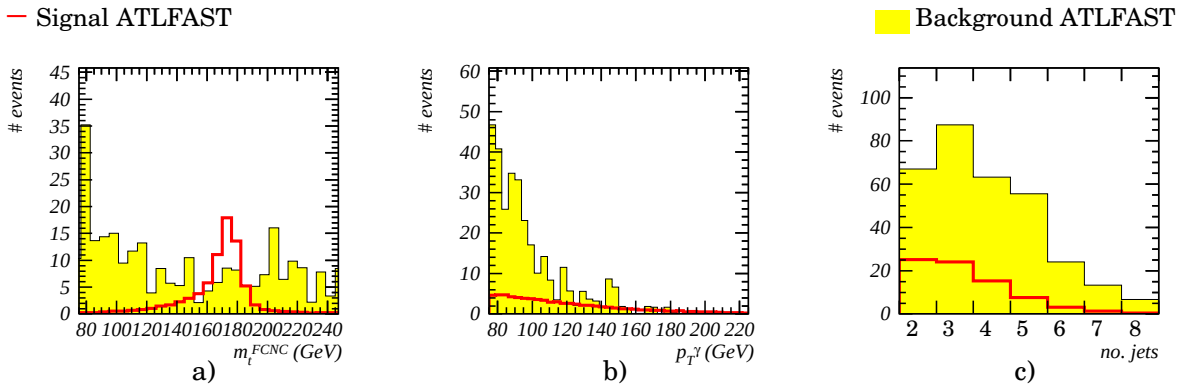

Figure 3.7: The distribution of the variables from which the probability density functions were built are shown (for the $t \to q\gamma$ channel): a) mass of the reconstructed top quark with FCNC decay (m_t^{FCNC}), b) transverse momentum of the photon p_T^{γ}) and c) number of jets. The SM background is normalised to $L = 10$ fb^{-1} and the signal has an arbitrary normalization, but the same in all plots of this figure.

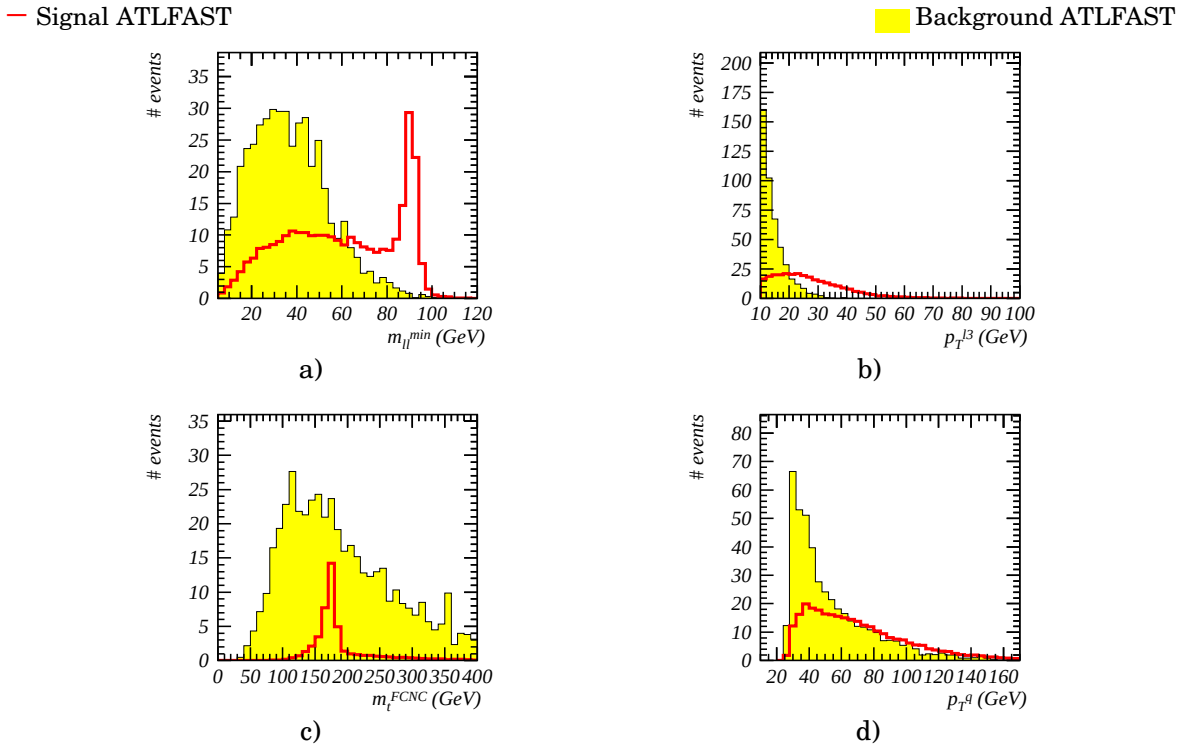

Figure 3.8: The distribution of the variables based on which the probability density functions were built are shown (for the $t \to qZ$ channel): a) minimum invariant mass ($m_{\ell\ell}^{\mathrm{min}}$) of the three possible combinations of two leptons (only the first three leptons were considered), b) transverse momentum of the third lepton ($p_T^{\ell_3}$), c) mass of the top quark with FCNC decay (m_t^{FCNC}) and d) the transverse momentum of the light quark (p_T^q). The SM background is normalised to $L = 10$ fb^{-1} and the signal has an arbitrary normalization, but the same in all plots of this figure.

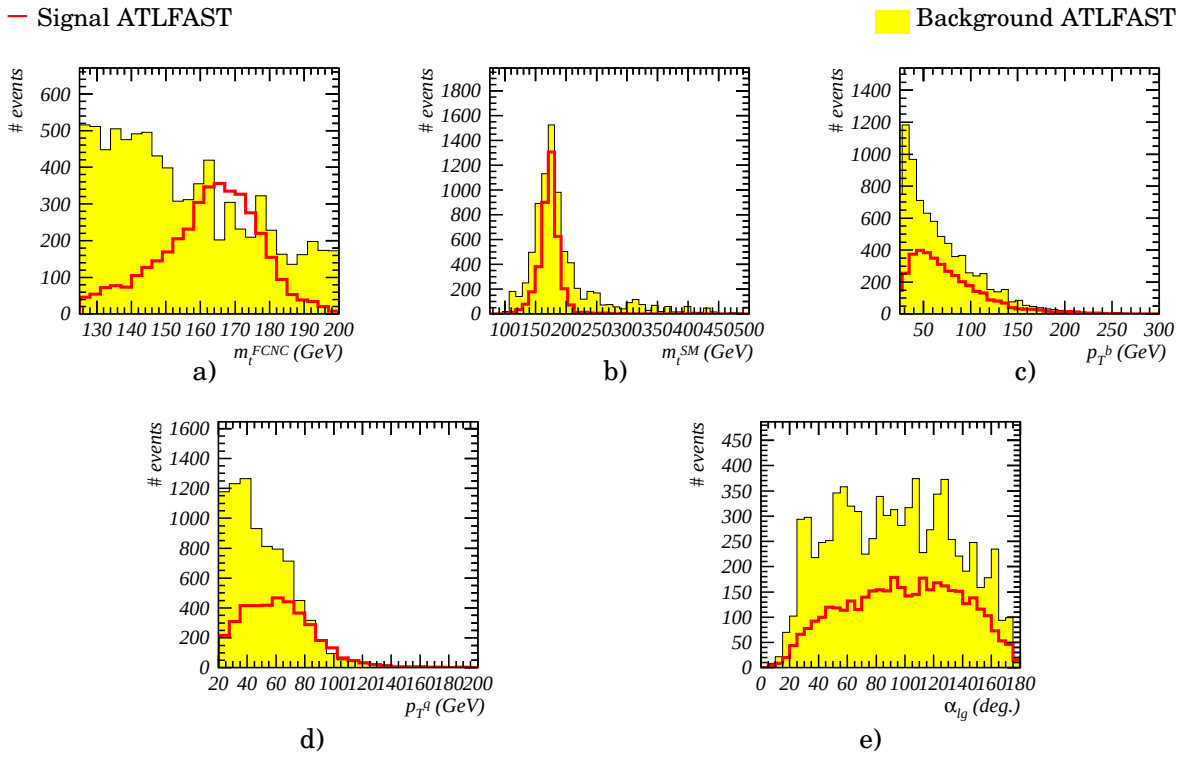

Figure 3.9: The distribution of the variables based on which the probability density functions were built are shown (for the $t \to qg$ channel "3 jets"): a) the mass of the top quark with FCNC decay (m_t^{FCNC}), b) the mass of the top quark with SM decay (m_t^{SM}), c) transverse momentum of the b quark (p_T^b), d) transverse momentum of the light quark (p_T^q) and e) angle between the lepton and the gluon ($\alpha_{\ell g}$). The SM background is normalised to $L = 10$ fb^{-1} and the signal has an arbitrary normalization, but the same in all plots of this figure.

$t \to qg$ channel:

As for the other channels, a likelihood-based type of analysis was adopted for the $t \to qg$ "3 jets" channel, using the following variables to build the probability density functions (*c.f.* Figure 3.9):

- the mass of the top quark with FCNC decay (m_t^{FCNC}),
- the mass of the top quark with SM decay (m_t^{SM}),
- transverse momentum of the b quark (p_T^b),
- transverse momentum of the light quark (p_T^q) and
- angle between the lepton and the gluon ($\alpha_{\ell g}$).

Finally, for the $t \to qg$ "4 jets" channel, the probability density functions were computed from the following physical distributions (shown in Figure 3.10):

- minimum invariant mass of the leading and the second non-b jets or the leading and the third non-b jets (m_{gj}),
- the mass of the top quark with SM decay (m_t^{SM}),

- transverse momentum of the top quark with FCNC decay ($p_T^{t^{\text{FCNC}}}$),
- transverse momentum of the top quark with SM decay ($p_T^{t^{\text{SM}}}$),
- angle between the lepton and the gluon ($\alpha_{\ell g}$),
- angle between the lepton and the b quark ($\alpha_{\ell b}$) and
- angle between the gluon and the light quark (α_{gq}).

The discriminant variables distributions for the four FCNC topologies are shown in Figure 3.11. The distributions of the number of expected SM background events as a function of the signal efficiency, obtained by cutting on the discriminant variable of each FCNC channel, is shown in Figure 3.12.

3.4 Results and systematic uncertainties

The expected top quark FCNC decay branching ratios sensitivities of the ATLAS experiment were estimated under two different hypothesis, as explained next.

BR sensitivity (5σ significance discovery hypothesis)

Assuming a signal discovery with a 5σ significance, the branching ratio (BR) sensitivity for each channel studied is estimated by:

$$BR = \frac{5\sqrt{B \times \varepsilon_\ell}}{2 \times L \times \sigma(t\bar{t}_{SM}) \times \varepsilon_s \times \varepsilon_\ell}, \tag{3.11}$$

where $\sigma(t\bar{t}_{SM}) = 833$ pb [71] is the NLO calculation of the SM cross-section for $t\bar{t}$ production in pp collisions at $\sqrt{s} = 14$ TeV. B is the total number of selected background events, ε_s is the signal efficiency convoluted with the appropriate branching ratios and $\varepsilon_\ell = 0.9^n$ is the charged leptons identification efficiency (n is the number of leptons required for each channel). The factor 2 in the denominator takes into account the t and $\bar{t}$ contributions to the BR. L is the luminosity of data samples.

The expected branching ratio sensitivities were evaluated after applying cuts to the discriminant variables, as given in Table 3.9 (see also Figure 3.12). These cuts were optimised according to the best $S/\sqrt{B}$ (S is the number of selected signal events). The expected branching ratio sensitivities for the 5σ discovery are shown in Table 3.10.

95% confidence level limits (hypothesis of absence of signal)

In the absence of a FCNC top quark decay signal, expected limits at 95% CL can be derived. With data, these upper limits on the number of signal events for each channel can be determined by fitting the discriminant variables obtained from the data events with those for the hypothesis of signal plus background, without doing any cuts on the distributions (more details can be found in [100, 101]). For that purpose, a test-statistic, which characterises the data with background and signal, was done:

$$X_d = \sum_i n_i \ln\left(1 + \frac{s_i}{b_i}\right) \tag{3.12}$$

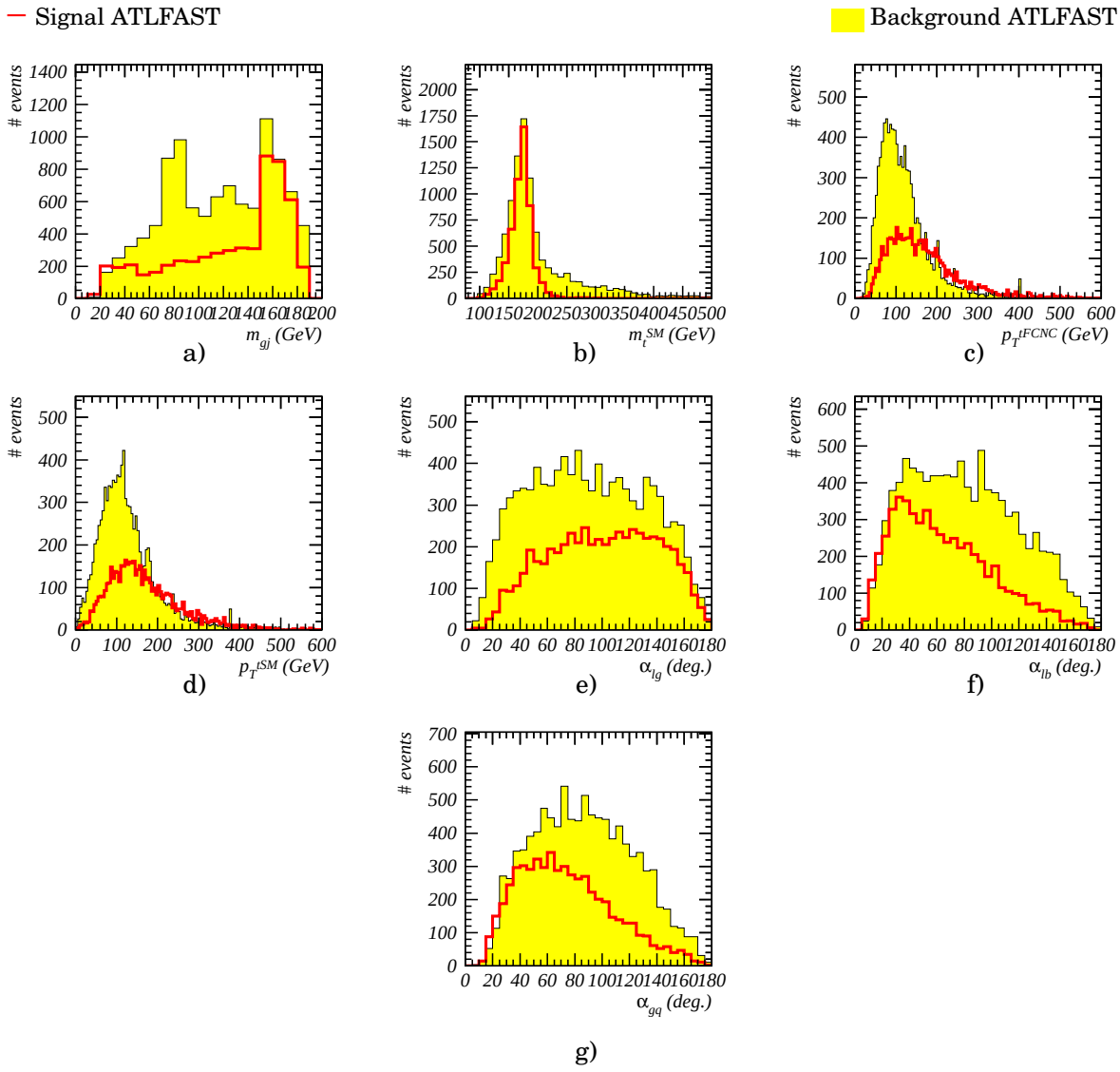

Figure 3.10: The distribution of the variables based on which the probability density functions were built are shown (for the $t \to qg$ channel "4 jets"): a) minimum invariant mass of the first and the second non-b jets or the first and the third non-b jets, b) the mass of the top quark with SM decay (m_t^{SM}), c) transverse momentum of the top quark with FCNC decay ($p_T^{t^{\mathrm{FCNC}}}$), d) transverse momentum of the top quark with SM decay ($p_T^{t^{\mathrm{SM}}}$), e) angle between the lepton and the gluon ($\alpha_{\ell g}$), f) angle between the lepton and the b quark ($\alpha_{\ell b}$) and g) angle between the gluon and the light quark (α_{gq}). The SM background is normalised to $L = 10$ fb^{-1} and the signal has an arbitrary normalization, but the same in all plots of this figure.

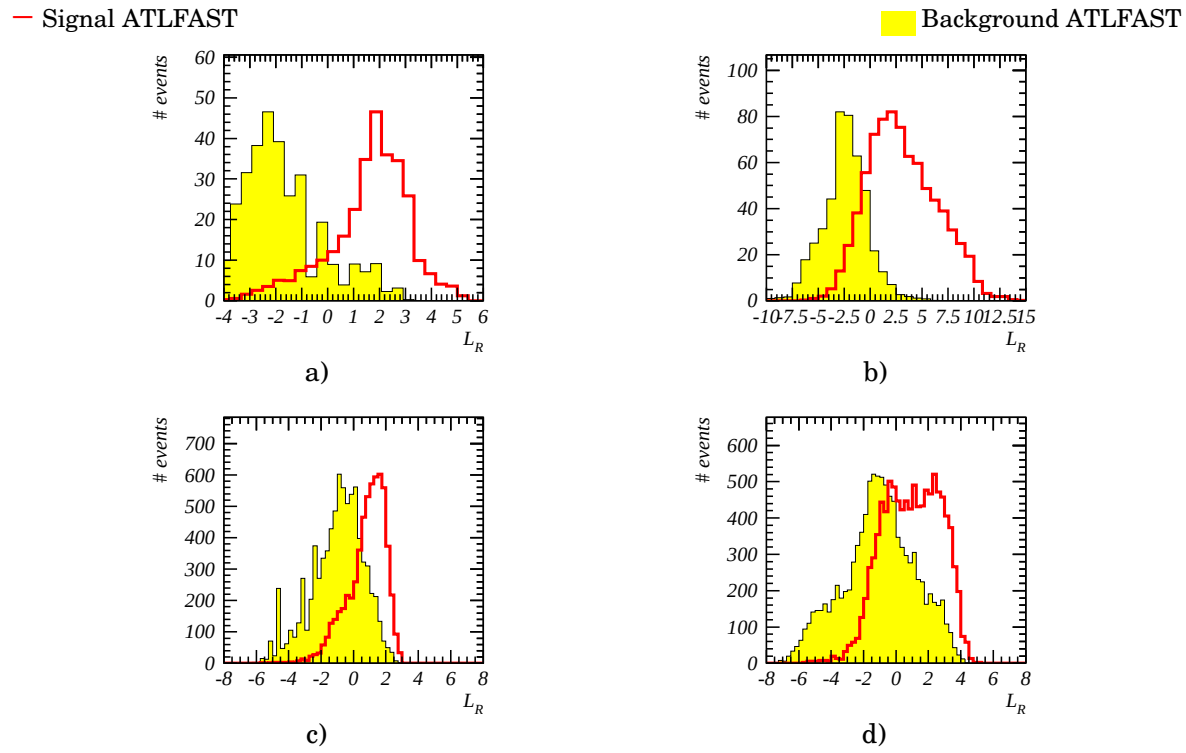

Figure 3.11: SM background and signal discriminant variable distributions for the a) $t \to q\gamma$, b) $t \to qZ$, c) $t \to qg$ "3 jets" and c) $t \to qg$ "4 jets" channels are shown. The SM background is normalised to $L = 10$ fb^{-1} and the signal has an arbitrary normalization.

channel		L_R cut	B	ε_s
$t \to q\gamma$		$> +2.71$	3.48	0.62%
$t \to qZ$		$> +5.62$	0.50	0.06%
$t \to qg$	"3 jets"	$> +1.13$	734.1	0.20%
	"4 jets"	> -0.38	4033.9	0.29%

Table 3.9: The number of selected background events (normalised to $L = 10$ fb^{-1}) and signal efficiencies (convoluted with the appropriate branching ratios), for each channel of the likelihood-based analyses, after the specified L_R cut, are shown.

channel		BR ($L = 10$ fb^{-1})	BR ($L = 100$ fb^{-1})
$t \to q\gamma$		9.4×10^{-5}	3.0×10^{-5}
$t \to qZ$		4.4×10^{-4}	1.4×10^{-4}
$t \to qg$	"3 jets"	4.3×10^{-3}	1.4×10^{-3}
	"4 jets"	6.9×10^{-3}	2.2×10^{-3}

Table 3.10: The branching ratio sensitivity, for each channel, in the 5σ discovery hypothesis, is shown. The results for a luminosity of $L = 10$ and 100 fb^{-1}, obtained after applying the cuts described in Table 3.9, are presented.

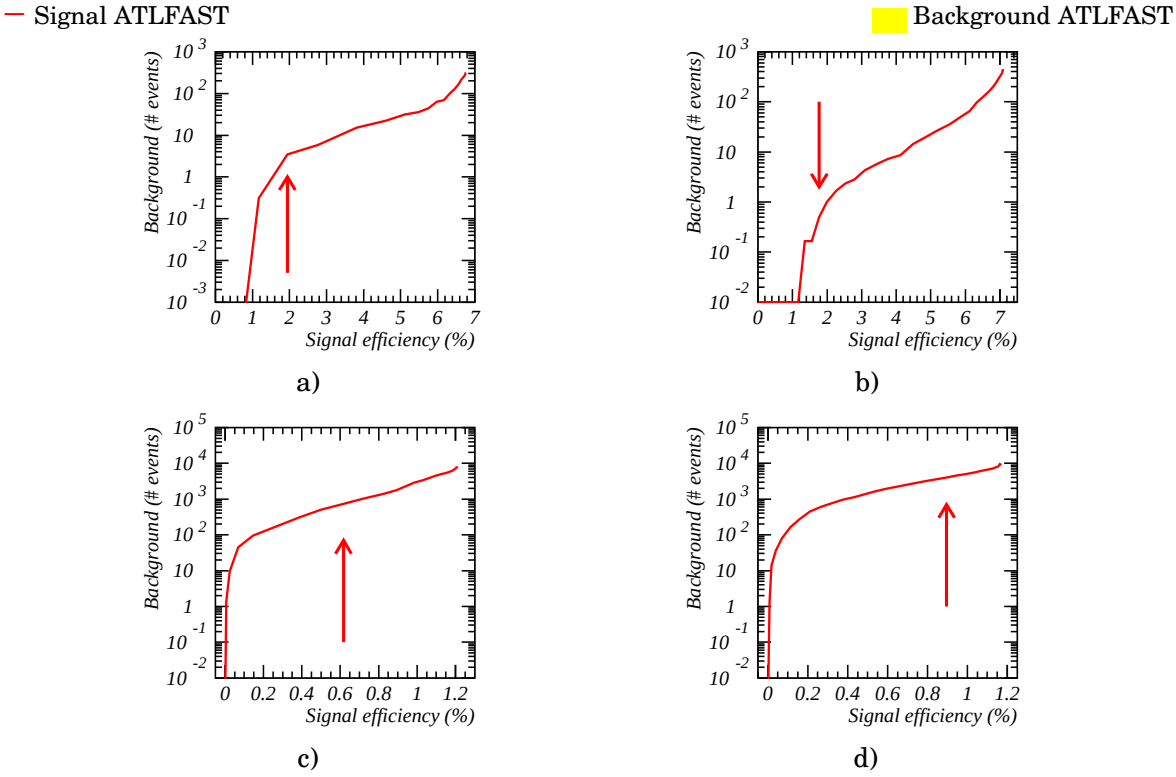

Figure 3.12: The number of expected SM background as a function of the signal efficiency for the a) $t \to q\gamma$, b) $t \to qZ$, c) $t \to qg$ "3 jets" and d) $t \to qg$ "4 jets" channels, is shown. The SM background is normalised to $L = 10$ fb^{-1}. The arrows show the points with best $S/\sqrt{B}$.

where i runs over all the bins of all the discriminant variables and n_i, s_i and b_i are the number of events in bin i of the discriminant variables in the data, the expected background and the signal events, respectively. When data events are more similar to the signal events, the X_d variable takes higher values.

The X_d statistical test is then compared with similar statistical tests obtained for the hypotheses of signal plus background (X_{s+b}) and background only (X_b). For the signal plus background hypothesis, the X_{s+b} distribution was computed iteratively, by simulating statistically compatible distributions with the sum of the signal and the background discriminant variables. The statistical fluctuations were performed with Poisson distributions and in each iteration, X_{s+b} was computed as:

$$X_{s+b} = \sum_i n_i^{(s+b)} \ln\left(1 + \frac{s_i}{b_i}\right), \tag{3.13}$$

where, $n_i^{(s+b)}$ is the total number of events in the simulated distributions. A similar method was used to obtain the X_b statistical test:

$$X_b = \sum_i n_i^{(b)} \ln\left(1 + \frac{s_i}{b_i}\right), \tag{3.14}$$

in which $n_i^{(b)}$ is the total number of events in the simulated distributions of the background discriminant variables.

In the modified frequentist likelihood method, the confidence level (CL) of the extracted limit is defined as [100, 101]:

$$1 - CL = \frac{\int_0^{X_d} P_{s+b}(X)\mathrm{d}X}{\int_0^{X_d} P_b(X)\mathrm{d}X}, \tag{3.15}$$

where P_{s+b} and P_b are the X_{s+b} and X_b distributions, respectively. Figure 3.13 shows comparisons of the statistical tests distributions for the signal plus background (X_{s+b}) and background only (X_b) with the X_d data statistical test, for four different cases. The 95% CL observed limit is the value for which expression 3.15 is equal to 0.05.

The expected limit is the one which would be obtain if the data events were perfectly described by the expected background and was computed by replacing X_d with the median of the statistical test for the background hypothesis (X_b). Using the NLO calculation for $\sigma(t\bar{t}_{SM})$, these expected limits on the number of signal events were then converted into limits on the branching ratio for each of the studied FCNC top quark decay channels. The expected 95% confidence level limits on the branching ratios are summarised in Table 3.11. The charged lepton identification efficiency was set to 90%.

Systematic uncertainties and analyses stability

The effect of different systematic sources of uncertainty on the limits evaluation was studied. This estimation was done by considering the changes on the central values of the signal efficiency, number of background events and likelihood ratio distributions. The following systematic uncertainties were considered:

- The effect of the top mass uncertainty was evaluated using different MC samples with m_t = 170 GeV and m_t = 180 GeV. This systematic uncertainty affects both the event kinematics (and consequently the discriminant variables shape) and the value of the $t\bar{t}$ cross-section (used in the limits evaluation).

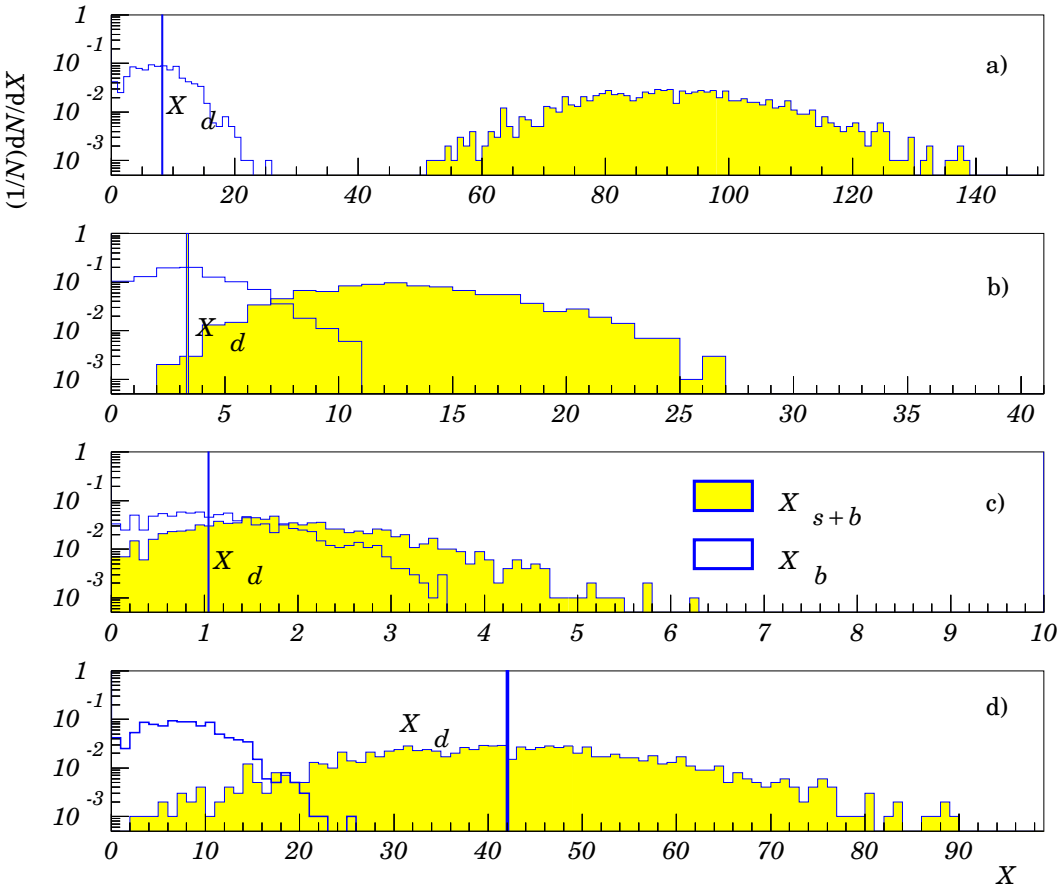

Figure 3.13: Schematic comparisons of the statistical tests distributions for the signal plus background (X_{s+b}) and background only (X_b) with the X_d data statistical test. The figure shows four cases: a) complete exclusion of the signal hypothesis, b) 5% CL exclusion of the signal hypothesis, c) inability to exclude the signal hypothesis and d) signal hypothesis confirmed. The vertical line represents X_d. (Adapted from [100])

		-1σ	expected	$+1\sigma$
$L = 10$ fb^{-1}:				
$t \to q\gamma$		2.5×10^{-5}	4.1×10^{-5}	6.2×10^{-5}
$t \to qZ$		2.2×10^{-4}	3.1×10^{-4}	4.3×10^{-4}
	"3 jets"	1.0×10^{-3}	1.6×10^{-3}	2.3×10^{-3}
$t \to qg$	"4 jets"	1.5×10^{-3}	2.4×10^{-3}	3.5×10^{-3}
	combined	8.2×10^{-4}	1.3×10^{-3}	1.9×10^{-3}
$L = 100$ fb^{-1}:				
$t \to q\gamma$		6.6×10^{-6}	1.2×10^{-5}	1.7×10^{-5}
$t \to qZ$		4.1×10^{-5}	6.1×10^{-5}	8.7×10^{-5}
	"3 jets"	6.5×10^{-4}	4.8×10^{-4}	7.1×10^{-4}
$t \to qg$	"4 jets"	4.8×10^{-4}	7.5×10^{-4}	1.1×10^{-3}
	combined	2.7×10^{-4}	4.2×10^{-4}	6.6×10^{-4}

Table 3.11: The expected 95% confidence level limits on the FCNC top quark decay branching ratios, in the absence of signal hypothesis, are shown. The results for a luminosity of $L = 10$ and 100 fb^{-1} are presented. The central values are presented together with the 1σ bands, which include the contribution from the statistical and systematic uncertainties.

- The overall theoretical uncertainty on $\sigma(t\bar{t})$ was estimated in reference [33]. The effect of this uncertainty was studied by allowing a change of 12% on the central value of $\sigma(t\bar{t})$, the cross-section used both in the $t\bar{t}_{SM}$ background normalisation and in the BR limits evaluation, assuming a negligible error on the measurement itself. If the error on the cross-section measurement is, for instance, 5%, the ATLAS sensitivity will be degraded but the change will not affect the order of magnitude of the results. For the $t \to qZ$ and the $t \to q\gamma$ channels, a 5% error gives a maximum change on the limit of 5%. For the $t \to qg$ channels, where the expected number of background events is more important, the limit can change by a factor 2 to 3 (depending if it is the 3 or 4 jets topology). A precise measurement of the $t\bar{t}$ cross-section is, for this reason, of utmost importance.

- The CTEQ 5L PDF set was used in the Monte Carlo generation. A different PDF set (CTEQ 4M) was used to estimate the effect of this choice of PDF on the event kinematics.

- As mentioned in section 3.2, the ATLFAST-B package was used to simulate the b-tag algorithm with a b-tag efficiency of 60%. In order to study the impact of an algorithm with a different efficiency, the b-tagging efficiencies of 50% and 70%, with the corresponding contamination factors for c-jets and light jets, were also considered. This source of uncertainty affects the signal efficiency, background estimation and discriminant variable shapes.

- The impact of the knowledge of the absolute jet energy scale was estimated by recalibrating the reconstructed jet energy. A miscalibration of $\pm 1\%$ for light jets and $\pm 3\%$ for b-jets was used. This uncertainty was found to have a negligible effect on the signal efficiency, background estimation and discriminant variable shapes. A jet energy miscalibration of $\pm 5\%$ for all jets was also considered. For the $t \to qZ$, $t \to q\gamma$ and $t \to qg$ ("3 jets") channels

channel	$t \to q\gamma$	$t \to qZ$	$t \to qg$	
			"3 jets"	"4 jets"
systematic uncertainties:				
top mass	18%	13%	8%	7%
$\sigma(t\bar{t})$	11%	11%	9%	7%
PDF choice	15%	7%	3%	6%
b-tag algorithm efficiency	16%	5%	18%	17%
jet energy calibration	2%	1%	2%	3%
total	30%	19%	22%	21%
analysis stability:				
selection criteria	9%	12%	3%	13%
pdf choice	10%	15%	1%	2%

Table 3.12: Absolute value of the maximum relative changes on the expected 95% confidence level limits for each FCNC top quark decay branching ratio evaluated with the likelihood-based analyses. The reference values were presented in Table 3.11 (for $L = 10$ fb^{-1}).

the relative changes on the 95% CL expected limits were found to be under 7%. For the most difficult channel ($t \to qg$ "4 jets") this effect is more important (up to 12%), due to the tighter selection criteria used to reject the large contribution from background.

The stability of the selection criteria was studied by changing the preselection and final selection (typically a ±10% variation on the cut values was considered). The discriminant variables were computed using the probability density function sets described in section 3.3. In order to estimate the effect of a different pdf set, the following changes were studied: in the $t \to qZ$ channel, the top quark with FCNC decay reconstruction was done by considering the jet closest to the reconstructed Z boson. Similarly, the top quark with FCNC decay mass reconstruction in the $t \to q\gamma$ channel was done using the jet closest to the leading photon. Moreover, the top quark with SM decay mass was included in the probability density functions set and the multiplicity of jets with $|\eta| < 2.5$ was chosen as a pdf (instead of the jet multiplicity). In the $t \to qg$ channel, ΔR was used instead of the angles in the pdf definition.

The absolute value of the maximum relative effect on the 95% confidence level expected limits on each considered source of systematic uncertainty (the reference values are those presented in Table 3.11) is shown in Table 3.12 (for $L = 10$ fb^{-1}). Although differences up to 20% were observed (caused by the uncertainty on the top quark mass), the order of magnitude of the expected limits on the BR is not affected by any of the systematic uncertainties considered. Moreover, the change on the selection criteria and on the probability density functions sets do not have a significant impact on the results.

4

Analyses with low luminosity

During the first data taking period the performance of the ATLAS detector will not be the final one. Complex tools like, for example, the b-tagging, may not be available. The algorithms for the identification of isolated particles may also be no yet optimised. It is also possible that some of the backgrounds can have cross-sections different from the theoretical predictions. The full simulation allows to study the performance of the detector with detail and accuracy. In order to study the ATLAS sensitivity to the FCNC top quark decays in $t\bar{t}$ events with an integrated luminosity of only 1 fb^{-1}, the full simulation of the detector was used. New analyses without b-tag were developed. This chapter is organised has the previous one. It starts by describing the MC samples used and the ATLAS full simulation. The new analyses are then explained, and finally a discussion about the obtained results, as well the systematic uncertainties and the analyses stability is presented. The work presented in this chapter is also described in [102].

4.1 Signal and background generation

Samples of $t\bar{t}$, with one of the top quarks decaying via SM and the other through FCNC, and SM background events were generated and simulated within the ATLAS software framework ATHENA 12 [103]. A detailed GEANT4 simulation of the detector was used. The samples used are a part of the ATLAS CSC (Computing System Commissioning) data.

The signal event samples used in this analysis are the ones corresponding to $t\bar{t} \rightarrow b\ell\nu qX$ channels, where $X = \gamma, Z \rightarrow \ell\ell, g$, and $\ell = e, \mu$ (due to limited computational resources, the decays into taus, which were considered in Chapter 3, but have a small efficiency, were not generated) presented in Table 4.1, and were generated using the TopReX [92] package. The hadronisation was handled by PYTHIA [104].

The other samples of Table 4.1 were considered as background. Background events coming from $W + n$ partons, $Wc\bar{c} + n$ partons and $Wb\bar{b} + n$ partons were generated with AlpGen 2.06[105] interfaced with HERWIG 6.510 [106]. In order to reduce the computational resources needed to generate, simulate and store these samples, only the leptonic decays of the W bosons were considered. Additionally, in the $W+n$ partons sample, only the generated events with at least three true jets with $p_T > 30$ GeV were simulated. The Z+jets events were generated using the PYTHIA library. Only the $Z \rightarrow \ell^+\ell^-$ (electrons and muons with p_T >10 GeV and taus with $p_T > 5$ GeV) decays were considered. Only the events with $m_{\ell^+\ell^-}$ >60 GeV were simulated. HERWIG was also used to generate WZ pairs events with at least one true electron

or a muon with p_T >10 GeV. Generation of SM $t\bar{t}$ events was done using the NLO generator MC@NLO 3.1 [107]. Partons were fragmented and hadronized using HERWIG linked with the multiple parton scattering generator JIMMY [108, 109]. The three channels of the single top quark production were generated with AcerMC [110]. The t-channel was generated by combining LO and NLO diagrams, while the s and the Wt channels were generated at LO. Only the leptonic decays of the W bosons ($W \to e\nu_e, \mu\nu_\mu, \tau\nu_\tau$) were allowed, except in the Wt channel, where one of W was forced to decay hadronically and the other one to decay leptonically. The hadronisation was done by PYTHIA.

TAUOLA and PHOTOS [111] were used to process τ decays and radiative corrections. A top quark mass of 175 GeV was assumed for all processes. The CTEQ 6L PDF [70] was used for all events, except those generated with MC@NLO, where CTEQ 6M was used. The NLO values were used for $t\bar{t}$, single-top, Z+jets, $W+n$ partons, $Wc\bar{c}+n$ partons and $Wb\bar{b}+n$ partons samples. The NLO values for Z+jets, $W+n$ partons, $Wc\bar{c}+n$ partons and $Wb\bar{b}+n$ partons were obtained by applying a global K factor of 1.24, 1.15, 2.57 and 2.57 to the LO cross-sections, respectively. It should be noted that even these LO cross-sections, due to kinematics cuts imposed to the generators, cannot be directly compared with those of Table 3.1. Initial and final state radiation, and multiple interactions were simulated in agreement with Tevatron data extrapolated to LHC [112]. No pile-up events were added.

Table 4.2 shows the samples used to study some of the systematic uncertainties which will be discussed in Section 4.4. AcerMC was also used to generate $t\bar{t}$ events with at least one of the top quarks decaying semi-leptonically. Samples of $t\bar{t}$ (with at least one lepton) and single top events were produced with pile-up. An average of 4.6 collisions per bunch crossing was taken into account. Different top quark masses (m_t = 160 GeV, 170 GeV and 190 GeV) were also generated for $t\bar{t}$ (with at least one lepton) with MC@NLO. Two $t\bar{t}$ (with at least one lepton) AcerMC samples were generated to study the ISR and FSR. The Pythia parameters were changed in a way that one of the samples had highest top quark mass (the following values were used: `PARJ(81)`=0.07, `PARP(61)`=0.384 and `PARP(62)`=1.0), while the other one had the lowest top quark mass (using the following values: `PARJ(81)`=0.28, `PARP(61)`=0.096 and `PARP(62)`=3.0).

The likelihood-based type of analyses require the use of large samples, but due to the reduced number of generated events, new samples of fast simulation events were also generated. The generation and simulation of these samples was done following the description of Chapter 3, except that newer versions of the generators (TopReX 4.10 and PYTHIA 6.228) and of the PDF set (CTEQ 6L) were used to generate the $t\bar{t}$, single top, W+jets, Z+jets and WZ pairs backgrounds. In order to reduce the number of generated but rejected events due to topological cuts in the analyses, the minimum p_T of the $2 \to 2$ hard process was also raised to 10 GeV. For the signal and $b\bar{b}$ events, the samples described earlier were used. Table 4.3 summarises the information about the generated samples. The samples of both types of simulation were analysed and the shape of the physical distributions were compared, in order to test if the fast simulation samples could be used to construct the pdf, and to compute the discriminant variables to be applied to the full simulation events. Unless otherwise stated, the results reported in this chapter refer to the full simulation samples.

4.2 Full simulation

With the full simulation, the reconstruction of final state particles does not rely on true information. It is based on the simulated signals of each ATLAS sub-detector, done with GEANT4. The signal and background events were passed through the complete GEANT4 sim-

sample ID	process	generator	σ (pb)	no. events	L (fb^{-1})
5510	$t\bar{t} \to bWq\gamma \to b\ell\nu q\gamma, \ell = e, \nu$	TopReX	0.118	9450	80.1
5511	$t\bar{t} \to bWqZ \to b\ell\nu q\ell\ell, \ell = e, \nu$	TopReX	0.198	10000	50.4
5512	$t\bar{t} \to bWqg \to b\ell\nu qg, \ell = e, \nu$	TopReX	1.99	20000	10.1
5200	$t\bar{t} \to bWbW \to bqqb\ell\nu, b\ell\nu b\ell\nu$	MC@NLO	450 (NLO)	548550	0.89
5204	$t\bar{t} \to bWbW \to bqqbqq$	MC@NLO	383 (NLO)	97200	0.19
5500	single top (Wt channel)	AcerMC	29.1 (NLO)	48350	1.66
5501	single top (s-channel)	AcerMC	3.5 (NLO)	48300	14.00
5502	single top (t-channel)	AcerMC	79.9 (NLO)	46950	0.52
5144	$Z \to ee$	PYTHIA	1776 (NLO)	481300	0.27
5145	$Z \to \mu\mu$	PYTHIA	1856 (NLO)	185400	0.10
5146	$Z \to \tau\tau$	PYTHIA	95 (NLO)	176300	1.85
5985	WW	HERWIG	24.5	16250	0.66
5986	ZZ	HERWIG	2.1	29800	14.26
5987	WZ	HERWIG	7.8	30000	3.83
8240	$W \to e\nu$ + 2j	ALPGEN	246 (NLO)	21950	0.09
8241	$W \to e\nu$ + 3j	ALPGEN	143 (NLO)	11250	0.08
8242	$W \to e\nu$ + 4j	ALPGEN	62 (NLO)	6000	0.10
8243	$W \to e\nu$ + 5j	ALPGEN	26 (NLO)	4950	0.19
8244	$W \to \mu\nu$ + 2j	ALPGEN	19 (NLO)	7000	0.37
8245	$W \to \mu\nu$ + 3j	ALPGEN	74 (NLO)	12500	0.17
8246	$W \to \mu\nu$ + 4j	ALPGEN	41 (NLO)	3200	0.08
8247	$W \to \mu\nu$ + 5j	ALPGEN	23 (NLO)	2750	0.12
8248	$W \to \tau\nu$ + 2j	ALPGEN	101 (NLO)	19700	0.20
8249	$W \to \tau\nu$ + 3j	ALPGEN	100 (NLO)	13000	0.13
8250	$W \to \tau\nu$ + 4j	ALPGEN	53 (NLO)	5750	0.11
8251	$W \to \tau\nu$ + 5j	ALPGEN	24 (NLO)	550	0.02
6280	$Wb\bar{b}$ + 0j	ALPGEN	16.1 (NLO)	6250	0.39
6281	$Wb\bar{b}$ + 1j	ALPGEN	17.9 (NLO)	7200	0.40
6282	$Wb\bar{b}$ + 2j	ALPGEN	10.1 (NLO)	4000	0.40
6283	$Wb\bar{b}$ + 3j	ALPGEN	7.1 (NLO)	3000	0.42
6284	$Wc\bar{c}$ + 0j	ALPGEN	17.3 (NLO)	7000	0.41
6285	$Wc\bar{c}$ + 1j	ALPGEN	19.2 (NLO)	3500	0.18
6286	$Wc\bar{c}$ + 2j	ALPGEN	11.2 (NLO)	4500	0.40
6287	$Wc\bar{c}$ + 3j	ALPGEN	6.3 (NLO)	2500	0.40

Table 4.1: The ID, MC generator, cross-section, number of generated events and luminosity is shown for each considered sample (TopView 12–14–03 common ntuples). The cross-sections values include the appropriate branching ratios and parton-jet matching efficiencies when needed. The NLO values were used for $t\bar{t}$, single-top, Z+jets, $W + n$ partons, $Wc\bar{c} + n$ partons and $Wb\bar{b} + n$ partons samples. The NLO values for Z+jets, $W + n$ partons, $Wc\bar{c} + n$ partons and $Wb\bar{b} + n$ partons were obtained by applying a global K factor of 1.24, 1.15, 2.57 and 2.57 to the LO cross-sections, respectively.

ID	process	generator	N_{events}
5205	$t\bar{t} \to bWbW \to bqqb\ell\nu, b\ell\nu b\ell\nu$	AcerMC	113750
5200	$t\bar{t} \to bWbW \to bqqb\ell\nu, b\ell\nu b\ell\nu$ (with pile-up)	MC@NLO	82600
5500	single top (Wt channel with pile-up)	AcerMC	20700
5501	single top (s channel with pile-up)	AcerMC	19250
5502	single top (t-channel with pile-up)	AcerMC	10800
6201	$t\bar{t} \to bWbW \to bqqb\ell\nu, b\ell\nu b\ell\nu$ ($m_t = 170$ GeV)	MC@NLO	98966
6203	$t\bar{t} \to bWbW \to bqqb\ell\nu, b\ell\nu b\ell\nu$ ($m_t = 160$ GeV)	MC@NLO	99750
6204	$t\bar{t} \to bWbW \to bqqb\ell\nu, b\ell\nu b\ell\nu$ ($m_t = 190$ GeV)	MC@NLO	98600
6250	$t\bar{t} \to bWbW \to bqqb\ell\nu, b\ell\nu b\ell\nu$ (ISR/FSR param. $\to \max m_t$)	AcerMC	403555
6251	$t\bar{t} \to bWbW \to bqqb\ell\nu, b\ell\nu b\ell\nu$ (ISR/FSR param. $\to \min m_t$)	AcerMC	431200

Table 4.2: The ID, MC generator and number of available events (TopView 12–14–03 common ntuples) is shown for each sample considered for systematic studies.

process	generator	σ (pb)	no. events	L (fb^{-1})
regular fast simulation samples:				
$t\bar{t} \to bWbW$	TopReX	8.33×10^{2}	8.10×10^{7}	9.72×10^{1}
single top (t-channel)	TopReX	2.47×10^{2}	1.80×10^{7}	7.30×10^{1}
single top (Wt channel)	TopReX	6.42×10^{1}	1.80×10^{7}	2.80×10^{2}
single top (s channel)	TopReX	1.07×10^{1}	1.80×10^{7}	1.69×10^{3}
Z/γ^{*}+jets	PYTHIA	3.25×10^{4}	1.50×10^{8}	4.62×10^{0}
W+jets	PYTHIA	8.38×10^{4}	2.10×10^{8}	2.51×10^{0}
WZ pairs	PYTHIA	3.70×10^{2}	6.50×10^{7}	1.76×10^{2}
$m_t = 170$ GeV fast simulation samples:				
$t\bar{t} \to bWbW$	TopReX	9.40×10^{2}	2.20×10^{7}	2.34×10^{1}
$m_t = 180$ GeV fast simulation samples:				
$t\bar{t} \to bWbW$	TopReX	7.20×10^{2}	2.20×10^{7}	3.06×10^{1}

Table 4.3: The MC generator, cross-section and luminosity is shown for each generated fast simulation sample used in the analyses. All the hadronic and leptonic decays of the W and Z bosons were considered.

ulation of the ATLAS detector using version 12.0.31 of the ATLAS software (ATHENA). The test beam data [113] was used to validate the GEANT4 simulation and an agreement at the level of 1% was achived [114]. The ATLAS layout used in this study, ATLAS–CSC–01–02–00, is based on a perfect detector, with a misaligned layout of LAr and Muons systems, distorted materials in LAr and inner detector, magnetic field with initial displacement included. The signals of each sub-detector were digitized and the whole event was reconstructed with the ATLAS software version 12.0.6, including the trigger simulation. The reconstruction outputs, which come out in the Analysis Object Data format (AOD), were used in the analyses. Muons, electrons, photons and jets were reconstructed using the TopView 12–14–03 [115, 116], which is based on the EventView [117] package. The AOD container and the criteria used for each object reconstruction are shown in Table 4.4. Reconstructed photons which overlap with reconstructed electrons within a cone of $\Delta R = 0.1$ are not considered. Reconstructed jets which overlap within a cone of $\Delta R = 0.2$ with electrons or photons are also not considered. The missing transverse energy was computed as the sum of the energies deposited in the cells associated to reconstructed electrons, photons and jets, as well the energies of cells in topological clusters outside identified objects, muons and the cryostat correction [87]. A disadvantage of using the full simulation is the high computational requirements, in processing time and in storage space. The typical time it takes to completely simulate a event is about 15 minutes.

The reconstruction efficiency of the final state objects was studied with the signal and $t\bar{t} \to bWbW \to bqqb\ell\nu, b\ell\nu b\ell\nu$ samples, by counting the number of times an object was reconstructed within a cone of $\Delta R = 0.4$ around the true particle (generator level). Only isolated true particles where studied (the isolation was defined by requiring $E_T < 6$ GeV in a cone of $\Delta R = 0.2$). When more than one reconstructed object was found, the closest one was chosen. Additionally, in order to avoid radiated particles from jets, reconstructed electrons, muons, photons and taus had to be isolated if the true particle was a quark or a gluon. The reconstruction efficiencies of true electrons, muons, photons, taus and jets as a function of the η and p_T of the true particles are shown from Figure 4.1 to Figure 4.10. The mean efficiencies for the above mentioned particle types, averaged over η, are shown in Table 4.5. These values take into account the pseudo-rapidity distributions of the particles, including the crack effects. Away from the acceptance edges, the efficiency is relatively flat in η. After an increase at low p_T, the efficiency is flat, including the high p_T region of the distributions, where statistics is low. Muons have high reconstruction efficiency, as a result of the dedicated ATLAS muon system. Electrons also have high reconstruction efficiency, but not as good as muons, since they are mistagged as jets in about 16% of the cases. The performance of the ATLAS reconstruction algorithm used for photons is not high. Only about 2/3 of the photons are correctly identified, the other $\sim$ 1/3 being mistagged as hadronic jets. This means that the expected signal efficiency for the $t \to q\gamma$ channel will decrease. Nevertheless, it it reasonable to assume that with high luminosity (10 fb^{-1}) enough information will be available to tune the algorithms in order to increase the performance. Hadronic jets are also reconstructed with high efficiency, but due to the large multiplicity of jets and the large number of expected QCD events, the small mistag efficiencies can originate a large number of fake charged leptons and photons. These reconstruction efficiencies were applied to the fast simulation samples mentioned in the last section, as a function of the η and p_T of the final state particles.

4.3 Event selection

The analyses presented in Chapter 3 were taken as a starting point for the study of the ATLAS sensitivity with the full simulation and without jet b-tagging. The same three FCNC

object	AOD container	criteria
electrons	ElectronCollection	$E_T > 10$ GeV
		only medium egamma electrons (isEM 0x3FF)
		$\|\eta\| < 2.5$
		no isolation cut
muons	StacoMuonCollection	$E_T > 15$ GeV
		isolation cone: 0.2
		absolute isolation cut: 6 GeV
		$\|\eta\| < 2.5$
		no χ^2 cut
		no low p_T muons
		no standalone muons
photons	PhotonCollection	$E_T > 15$ GeV
		only tight egamma photons (isEM 0xFF)
		Tune2 for isEM
		$\|\eta\| < 2.4$
		no isolation cut
taus	TauJetCollection	$E_T > 15$ GeV
		$\|\eta\| < 2.5$
		LogLikelihoodRatio > 6
		fraction of hadronic energy > 0.1
jets	Cone4TowerParticleJets	$E_T > 15$ GeV
		clustering within $\Delta R = 0.4$

Table 4.4: AOD containers and criteria used in TopView 12–14–03 for object reconstruction.

		true				
		e	μ	γ	τ	q/g
reco. as	*	99.6 ± 0.3	94.5 ± 0.3	100 ± 1	65.8 ± 0.4	94.4 ± 0.1
	e	76.8 ± 0.3	0.011 ± 0.002	1.09 ± 0.08	18.4 ± 0.2	1.049 ± 0.008
	μ	0.005 ± 0.002	93.9 ± 0.3	0.010 ± 0.007	19.4 ± 0.2	0.116 ± 0.003
	γ	5.39 ± 0.06	0.002 ± 0.001	66.6 ± 0.8	1.13 ± 0.04	0.176 ± 0.003
	τ	1.47 ± 0.03	0.021 ± 0.003	0.92 ± 0.07	5.77 ± 0.09	0.348 ± 0.004
	jet	15.9 ± 0.1	0.58 ± 0.02	31.2 ± 0.5	21.21 ± 0.2	92.7 ± 0.1

Table 4.5: Reconstruction efficiencies (%) for true muons, electrons, photons, taus and quarks/gluons, with $p_T > 25$ GeV. The asterisk (*) means "anything". See text for details.

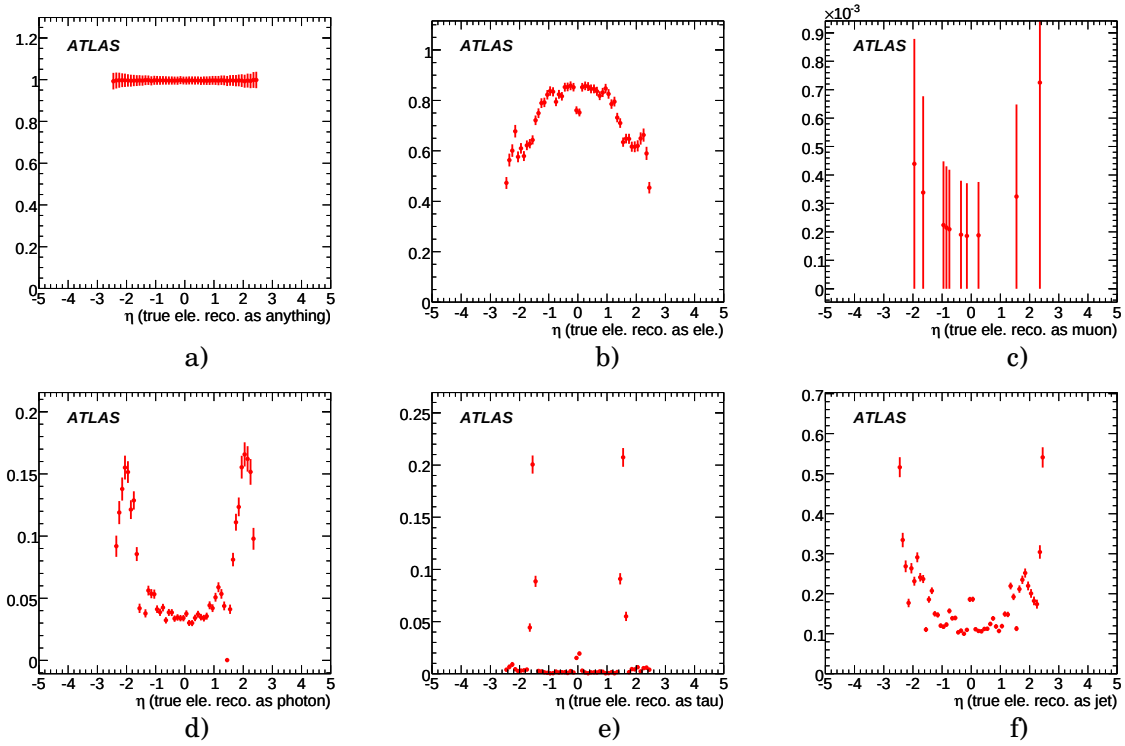

Figure 4.1: Efficiencies as a function of η of true electrons with $p_T > 25$ GeV reconstructed as: a) everything, b) electrons, c) muons, d) photons, e) taus and f) jets. See text for details.

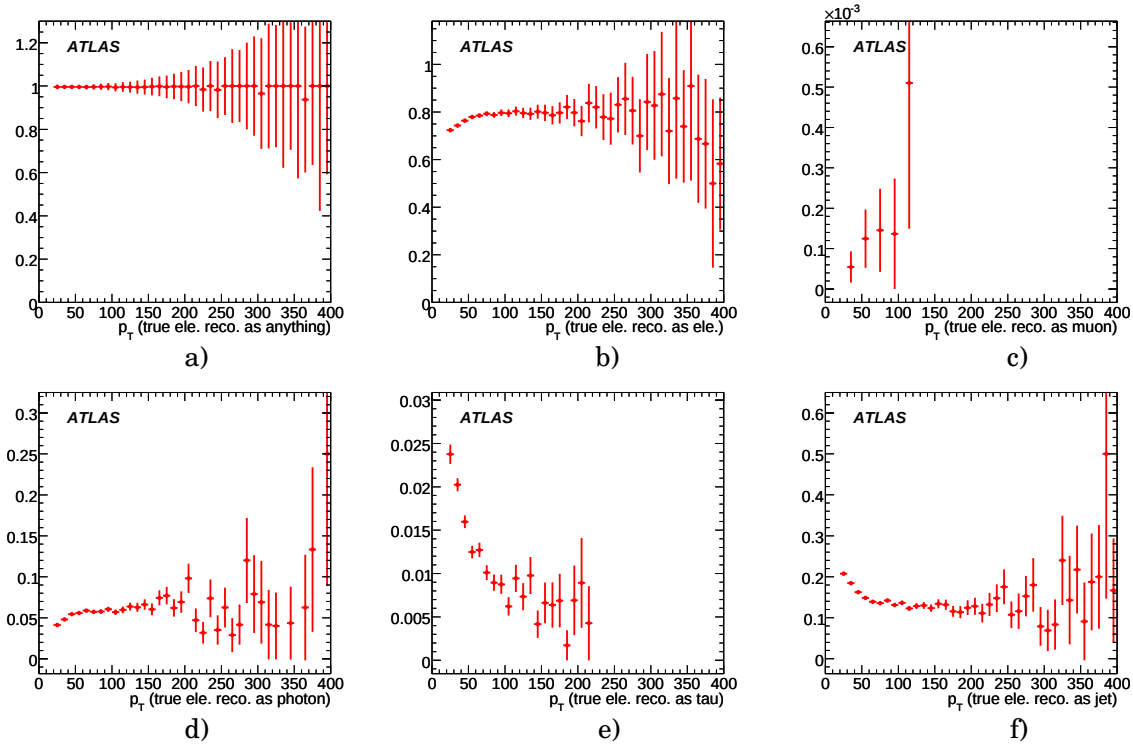

Figure 4.2: Efficiencies as a function of p_T of true electrons with $p_T > 25$ GeV reconstructed as: a) everything, b) electrons, c) muons, d) photons, e) taus and f) jets. See text for details.

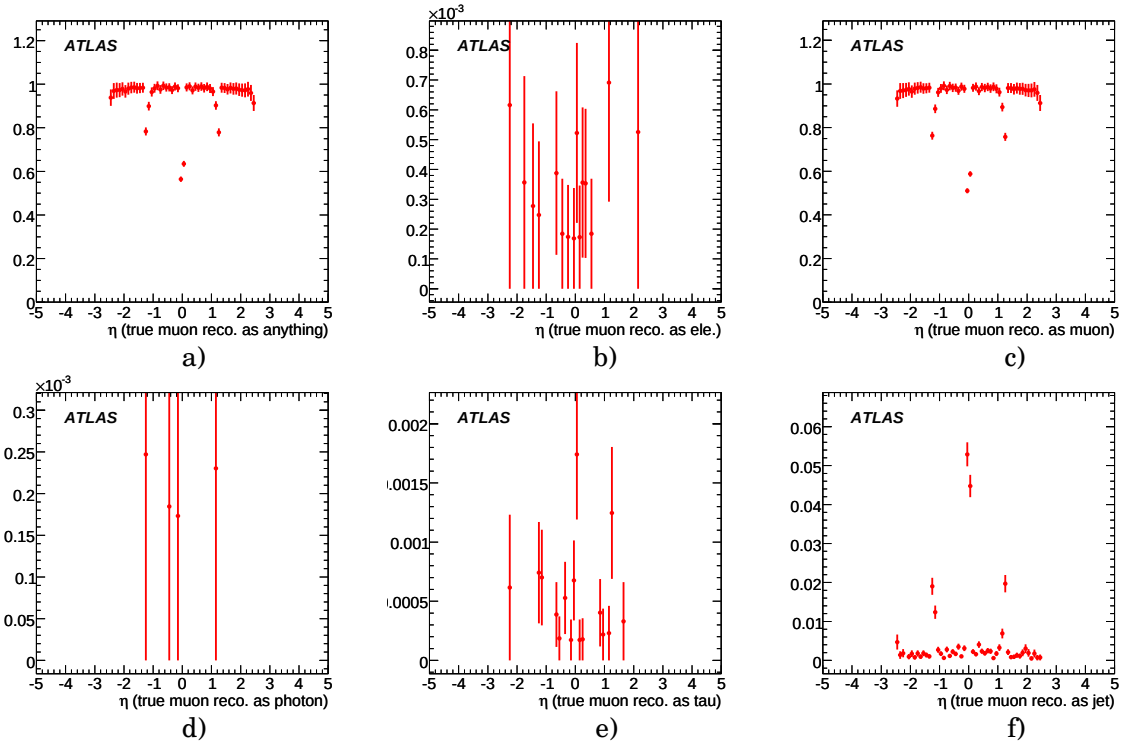

Figure 4.3: Efficiencies as a function of η of true muons with $p_T > 25$ GeV reconstructed as: a) everything, b) electrons, c) muons, d) photons, e) taus and f) jets. See text for details.

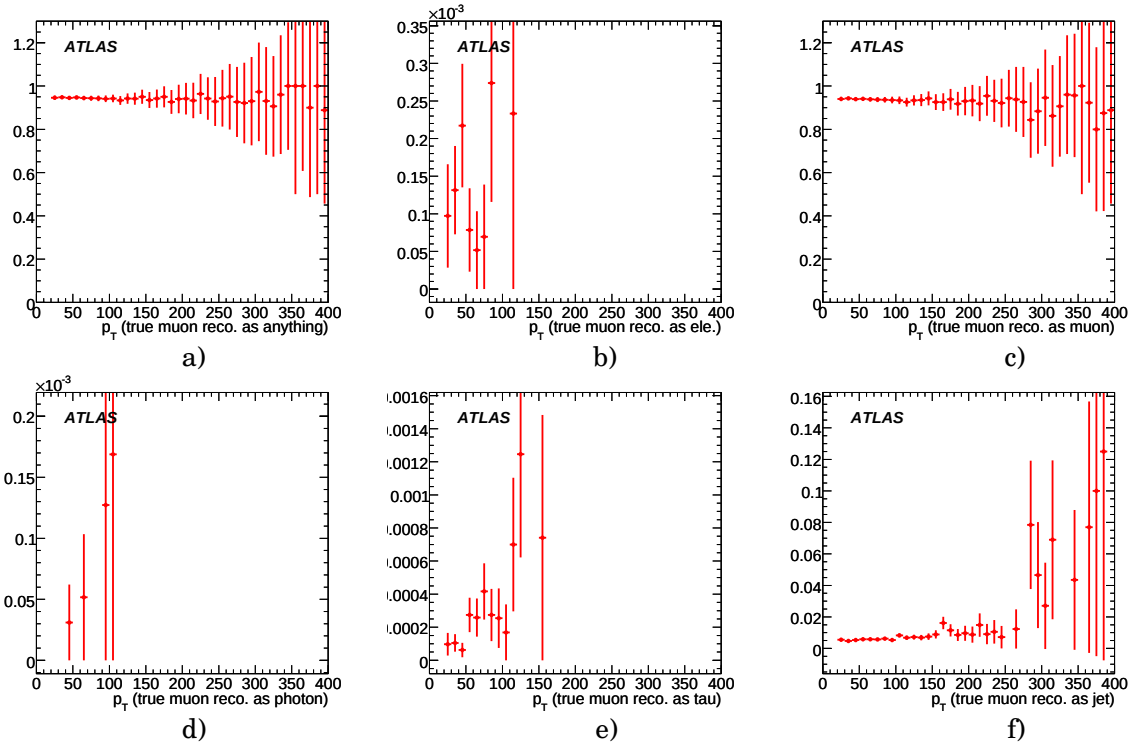

Figure 4.4: Efficiencies as a function of p_T of true muons with $p_T > 25$ GeV reconstructed as: a) everything, b) electrons, c) muons, d) photons, e) taus and f) jets. See text for details.

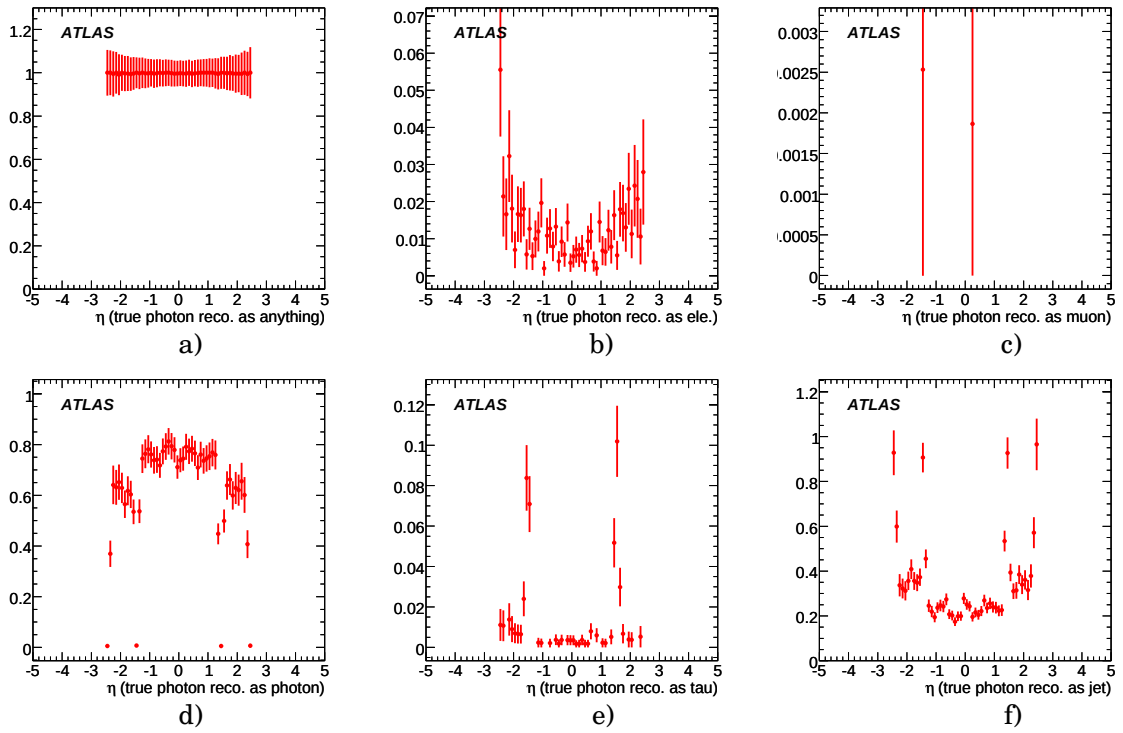

Figure 4.5: Efficiencies as a function of η of true photons with $p_T > 25$ GeV reconstructed as: a) everything, b) electrons, c) muons, d) photons, e) taus and f) jets. See text for details.

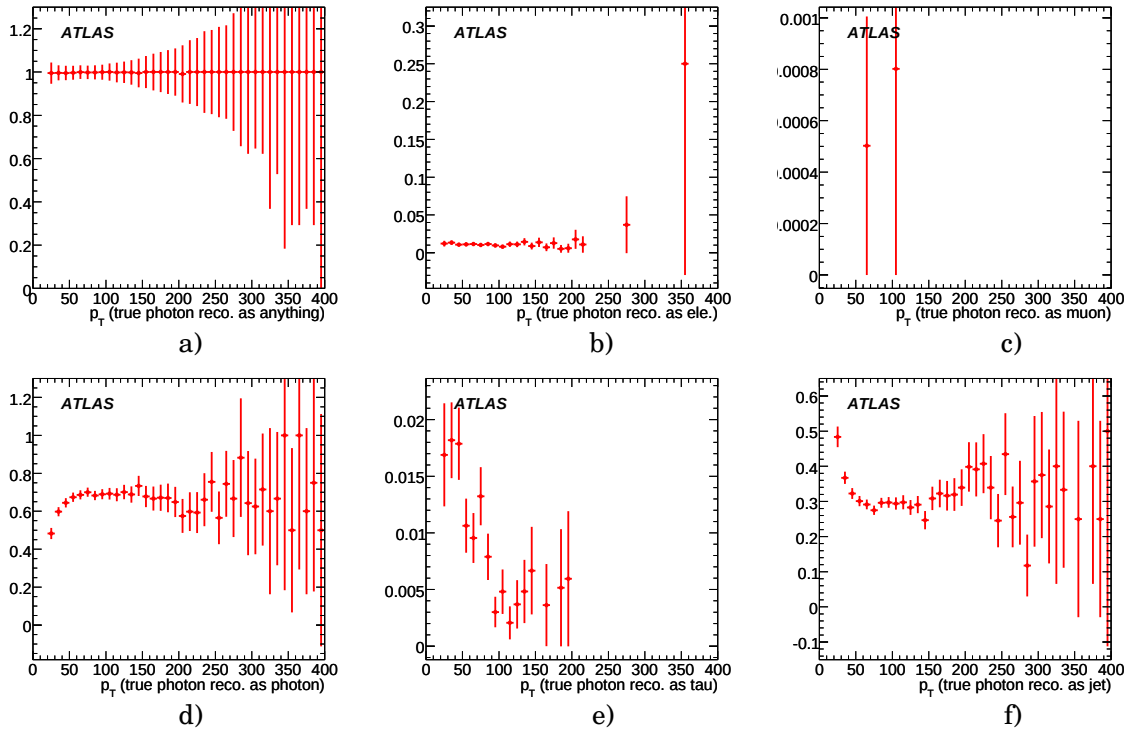

Figure 4.6: Efficiencies as a function of p_T of true photons with $p_T > 25$ GeV reconstructed as: a) everything, b) electrons, c) muons, d) photons, e) taus and f) jets. See text for details.

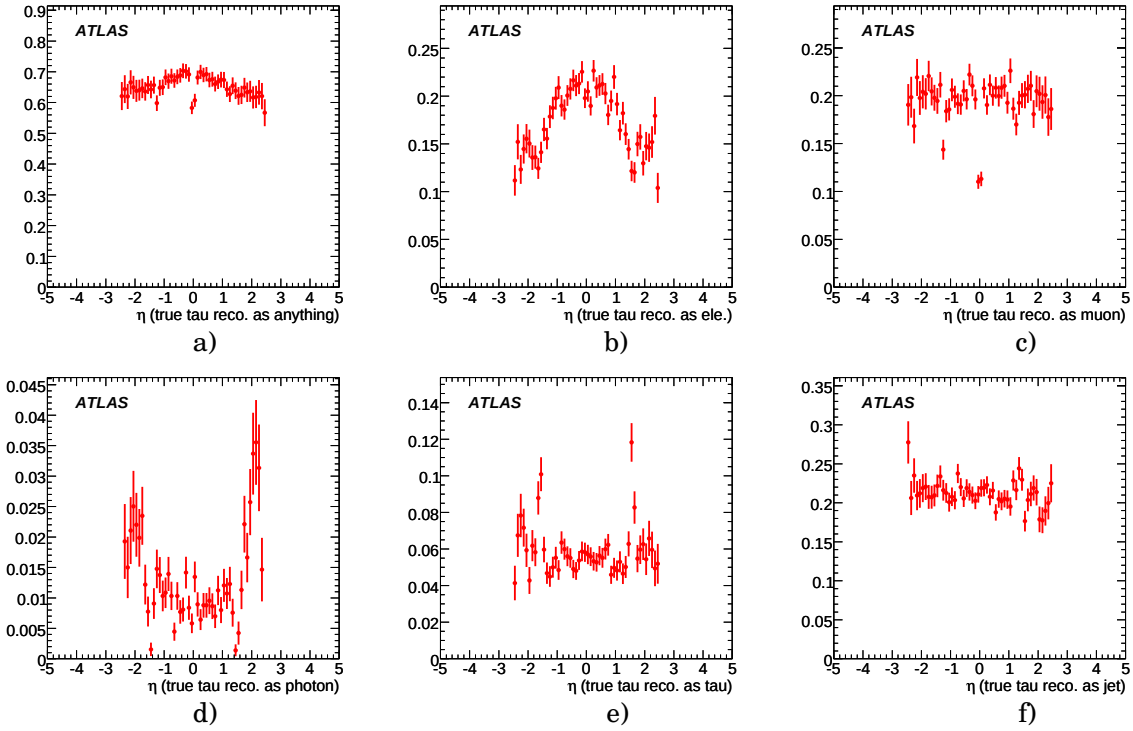

Figure 4.7: Efficiencies as a function of η of true taus with $p_T > 25$ GeV reconstructed as: a) everything, b) electrons, c) muons, d) photons, e) taus and f) jets. See text for details.

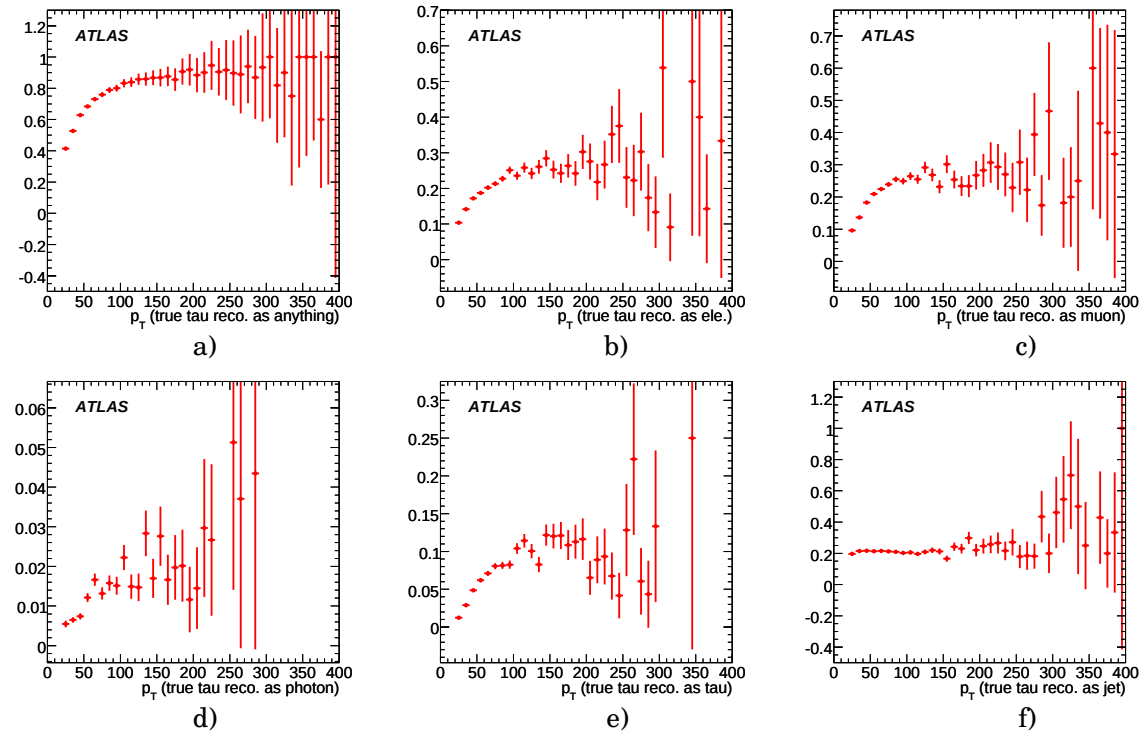

Figure 4.8: Efficiencies as a function of p_T of true taus with $p_T > 25$ GeV reconstructed as: a) everything, b) electrons, c) muons, d) photons, e) taus and f) jets. See text for details.

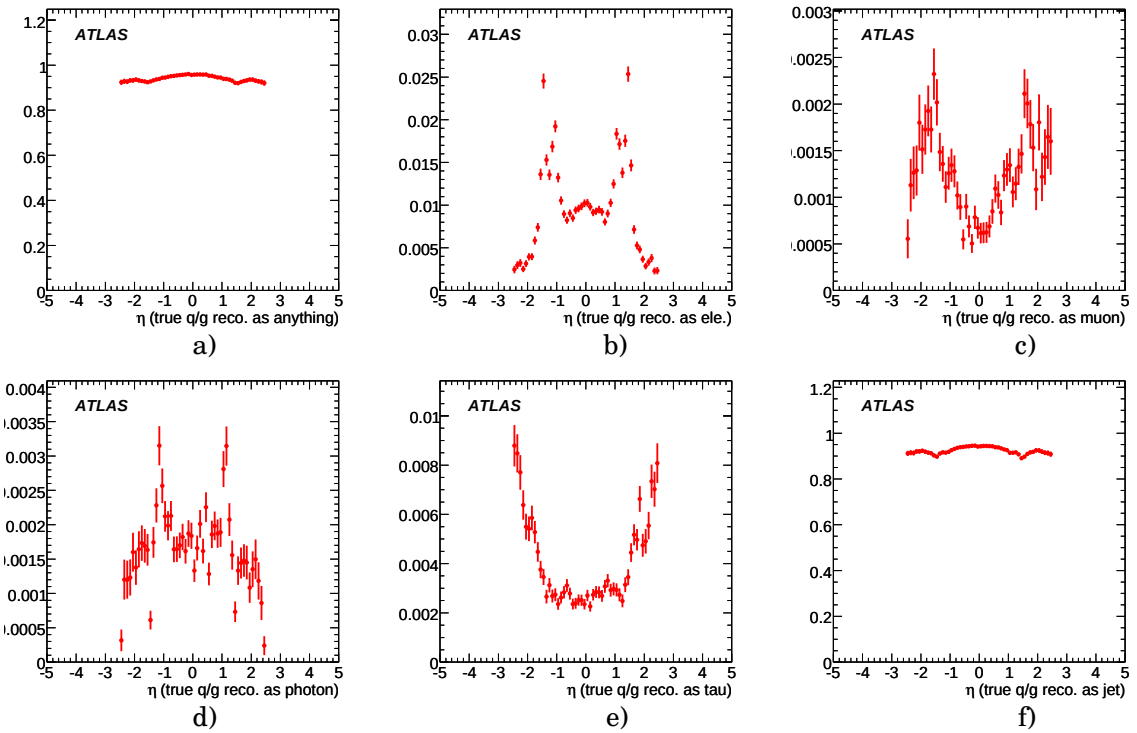

Figure 4.9: Efficiencies as a function of η of true quarks/gluons with $p_T > 25$ GeV reconstructed as: a) everything, b) electrons, c) muons, d) photons, e) taus and f) jets. See text for details.

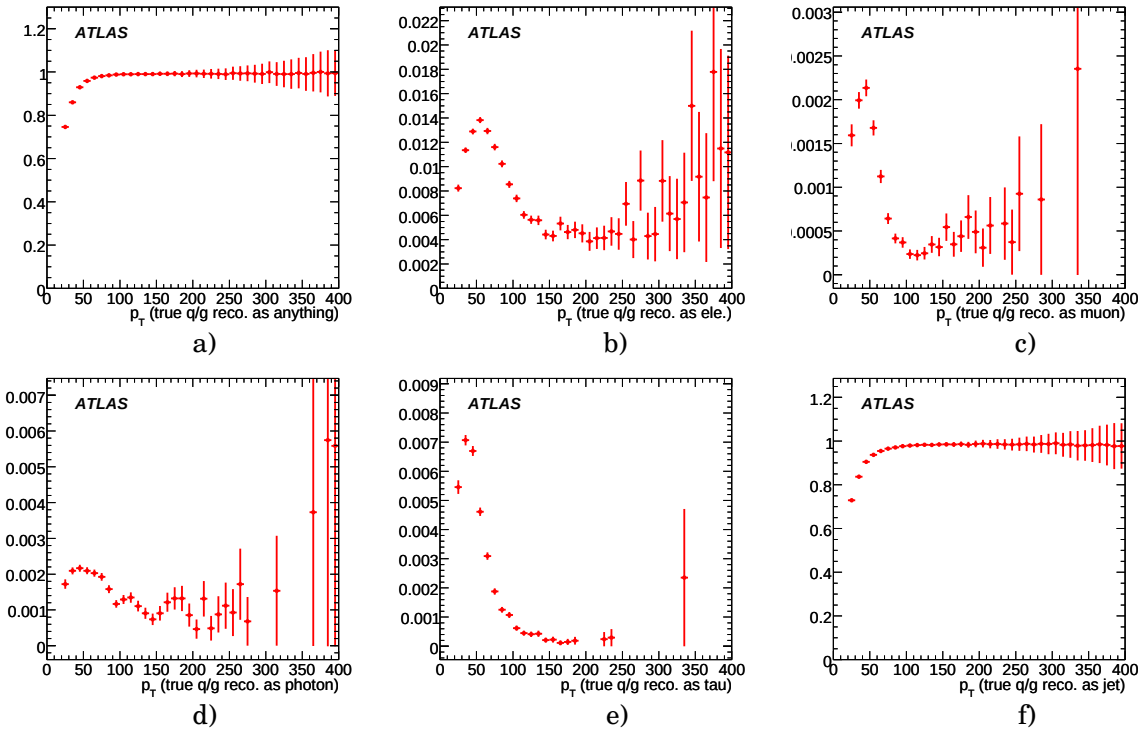

Figure 4.10: Efficiencies as a function of p_T of true quarks/gluons with $p_T > 25$ GeV reconstructed as: a) everything, b) electrons, c) muons, d) photons, e) taus and f) jets. See text for details.

channel	$t \to q\gamma$	$t \to qZ$	$t \to qg$
preselection	$= 1\ell$ ($p_T > 25$ GeV)	$= 3\ell$ ($p_T > 25, 15, 15$ GeV)	$= 1\ell$ ($p_T > 25$ GeV)
	$\geq 2j$ ($p_T > 20$ GeV)	$\geq 2j$ ($p_T > 30, 20$ GeV)	$= 3j$ ($p_T > 40, 20, 20$ GeV)
	$= 1\gamma$ ($p_T > 25$ GeV)	$= 0\gamma$ ($p_T > 15$ GeV)	$= 0\gamma$ ($p_T > 15$ GeV)
	$\not{p}_T > 20$ GeV	$\not{p}_T > 20$ GeV	$\not{p}_T > 20$ GeV
final selection	$p_{T_\gamma} > 75$ GeV	2 ℓ same flavour, oppos. charge	$E_{\text{vis}} > 300$ GeV
			$p_{T_g} > 75$ GeV
			$m_{qg} > 125$ GeV
			$m_{qg} < 200$ GeV
trigger	e25i, mu20i or g60	e25i or mu20i	e25i or mu20i

Table 4.6: Selection cuts applied in the analyses with full simulation. For the $t \to qg$ channels, E_{vis}, p_{T_g} and m_{qg} represent the total visible energy, the transverse momentum of the jet associated with the gluon and the reconstructed mass of the top quark with FCNC decay, respectively (see text for details).

channels were considered: $t\bar{t} \to bWq\gamma$, $t\bar{t} \to bWqZ$ and $t\bar{t} \to bWqg$ (which will continue to be labeled $t \to q\gamma$, $t \to qZ$ and $t \to qg$, respectively). For this last channel only the "3 jets" sample was studied, since this is the dominant channel for the gluon analysis, as can be seen in Table 3.11. Only the leptonic decays of both W and Z to e and μ were taken into account. Only isolated muons, electrons and photons, with $\Delta R > 0.4$ in relation to other reconstructed objects, were considered. Table 4.6 summarises the cuts performed in the analyses. It should be noted that for the different channels the selection is still orthogonal. Only the differences in respect to the analyses presented in Section 3.3 are described below. The trigger selection was applied only after all the other selection cuts in order to study its effect in the number of selected events. In order to handle simultaneously different simulated data formats, LipCbrAnalysis, a new C++ analysis program using the ROOT [118] framework was developed.

Preselection

In order to simplify the analyses, only topological cuts were done in the preselection. The other cuts were moved to the final selection.

$t \to q\gamma$ channel:

For the preselection of the $t \to q\gamma$ channel, the difference is that the events had to have exactly one photon and one lepton. This way, the preselection becomes simpler and reduces the contribution from events with two photons.

$t \to qZ$ channel:

For the $t \to qZ$ channel, the p_T cut for the non-leading leptons was raised to 15 GeV, since that is the minimum value used to reconstruct isolated muons. Events with more than 3 isolated leptons were not accepted, since the corresponding signal efficiency is very small. The leading jet was required to have $p_T > 30$ GeV already at preselection (this criteria was applied

before in the final selection). In order to reduce the background events with photons (from ISR/FSR or mistag), no reconstructed photons were allowed.

$t \to qg$ channel:

In order to define only the event topology in the preselection, the $E_{\text{vis}} > 300$ GeV criterum was moved to the final selection and neither the b-tagging multiplicity cut nor the p_{z_ν} requirement were applied.

Number of selected events and relevant variables:

The expected number of background events, normalised to 1 fb^{-1}, and signal efficiencies after preselection cuts are shown in Table 4.7. In order to study the effect of the different reconstruction efficiencies, three sub-samples were defined according to the flavour of the isolated charged leptons: only electrons, only muons and no separation. For all the FCNC channels, the sub-sample with muons has higher signal efficiencies and lower number of expected background than the ones for the sub-sample with electrons, as expected. The effect of mistag in the background contributions is also visible as an increase of the number of expected events, when compared to the numbers given in Table 3.6 (after applying a normalisation factor due to the different luminosities used). As a test, the same events of the full simulation samples, but with the fast simulation and without any correction for the object identification criteria efficiencies, were used. Repeating the analyses, 1621±99, 55±55 and 57716±624 background events are expected for the $t \to q\gamma$, $t \to qZ$ and $t \to qg$ channels, respectively, which indicates that the differences come from the reconstruction and mistag efficiencies. The distribution of relevant variables after this selection level are shown from Figure 4.11 to Figure 4.21. The distributions obtained with the fast simulation are also shown. As can be seen from the figures, there is a fair agreement between the fast and the full simulated distributions, both for signal and background. There are also some discrepancies in the low p_T region (p_T<50 GeV) in jet momenta distributions, which arise from the different generators used and slightly different generated phase space.

	Z+jets	W+jets	WZ pairs	$t\bar{t}$	single top	total background	signal efficiency %
				after preselection			
$t\bar{t} \to bWq\gamma$:							
e	926 ± 59	311 ± 71	27 ± 5	583 ± 25	22 ± 4	1869 ± 96	6.1 ± 0.2
μ	129 ± 35	367 ± 69	12 ± 4	561 ± 21	30 ± 6	1100 ± 80	7.3 ± 0.2
ℓ	1055 ± 68	678 ± 84	40 ± 6	1145 ± 32	52 ± 7	2969 ± 113	13.4 ± 0.3
$t\bar{t} \to bWqZ$:							
$3e$	12 ± 12	0 ± 53	2 ± 2	17 ± 5	0 ± 2	30 ± 55	1.4 ± 0.1
3μ	0 ± 11	0 ± 53	6 ± 2	7 ± 5	0 ± 2	13 ± 55	2.7 ± 0.1
3ℓ	35 ± 16	0 ± 53	16 ± 3	152 ± 12	0 ± 2	204 ± 57	8.1 ± 0.2
$t\bar{t} \to bWqg$:							
e	1524 ± 73	28642 ± 569	597 ± 27	6558 ± 75	1978 ± 48	39299 ± 581	2.2 ± 0.1
μ	2626 ± 158	17248 ± 327	636 ± 27	7521 ± 80	2634 ± 56	30665 ± 377	2.8 ± 0.1
ℓ	4150 ± 173	45890 ± 655	1233 ± 38	14079 ± 109	4612 ± 74	69964 ± 691	5.0 ± 0.1

Table 4.7: The expected number of background events and signal efficiencies after the preselection level of the analyses for each FCNC channel. The expected background numbers are normalised to $L = 1$ fb^{-1}.

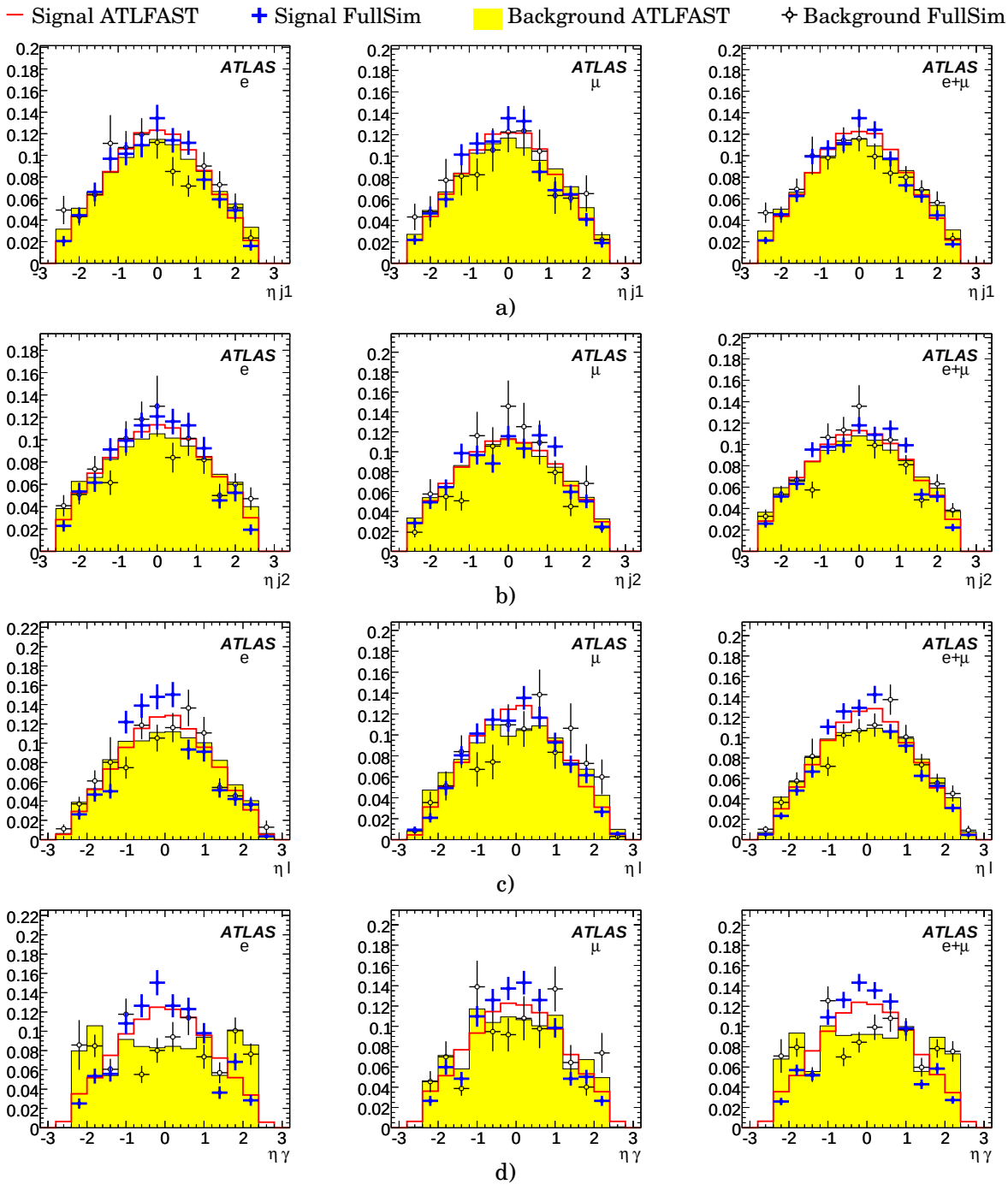

Figure 4.11: Normalised distributions, for the expected background and signal after the pre-selection of the $t \to q\gamma$ channel, of the pseudo-rapidities of the a) leading jet, b) second jet, c) lepton and d) photon, when the isolated lepton is identified as an electron (left), a muon (centre) and electron or muon (left).

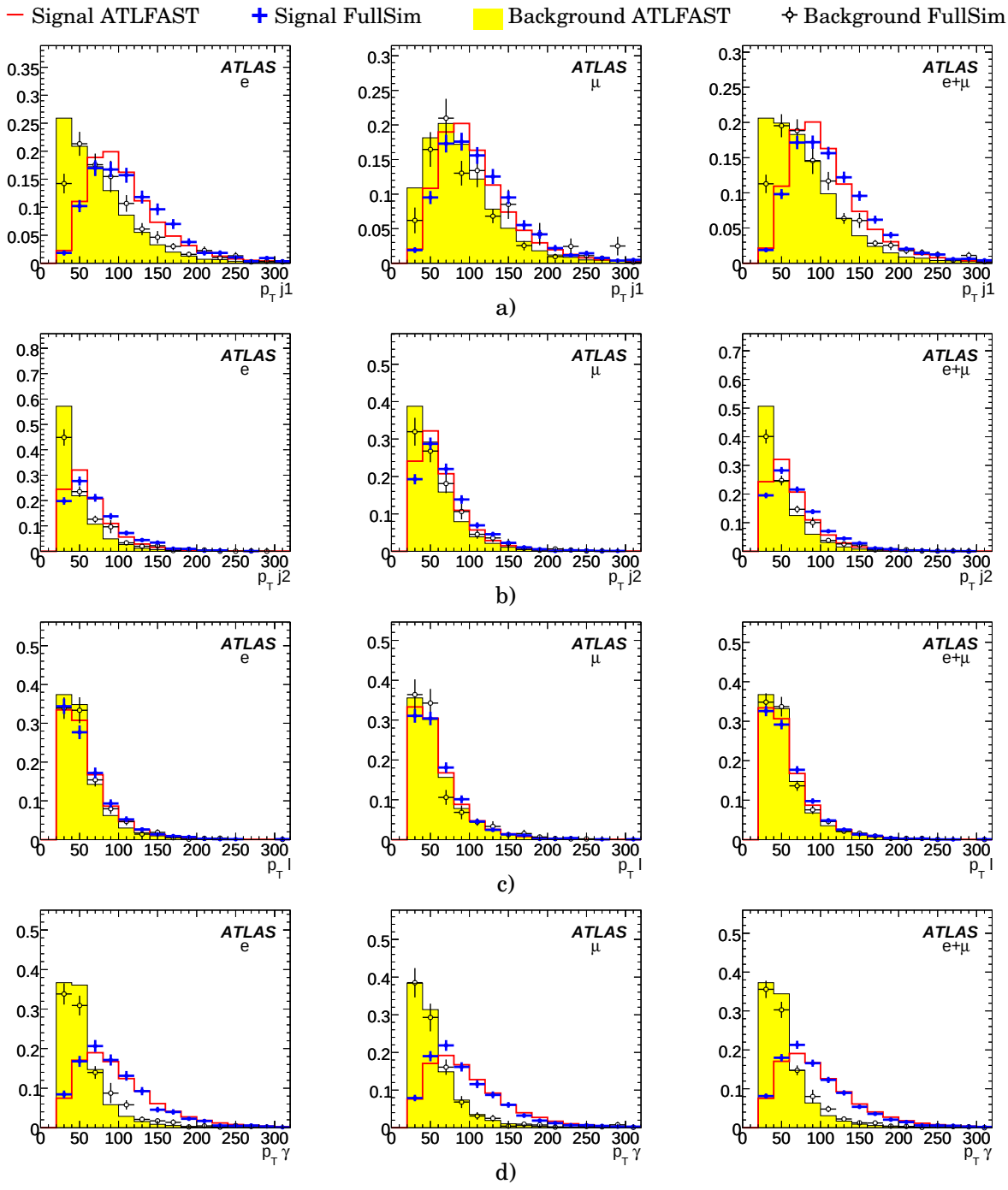

Figure 4.12: Normalised distributions, for the expected background and signal after the preselection of the $t \to q\gamma$ channel, of the transverse momenta of the a) leading jet, b) second jet, c) lepton and d) photon, when the isolated lepton is identified as an electron (left), a muon (centre) and electron or muon (left).

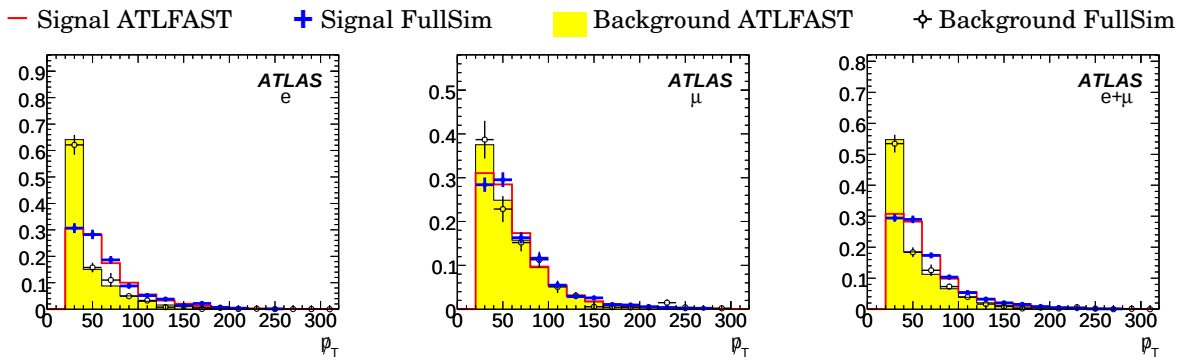

Figure 4.13: Normalised distributions, for the expected background and signal after the preselection of the $t \to q\gamma$ channel, of the missing transverse momentum, when the isolated lepton is identified as an electron (left), a muon (centre) and electron or muon (left).

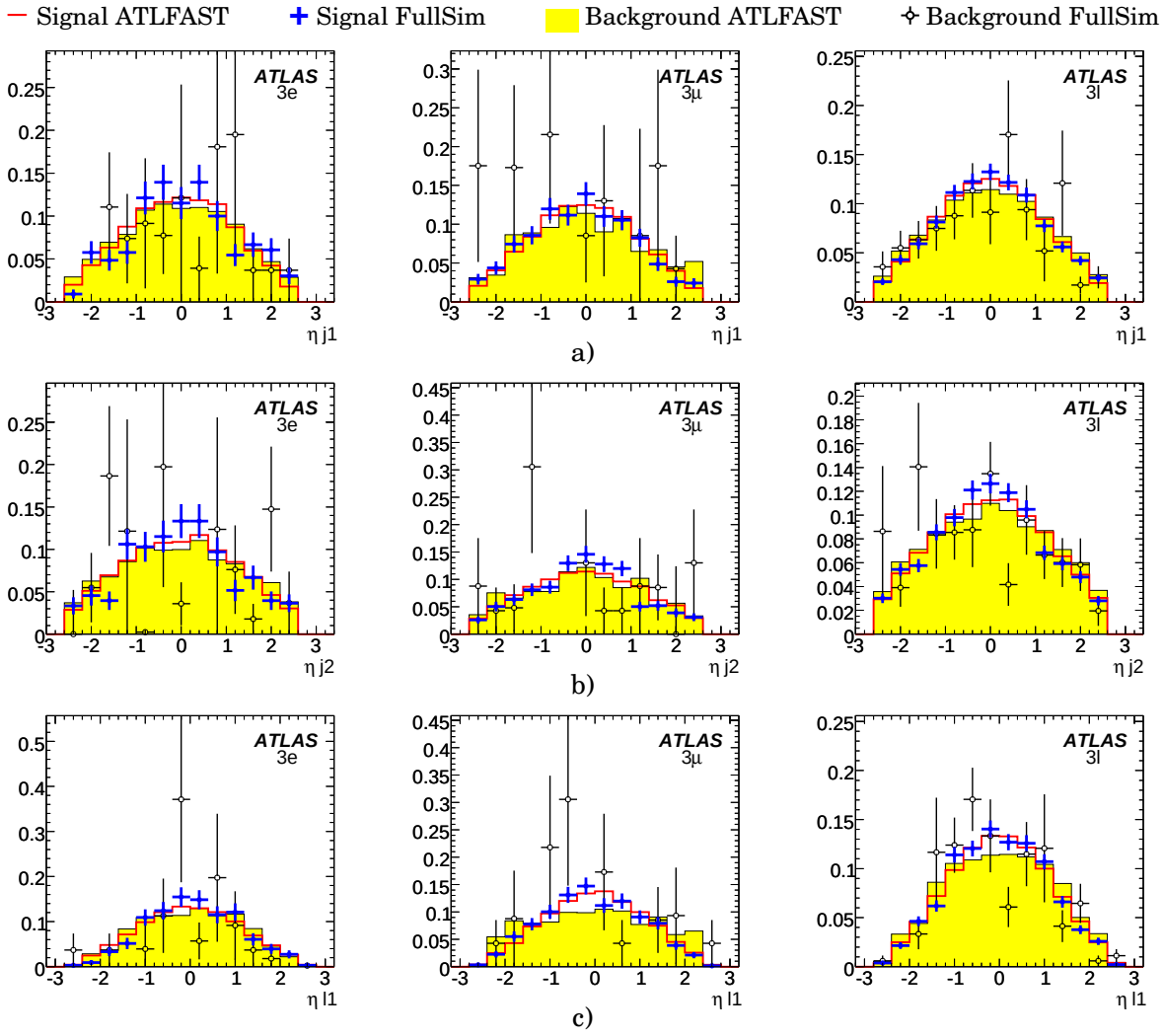

Figure 4.14: Normalised distributions, for the expected background and signal after the preselection of the $t \to qZ$ channel, of the pseudo-rapidities of the a) leading jet, b) second jet and c) leading lepton, when the three isolated leptons are identified as electrons (left), muons (centre) and electrons or muons (left).

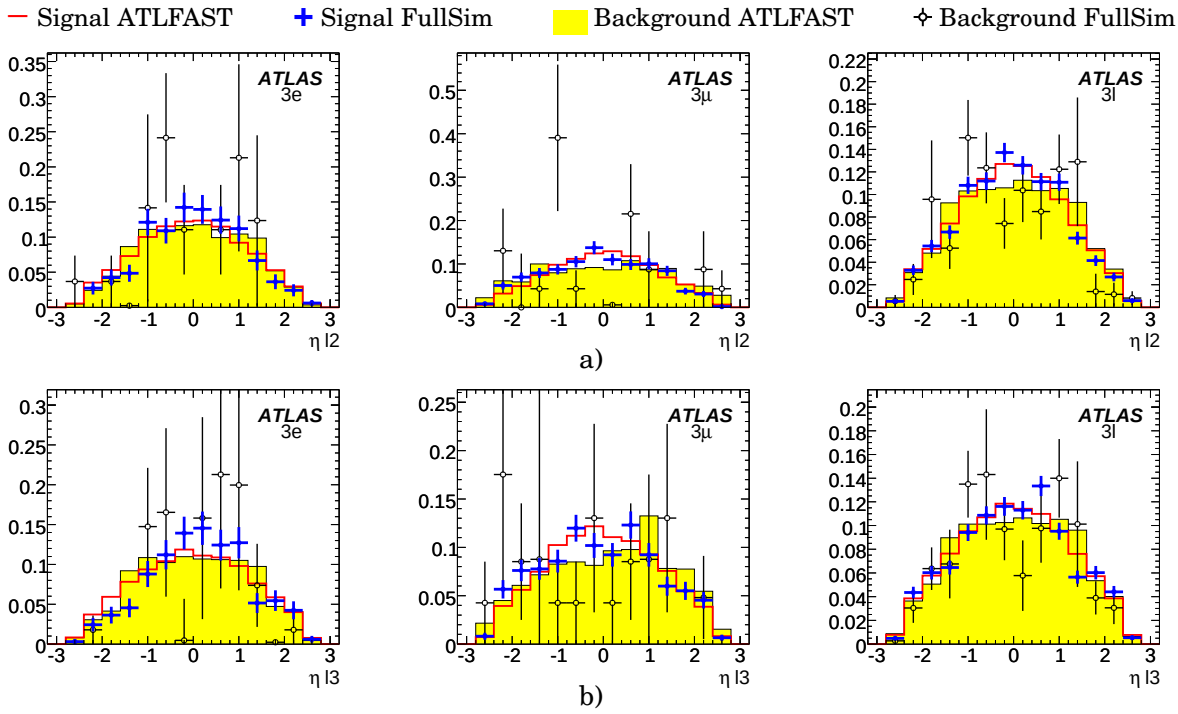

Figure 4.15: Normalised distributions, for the expected background and signal after the preselection of the $t \to qZ$ channel, of the pseudo-rapidities of the a) second lepton and b) third lepton, when the three isolated leptons are identified as electrons (left), muons (centre) and electrons or muons (left).

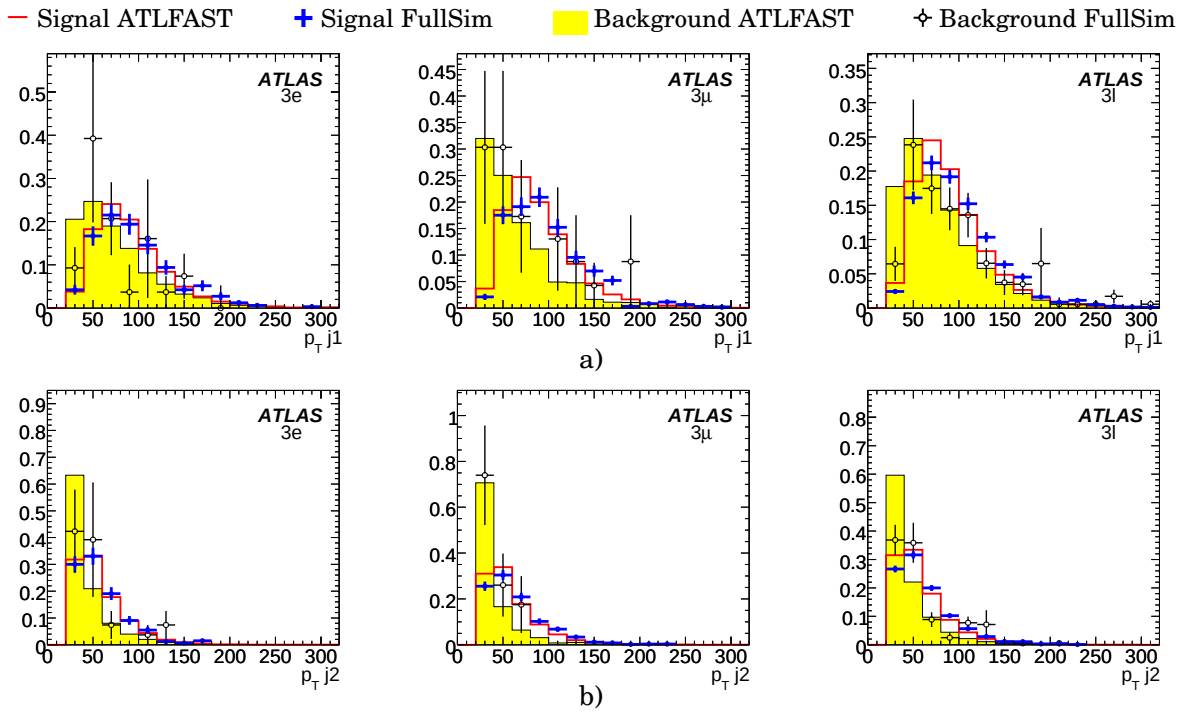

Figure 4.16: Normalised distributions, for the expected background and signal after the preselection of the $t \to qZ$ channel, of the transverse momenta of the a) leading jet and b) second jet, when the three isolated leptons are identified as electrons (left), muons (centre) and electrons or muons (left).

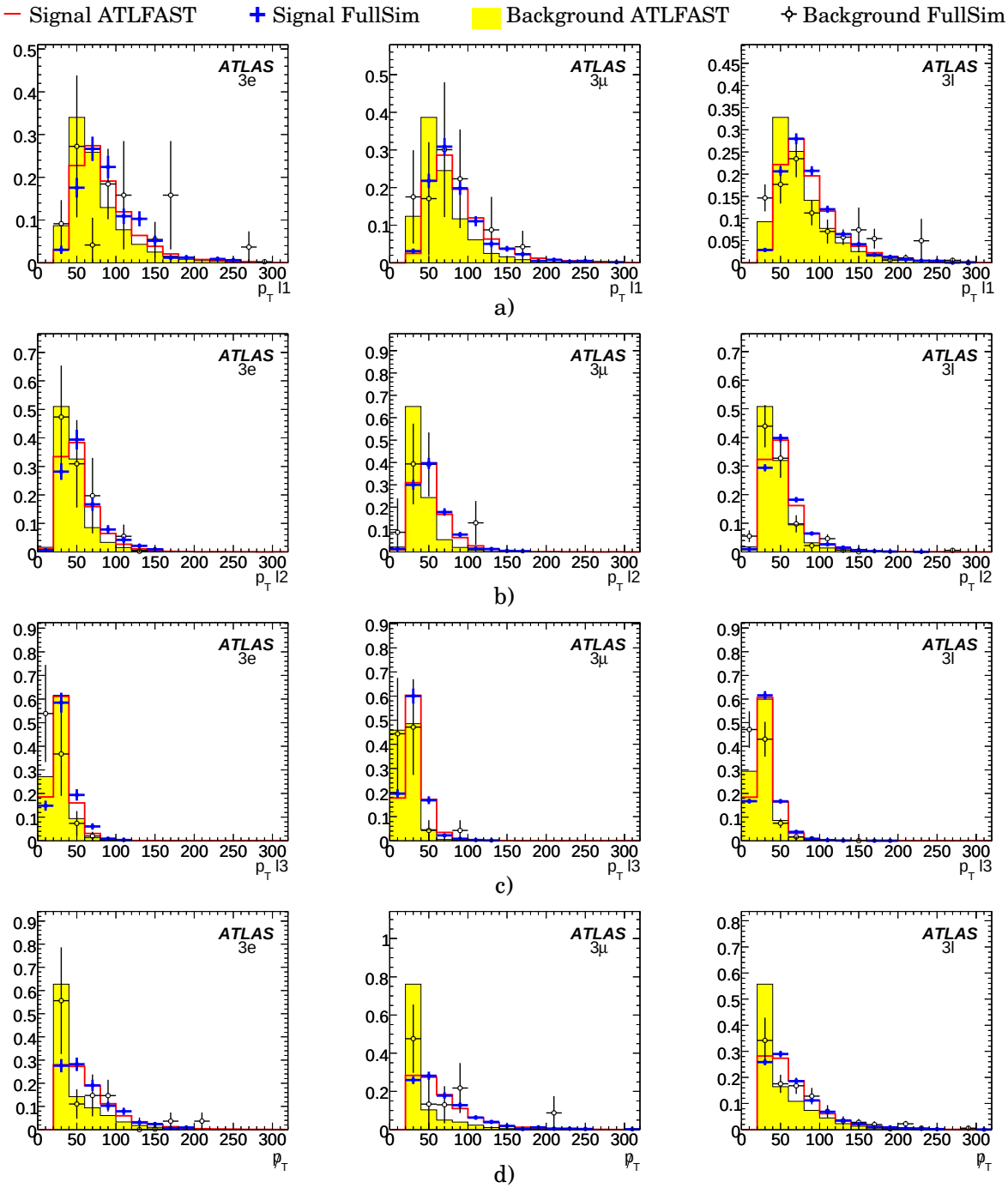

Figure 4.17: Normalised distributions, for the expected background and signal after the preselection of the $t \to qZ$ channel, of the transverse momenta of the a) leading lepton, b) second lepton and c) third lepton and d) the missing transverse momentum, when the three isolated leptons are identified as electrons (left), muons (centre) and electrons or muons (left).

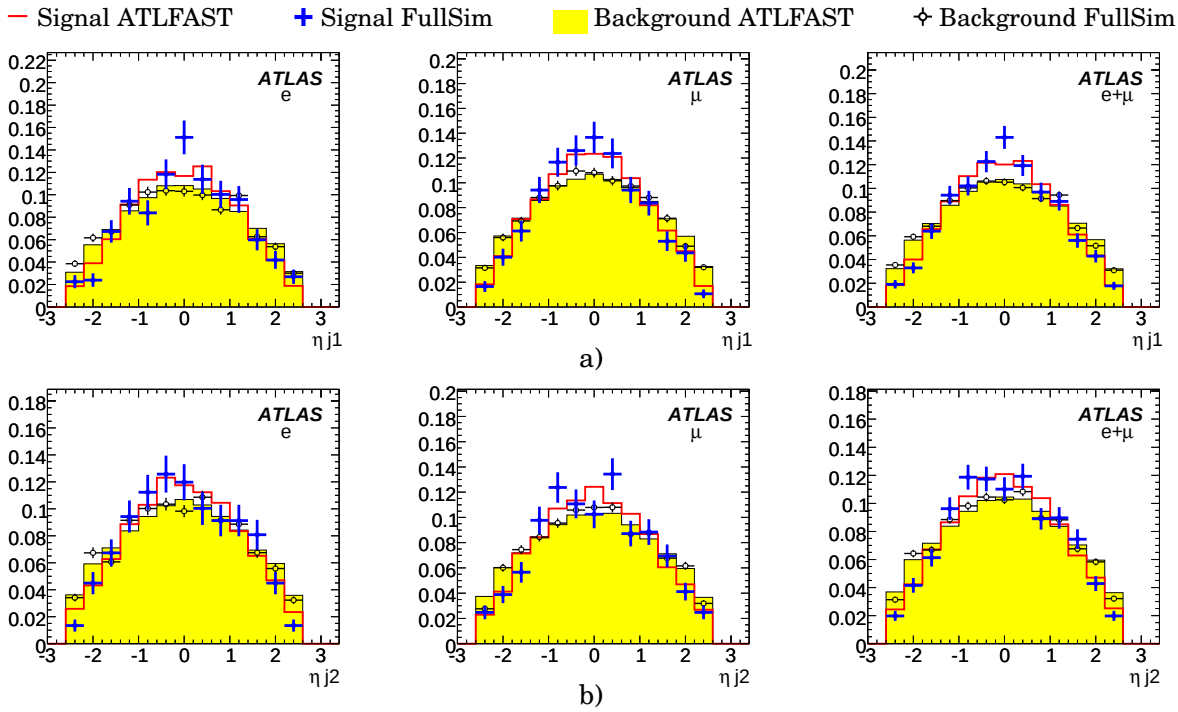

Figure 4.18: Normalised distributions, for the expected background and signal after the preselection of the $t \to qg$ channel, of the pseudo-rapidities of the a) leading jet and b) second jet, when the isolated lepton is identified as an electron (left), a muon (centre) and electron or muon (left).

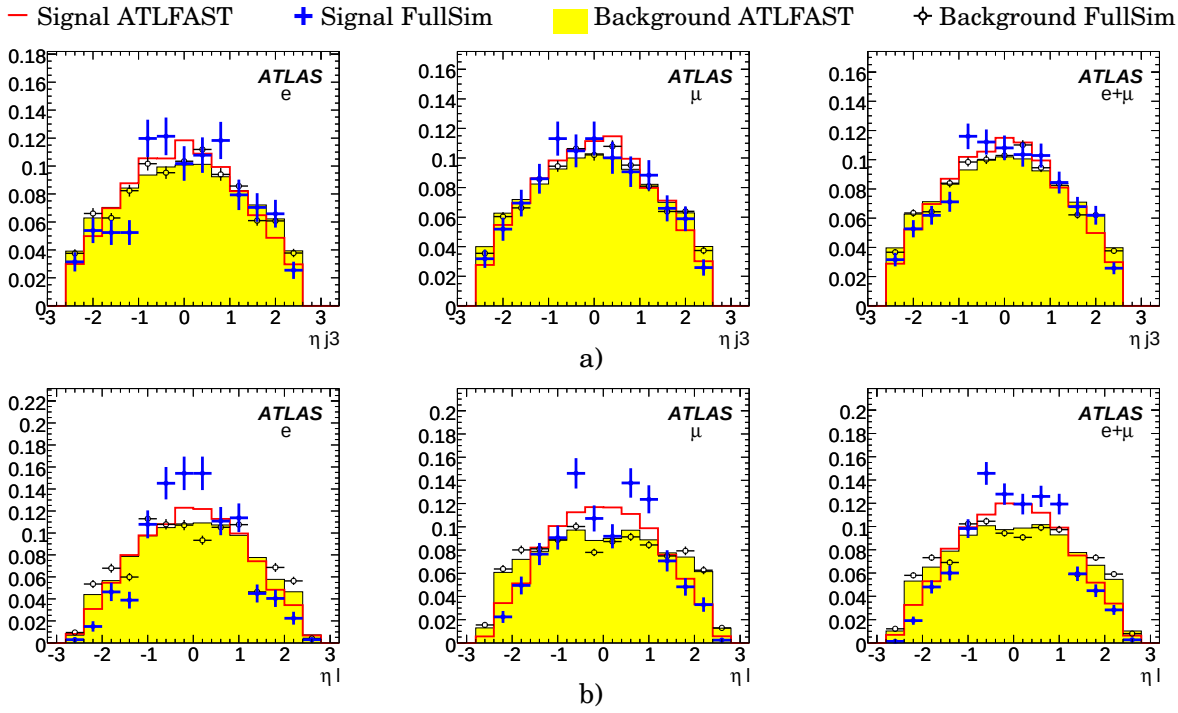

Figure 4.19: Normalised distributions, for the expected background and signal after the preselection of the $t \to qg$ channel, of the pseudo-rapidities of the a) third jet and b) lepton, when the isolated lepton is identified as an electron (left), a muon (centre) and electron or muon (left).

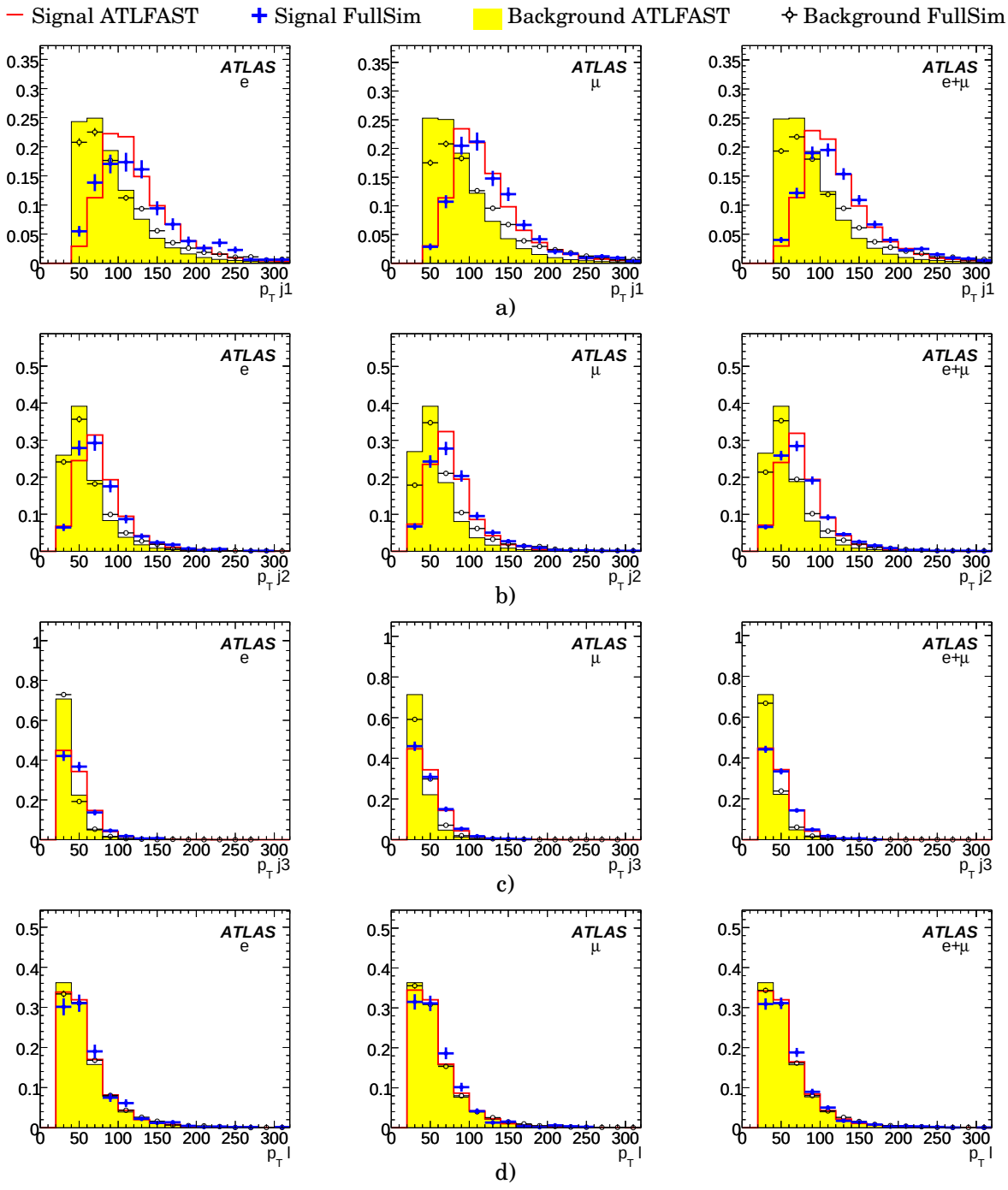

Figure 4.20: Normalised distributions, for the expected background and signal after the preselection of the $t \to qg$ channel, of the transverse momenta of the a) leading jet, b) second jet, c) third jet and d) lepton, when the isolated lepton is identified as an electron (left), a muon (centre) and electron or muon (left).

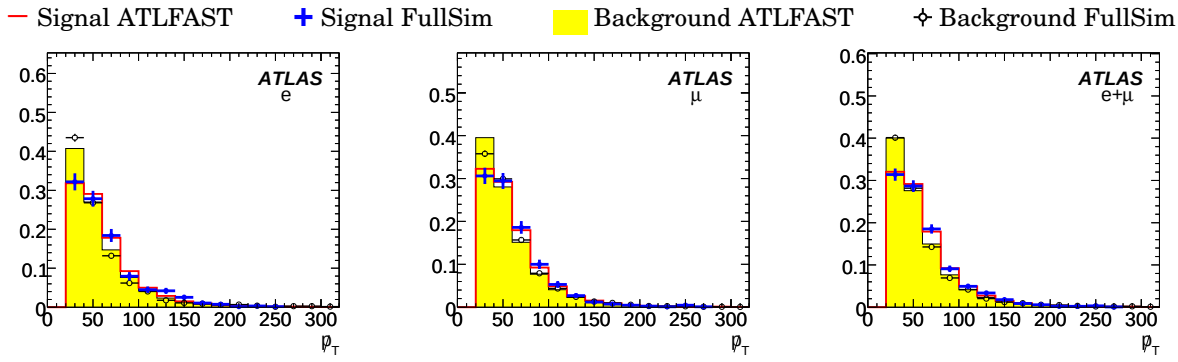

Figure 4.21: Normalised distributions, for the expected background and signal after the preselection of the $t \to qg$ channel, of the missing transverse momenta, when the isolated lepton is identified as an electron (left), a muon (centre) and electron or muon (left).

Kinematics reconstruction

In the analyses described in Chapter 3, the neutrino longitudinal momentum was reconstructed by solving a quadratic equation and it was then associated to the isolated lepton and to the b-tagged jet in order to reconstruct the top quark with FCNC decay. A new method was developed to perform the kinematics reconstruction without using jet tagging algorithms.

Again, the missing transverse energy is considered to be the neutrino transverse momentum. The longitudinal component can be determined by finding the p_Z^ν value and the jet combination (and the lepton combination in the case of the qZ topology) which gives the minimum value of the expression:

$$\chi^2 = \frac{\left(m_t^{\mathrm{FCNC}} - m_t\right)^2}{\sigma_t^2} + \frac{\left(m_{\ell_a \nu j} - m_t\right)^2}{\sigma_t^2} + \frac{\left(m_{\ell_a \nu} - m_W\right)^2}{\sigma_W^2} + \frac{\left(m_{\ell_b \ell_c} - m_Z\right)^2}{\sigma_Z^2}, \tag{4.1}$$

where m_t^{FCNC}, $m_{\ell_a \nu j}$, $m_{\ell_a \nu}$ and $m_{\ell_b \ell_c}$ are, for each jet and lepton combination, the reconstructed mass of the top quark decaying via FCNC, the top quark decaying through SM, the W boson from the top quark with SM decay and the Z boson from the top quark FCNC decay, respectively. The last term of expression 4.1 was only used in the $t \to qZ$ channel. The following values are used for the constraints: $m_t = 175$ GeV, $m_W = 80.42$ GeV, $m_Z = 91.19$ GeV, $\sigma_t = 14$ GeV, $\sigma_W = 10$ GeV and $\sigma_Z = 3$ GeV. No b-tag information was used to reconstruct the event kinematics and no event was discarded. The jet chosen to reconstruct the top quark with SM decay is labeled b quark. For the $t \to q\gamma$ and the $t \to qZ$ channels, the other jet, which was used to reconstruct the top quark with FCNC decay, is denoted by q quark. For the $t \to qg$ channel, it is assumed that the jet created by the gluon is the most energetic from the two which reconstruct the top quark with FCNC decay and the other is produced by the light quark.

Reconstructed masses:

The obtained χ^2 distributions, for the expected background and signal events, are presented in Figure 4.22, while the obtained distributions of the reconstructed masses of the top quark decaying via FCNC (m_t^{FCNC}), the top quark decaying through SM (m_t^{SM}), the W boson (m_W) and the Z boson (m_Z), for the full simulation of signal events, are shown in Figure 4.23. As expected, the χ^2 distributions have a peak at small values for signal events and have wider

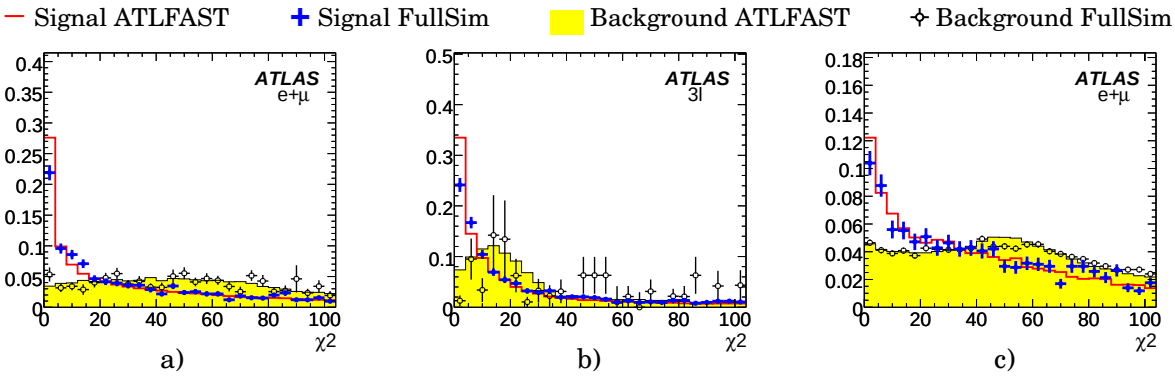

Figure 4.22: Normalised distributions of the minimum χ^2 value of the kinematics reconstruction found for each event, for the expected background and signal after the preselection of the a) $t \to q\gamma$, b) $t \to qZ$ and c) $t \to qg$ channels.

shapes for the background events. In order to study the resolution of the kinematics reconstruction, Gaussian functions were fitted to these invariant mass distributions. The obtained values for the Gaussian functions parameters (mass and width of the resonance) are listed in Table 4.8. It should be stressed that the σ parameters of expression 4.1 do not represent the widths of resonances, and thus, should not be compared with the ones of Table 4.8. In fact, one can rescale the σ parameters (by some arbitrary value, but equal for all σ) and obtain the same result. Figure 4.23 and the Table 4.8 (full simulation signal) cannot be compared directly with Figure 3.5 and Table 3.7, respectively, because they were obtained using different detector simulations and different kinematics reconstruction criteria. For this reason, this study was also done with the fast simulation of the signal samples. The results are summarised in Table 4.8. It can be seen that the full simulation gives broader mass distributions, although the central values are similar (the mean difference is 0.4 GeV). Comparing the fast simulation signal samples results, one finds similar central values. The widths obtained with the χ^2 method can be similar to the ones obtained in Chapter 3 by adjusting the σ parameters of expression 4.1.

Reconstruction efficiencies:

The obtained reconstruction efficiencies are shown in Tables 4.9 and 4.10. The same criteria used for computing Table 3.8 were applied. Comparing the two reconstruction methods for the fast simulation samples, it can be seen that the reconstruction efficiencies of the b quark decrease from about 90% to about 75%. Nevertheless, this is a high value since no b-tag information was used. The lower b-quark efficiency is also reflected in the lower reconstruction efficiency of the top quark with FCNC decay of the $t \to qg$ channel (since this top quark is reconstructed from the other two jets). For the $t \to qZ$ channel, the χ^2 method is more efficient to reconstruct the Z boson and the top quark with FCNC decay.

Final selection

In order to reduce the background contribution to the analyses, further selection cuts were applied to the three channels under study. Again, only the differences with respect to section 3.3 will be described.

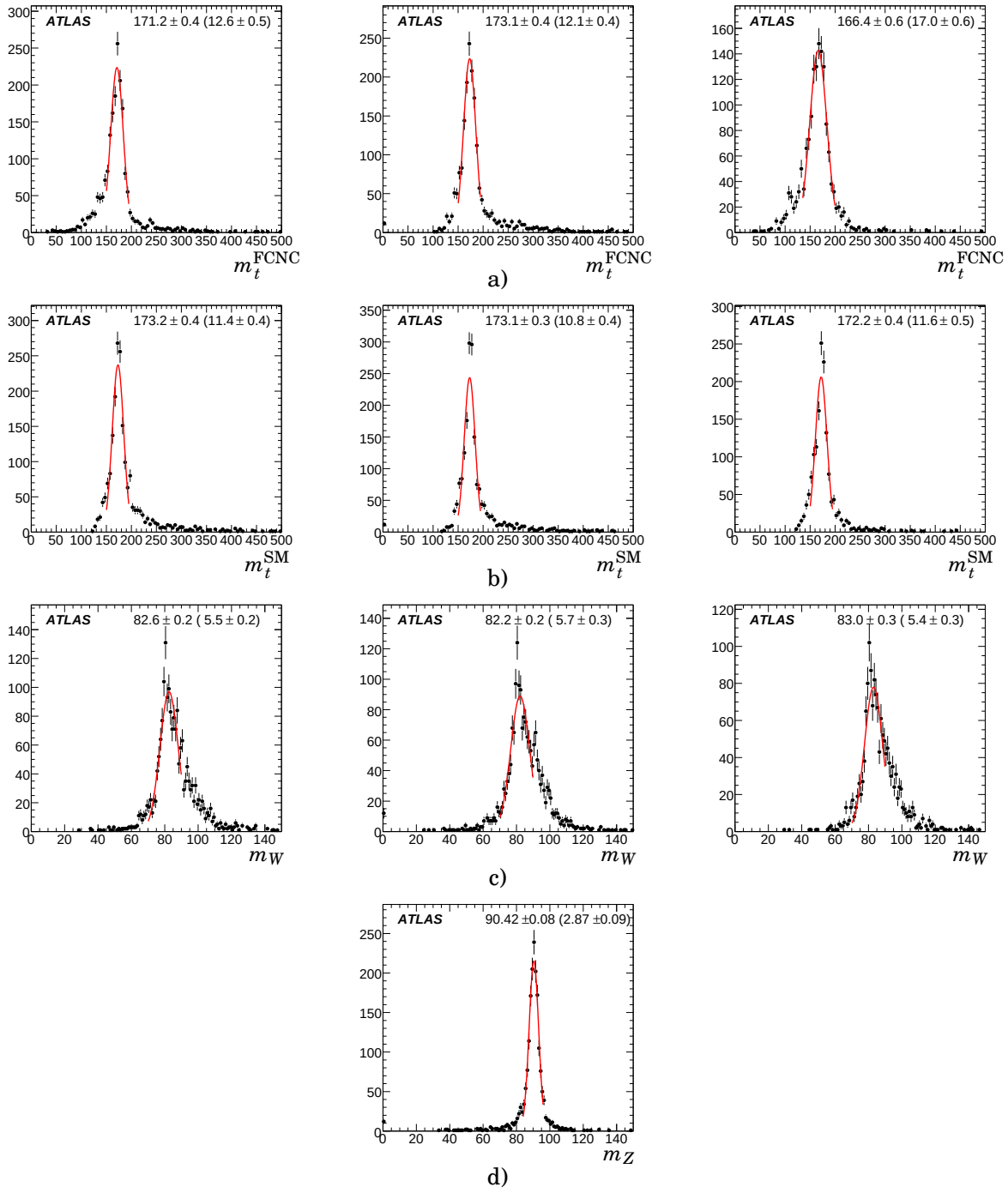

Figure 4.23: Distributions for the expected full simulated signal after the preselection of the $t \to q\gamma$ (left), $t \to qZ$ (centre) and $t \to qg$ (right) channels of the a) mass of the reconstructed top quark with FCNC decay, b) mass of the reconstructed top quark with SM decay, c) mass of the reconstructed W boson and d) mass of the reconstructed Z boson. The full lines represent the result of the fitted Gaussian functions to the masses distributions.

	$t \to q\gamma$	$t \to qZ$	$t \to qg$
full simulation samples:			
m_t^{FCNC} (σ)	171.2±0.4 (12.6±0.5)	173.1±0.4 (12.1±0.4)	166.4±0.6 (17.0±0.6)
m_t^{SM} (σ)	173.2±0.4 (11.4±0.4)	173.1±0.3 (10.8±0.4)	172.2±0.4 (11.6±0.5)
m_W (σ)	82.6±0.2 (5.5±0.2)	82.2±0.2 (5.7±0.3)	83.0±0.3 (5.4±0.3)
m_Z (σ)		90.42±0.08 (2.87±0.09)	
fast simulation samples:			
m_t^{FCNC} (σ)	172.69±0.04 (9.07±0.04)	173.17±0.05 (8.96±0.06)	164.9±0.2 (14.7±0.2)
m_t^{SM} (σ)	173.10±0.05 (10.56±0.05)	173.59±0.06 (10.12±0.07)	172.7±0.1 (10.4±0.1)
m_W (σ)	82.41±0.04 (5.63±0.04)	82.22±0.05 (5.52±0.05)	82.76±0.09 (5.47±0.09)
m_Z (σ)		90.75±0.01 (2.50±0.02)	

Table 4.8: The values of the masses and widths of the top quark decaying via FCNC (m_t^{FCNC}), the top quark decaying through SM (m_t^{SM}), the W boson (m_W) and the Z boson (m_Z), for the signal events, obtained by fitting Gaussian functions to the respective distributions, for full simulation and fast simulation samples.

$t \to q\gamma$ channel:

The requirements on the multiplicity of b-tagged jets and on the neutrino longitudinal momentum reconstruction were discarded. The other difference was that the event should pass the e25i (at least one isolated electron with p_T >25 GeV), mu20i (at least one isolated muon with p_T >20 GeV) or the g60 (at least one photon with p_T >60 GeV) trigger menus.

$t \to qZ$ channel:

Like for the $t \to q\gamma$ channel, the requirements on the multiplicity of b-tagged jets and on the neutrino longitudinal momentum reconstruction were not applied. The events should also pass the the e25i or the mu20i trigger menus.

$t \to qg$ channel:

Apart from the fact that the E_{vis} cut moved to the final selection, the only difference was that e25i or the mu20i trigger menus were required.

Number of selected events:

The expected number of background events and signal efficiencies after the final selection level are shown in Table 4.11. For the $t \to q\gamma$ channel, the dominant backgrounds are $t\bar{t}$, Z+jets and W+jets events, which correspond to 38%, 30% and 29% of the total background. The total background for the $t \to qZ$ channel is mainly composed of $t\bar{t}$ and Z+jets events (59% and 28% of the total background, respectively), while for the $t \to qg$ it is mainly composed of W+jets and $t\bar{t}$ events (which correspond, respectively, to 64% and 25% of the total background). The effect of each trigger level on the full simulated background and signal events, after all the other cuts, are shown in Table 4.12.

$\Delta R_{\text{reco}}^{\text{true}}$	0.2	0.4	0.8	1.2
$t \to q\gamma$:				
ε_q	63.2 ± 1.8	69.2 ± 1.9	72.8 ± 1.9	75.4 ± 2.0
ε_γ	99.8 ± 2.3	99.8 ± 2.3	99.8 ± 2.3	99.8 ± 2.3
$\varepsilon_{t^{\text{FCNC}}}$	59.7 ± 1.8	68.8 ± 1.9	77.2 ± 2.0	83.1 ± 2.1
ε_b	52.0 ± 1.6	57.4 ± 1.7	61.0 ± 1.8	64.1 ± 1.8
ε_ℓ	99.7 ± 2.3	99.7 ± 2.3	99.8 ± 2.3	99.8 ± 2.3
ε_ν	16.5 ± 0.9	36.0 ± 1.4	60.3 ± 1.8	73.4 ± 1.9
ε_W	31.3 ± 1.3	54.1 ± 1.7	76.1 ± 2.0	85.5 ± 2.1
$\varepsilon_{t^{\text{SM}}}$	27.9 ± 1.2	45.1 ± 1.5	62.8 ± 1.8	73.5 ± 1.9
$t \to qZ$:				
ε_q	55.7 ± 1.7	60.0 ± 1.8	63.6 ± 1.9	67.3 ± 1.9
ε_Z	94.6 ± 2.3	96.2 ± 2.3	97.2 ± 2.3	98.0 ± 2.3
$\varepsilon_{t^{\text{FCNC}}}$	54.2 ± 1.7	62.8 ± 1.8	72.8 ± 2.0	80.6 ± 2.1
ε_b	52.6 ± 1.7	57.3 ± 1.8	61.2 ± 1.8	64.9 ± 1.9
ε_ℓ	96.0 ± 2.3	96.0 ± 2.3	96.1 ± 2.3	96.6 ± 2.3
ε_ν	17.6 ± 1.0	35.9 ± 1.4	60.9 ± 1.8	74.1 ± 2.0
ε_W	30.5 ± 1.3	50.1 ± 1.6	71.1 ± 2.0	81.5 ± 2.1
$\varepsilon_{t^{\text{SM}}}$	28.3 ± 1.2	43.1 ± 1.5	61.2 ± 1.8	71.4 ± 2.0
$t \to qg$:				
ε_q	32.0 ± 1.5	35.3 ± 1.5	39.4 ± 1.6	43.9 ± 1.7
ε_g	37.2 ± 1.6	41.2 ± 1.6	44.6 ± 1.7	47.7 ± 1.8
$\varepsilon_{t^{\text{FCNC}}}$	47.0 ± 1.8	61.0 ± 2.0	72.2 ± 2.2	76.9 ± 2.3
ε_b	51.1 ± 1.8	56.6 ± 1.9	60.6 ± 2.0	63.9 ± 2.1
ε_ℓ	99.8 ± 2.6	99.8 ± 2.6	99.8 ± 2.6	99.8 ± 2.6
ε_ν	17.7 ± 1.1	37.0 ± 1.6	59.9 ± 2.0	72.6 ± 2.2
ε_W	33.5 ± 1.5	53.7 ± 1.9	74.8 ± 2.2	84.6 ± 2.4
$\varepsilon_{t^{\text{SM}}}$	27.5 ± 1.3	44.5 ± 1.7	61.0 ± 2.0	71.4 ± 2.2

Table 4.9: The obtained efficiencies of the kinematics reconstruction for each full simulated FCNC channel, after the preselection, for four different matching criteria: $\Delta R_{\text{reco}}^{\text{true}} < 0.2$, < 0.4, < 0.8 and < 1.2.

$\Delta R_{\text{reco}}^{\text{true}}$	0.2	0.4	0.8	1.2
$t \to q\gamma$:				
ε_q	75.2 ± 0.3	81.0 ± 0.3	84.1 ± 0.3	85.8 ± 0.3
ε_X	99.0 ± 0.3	99.6 ± 0.3	99.8 ± 0.3	99.9 ± 0.3
$\varepsilon_{t^{\text{FCNC}}}$	72.1 ± 0.3	81.0 ± 0.3	87.7 ± 0.3	91.2 ± 0.3
ε_b	68.2 ± 0.3	73.4 ± 0.3	76.7 ± 0.3	79.0 ± 0.3
ε_ℓ	98.6 ± 0.4	99.6 ± 0.4	99.9 ± 0.4	100.0 ± 0.4
ε_ν	20.2 ± 0.2	39.9 ± 0.2	61.7 ± 0.3	73.5 ± 0.3
ε_W	34.7 ± 0.2	54.5 ± 0.3	74.6 ± 0.3	85.4 ± 0.3
$\varepsilon_{t^{\text{SM}}}$	36.4 ± 0.2	54.6 ± 0.3	73.2 ± 0.3	82.5 ± 0.3
$t \to qZ$:				
ε_q	69.4 ± 0.4	74.3 ± 0.4	77.2 ± 0.4	79.3 ± 0.4
ε_X	93.4 ± 0.5	95.9 ± 0.5	97.1 ± 0.5	97.7 ± 0.5
$\varepsilon_{t^{\text{FCNC}}}$	68.5 ± 0.4	76.3 ± 0.4	83.1 ± 0.4	87.3 ± 0.5
ε_b	66.8 ± 0.4	71.8 ± 0.4	74.8 ± 0.4	77.0 ± 0.4
ε_ℓ	89.6 ± 0.5	90.7 ± 0.5	91.3 ± 0.5	91.8 ± 0.5
ε_ν	21.4 ± 0.2	41.4 ± 0.3	62.6 ± 0.4	73.5 ± 0.4
ε_W	32.2 ± 0.3	51.1 ± 0.3	70.5 ± 0.4	81.2 ± 0.4
$\varepsilon_{t^{\text{SM}}}$	34.9 ± 0.3	51.9 ± 0.3	69.3 ± 0.4	78.3 ± 0.4
$t \to qg$:				
ε_q	37.6 ± 0.5	40.7 ± 0.6	43.0 ± 0.6	45.3 ± 0.6
ε_X	40.5 ± 0.6	42.8 ± 0.6	44.1 ± 0.6	45.6 ± 0.6
$\varepsilon_{t^{\text{FCNC}}}$	57.9 ± 0.7	70.0 ± 0.7	78.2 ± 0.8	82.7 ± 0.8
ε_b	64.6 ± 0.7	68.3 ± 0.7	71.5 ± 0.7	74.1 ± 0.8
ε_ℓ	99.6 ± 0.9	99.9 ± 0.9	100.0 ± 0.9	100.0 ± 0.9
ε_ν	19.3 ± 0.4	40.2 ± 0.6	61.8 ± 0.7	73.2 ± 0.8
ε_W	34.7 ± 0.5	54.0 ± 0.6	73.8 ± 0.8	84.6 ± 0.8
$\varepsilon_{t^{\text{SM}}}$	32.9 ± 0.5	49.9 ± 0.6	66.9 ± 0.7	76.0 ± 0.8

Table 4.10: The obtained efficiencies of the kinematics reconstruction for each fast simulated FCNC channel, after the preselection, for four different matching criteria: $\Delta R_{\text{reco}}^{\text{true}} < 0.2$, < 0.4, < 0.8 and < 1.2.

	Z+jets	W+jets	WZ pairs	$t\bar{t}$	single top	total background	signal efficiency %
after final selection (the trigger is included)							
$t\bar{t} \to bWq\gamma$:							
e	182 ± 28	120 ± 56	7 ± 2	118 ± 11	8 ± 3	435 ± 63	3.6 ± 0.2
μ	11 ± 11	66 ± 55	4 ± 2	130 ± 11	6 ± 3	216 ± 57	4.1 ± 0.2
ℓ	193 ± 28	187 ± 58	10 ± 3	248 ± 15	13 ± 4	650 ± 66	7.6 ± 0.2
$t\bar{t} \to bWqZ$:							
$3e$	12 ± 12	0 ± 53	2 ± 2	15 ± 5	0 ± 2	28 ± 55	1.4 ± 0.1
3μ	0 ± 11	0 ± 53	6 ± 2	5 ± 4	0 ± 2	11 ± 55	2.5 ± 0.1
3ℓ	35 ± 16	0 ± 53	16 ± 3	74 ± 8	0 ± 2	125 ± 56	7.6 ± 0.2
$t\bar{t} \to bWqg$:							
e	290 ± 33	7763 ± 302	81 ± 10	2304 ± 45	551 ± 26	10988 ± 308	1.3 ± 0.1
μ	327 ± 55	4623 ± 176	77 ± 9	2567 ± 47	671 ± 29	8265 ± 193	1.5 ± 0.1
ℓ	617 ± 63	12386 ± 345	157 ± 13	4871 ± 65	1222 ± 39	19252 ± 359	2.9 ± 0.1

Table 4.11: The expected number of background events and signal efficiencies after the final selection level (the trigger is included) of the analyses for each FCNC channel. The expected background numbers are normalised to $L = 1$ fb^{-1}.

	$t \to q\gamma$		$t \to qZ$		$t \to qg$	
	sig.	back.	sig.	back.	sig.	back.
L1	100.0	100.0	99.9	100.0	90.4	90.0
L2	99.9	100.0	99.5	96.9	87.0	85.5
EF	99.6	99.5	99.2	95.0	83.2	82.2

Table 4.12: The reduction, in percentage, for each trigger level on the background and signal events after all the other cuts on the FCNC analyses.

Discriminant analysis

Due to the small statistics of the available full simulation samples, the fast simulation samples were used to obtain the pdf and to compute the discriminant variables of the full simulated samples. The pdf distributions are shown from Figure 4.24 to Figure 4.28. An attempt to use only distributions without large differences between fast and full simulations was done and new variables were tested.

For the $t \to q\gamma$ channel, it was realised that the number of jets pdf had significant differences between the fast and the full simulations of the background, due to the different generators used and generated phase space. This pfd was then substituted by the reconstructed mass of the photon and the b quark ($m_{b\gamma}$).

For the $t \to qZ$ channel, two new pdf were added, in order to increase the signal and background discrimination: the reconstructed mass of the Z and the b quark (m_{bZ}) and the reconstructed mass of the two quarks (m_{qb}).

A new pdf was considered for the $t \to qg$ channel, in order to increase the signal and background discrimination: the reconstructed mass of the light and the b quark (m_{qb}).

The distributions of the discriminant variables obtained for the three FCNC channels under study are presented in Figure 4.29. It can be seen that ATLFAST describes the fully simulated distributions fairly well, when the statistics is sufficient to tell.

4.4 Results and systematic uncertainties

The same methods explained in section 3.4 were used to derive the 5σ sensitivities and the expected limits at 95% CL in the absence of a FCNC top quark decay signal. The full simulation samples were used to compute the limits, and no cuts on the discriminant variables were used. The 95% CL limits are shown, together with the statistical and systematic uncertainties $\pm 1\sigma$ bands, in Table 4.13. As expected, the limits of the sub-samples with muons have better limits than those of the sub-samples with electrons. During the first data taking, the performance of the objects reconstruction in real data can be degraded in relation to the expected from the full simulation. This should not affect the identification of muons, since it is based on signals from the dedicated ATLAS Muon System. Therefore, if non expected problems are found, the analyses can still be done using only the muons sub-samples. Nevertheless, the combination of the two sub-samples gives better results (for the $t \to qZ$ channel, it should be noted that the full sample is composed of the sub-samples with only electrons, only muons and, additionally, electrons and muons). The branching ratio sensitivity for each FCNC channel, assuming a signal discovery with a 5σ significance, is on average 3.0 times larger than the values presented in Table 4.13.

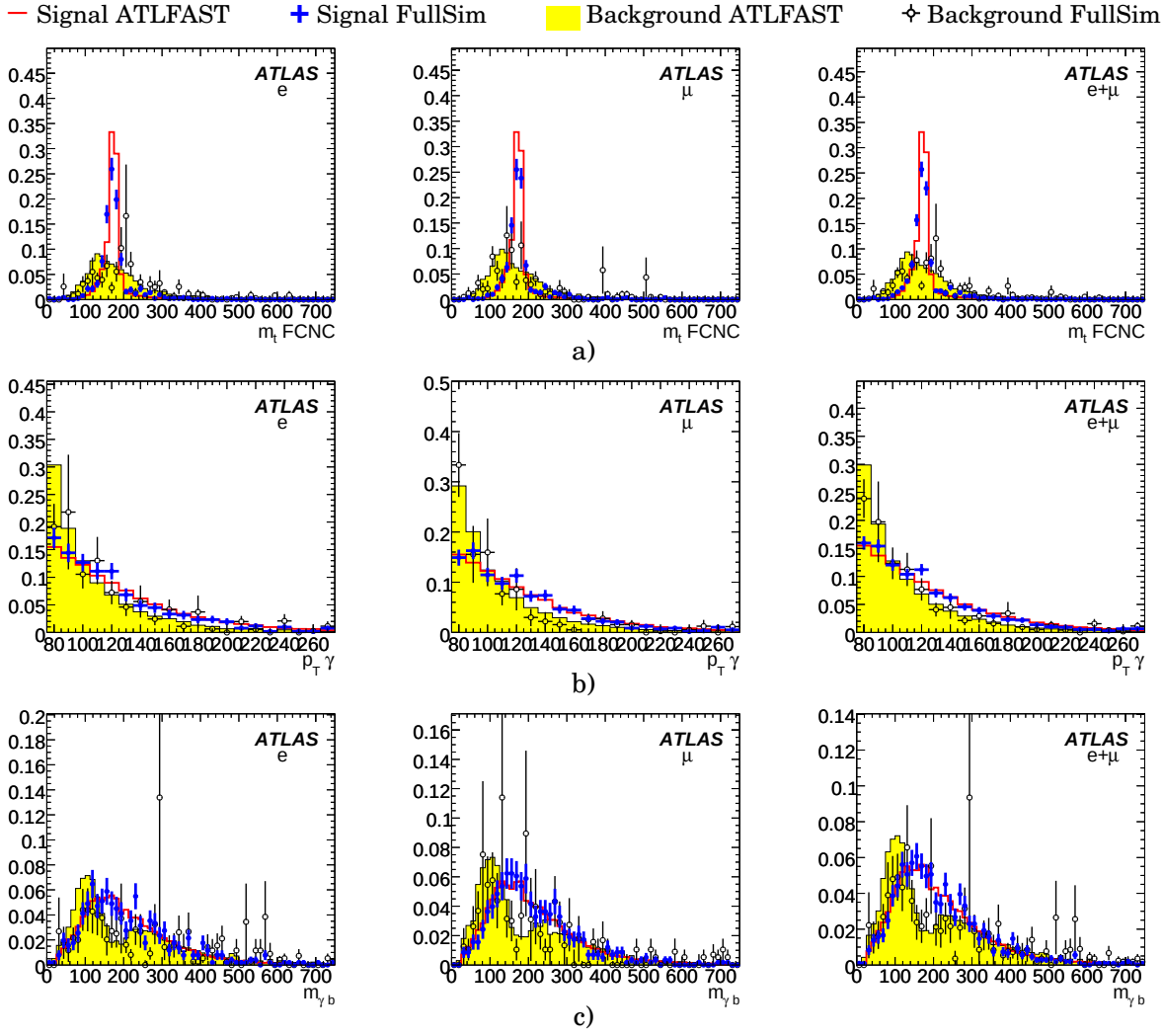

Figure 4.24: Distributions of the probability density functions for the expected background and signal after the final selection level, used in the $t \to q\gamma$ channel, when the isolated lepton is identified as an electron (left), a muon (centre) and electron or muon (left): a) mass of the reconstructed top quark with FCNC decay (m_t^{FCNC}), b) transverse momentum of the leading photon (p_T^{γ}) and c) reconstructed mass of the photon and the b quark ($m_{\gamma b}$).

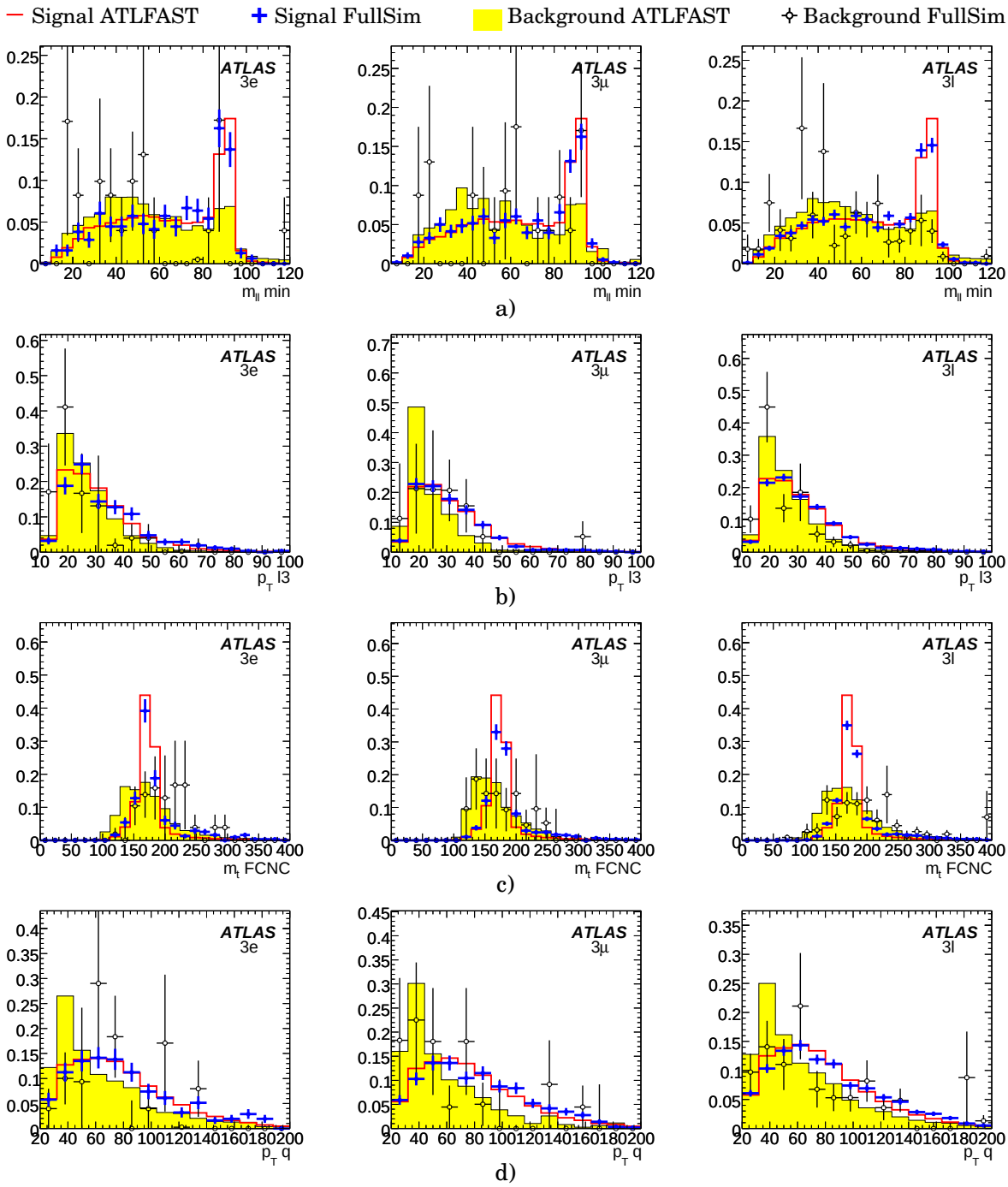

Figure 4.25: Distributions of the probability density functions for the expected background and signal after the final selection level, used in the $t \to qZ$ channel, when the three isolated leptons are identified as electrons (left), muons (centre) and electrons or muons (right): a) minimum invariant mass of the three possible combinations of two leptons ($m_{\ell\ell}^{\text{min}}$), b) the transverse momentum of the third lepton ($p_T^{\ell_3}$), c) mass of the top quark with FCNC decay (m_t^{FCNC}) and d) the transverse momentum of the light quark (p_T^q).

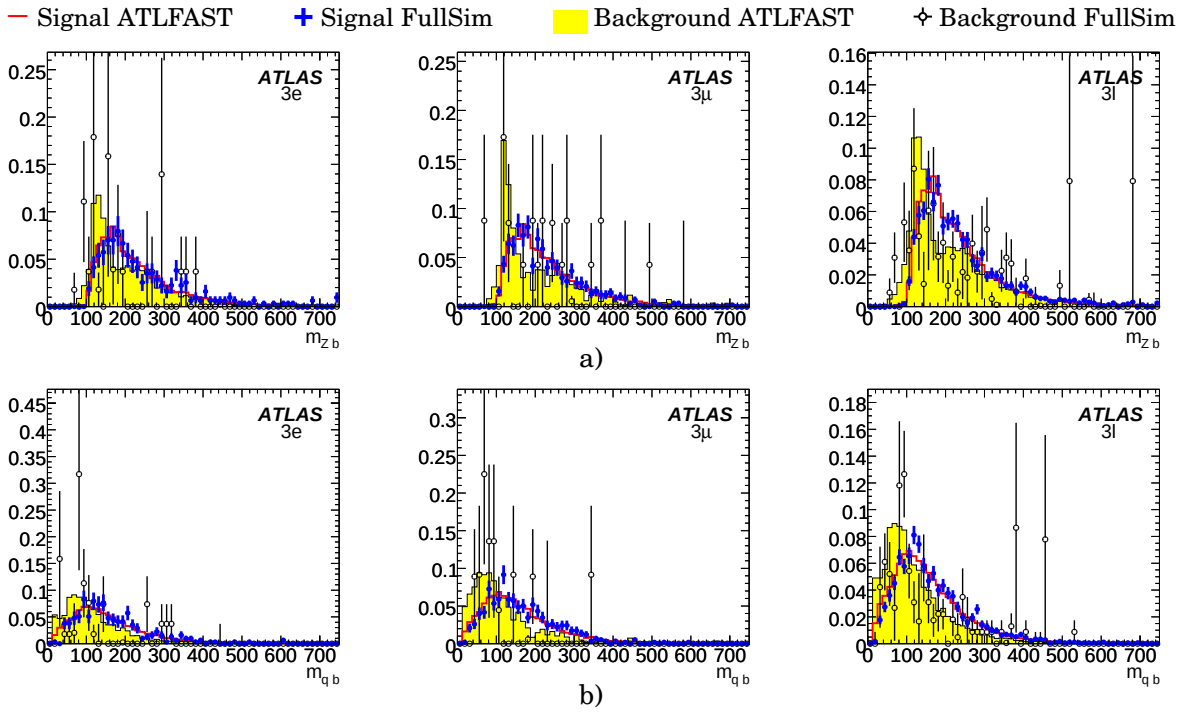

Figure 4.26: Distributions of the probability density functions for the expected background and signal after the final selection level, used in the $t \to qZ$ channel, when the three isolated leptons are identified as electrons (left), muons (centre) and electrons or muons (right): a) the reconstructed mass of the Z and the b quark (m_{Zb}) and b) the reconstructed mass of the two quarks (m_{qb}).

	-1σ	expected	$+1\sigma$
$t\bar{t} \to bWq\gamma$:			
e	4.3×10^{-4}	1.1×10^{-3}	1.9×10^{-3}
μ	4.5×10^{-4}	8.3×10^{-4}	1.3×10^{-3}
ℓ	3.8×10^{-4}	6.8×10^{-4}	1.0×10^{-3}
$t\bar{t} \to bWqZ$:			
$3e$	5.5×10^{-3}	9.4×10^{-3}	1.4×10^{-2}
3μ	2.4×10^{-3}	4.2×10^{-3}	6.4×10^{-3}
3ℓ	1.9×10^{-3}	2.8×10^{-3}	4.2×10^{-3}
$t\bar{t} \to bWqg$:			
e	1.3×10^{-2}	2.1×10^{-2}	3.0×10^{-2}
μ	1.0×10^{-2}	1.7×10^{-2}	2.4×10^{-2}
ℓ	7.2×10^{-3}	1.2×10^{-2}	1.8×10^{-2}

Table 4.13: The expected 95% confidence level limits on the FCNC top decay branching ratio, in the absence of signal, are shown for a luminosity of $L = 1$ fb^{-1}. The central values are represented together with the $\pm 1\sigma$ bands, which include the contribution from the statistical and systematic uncertainties.

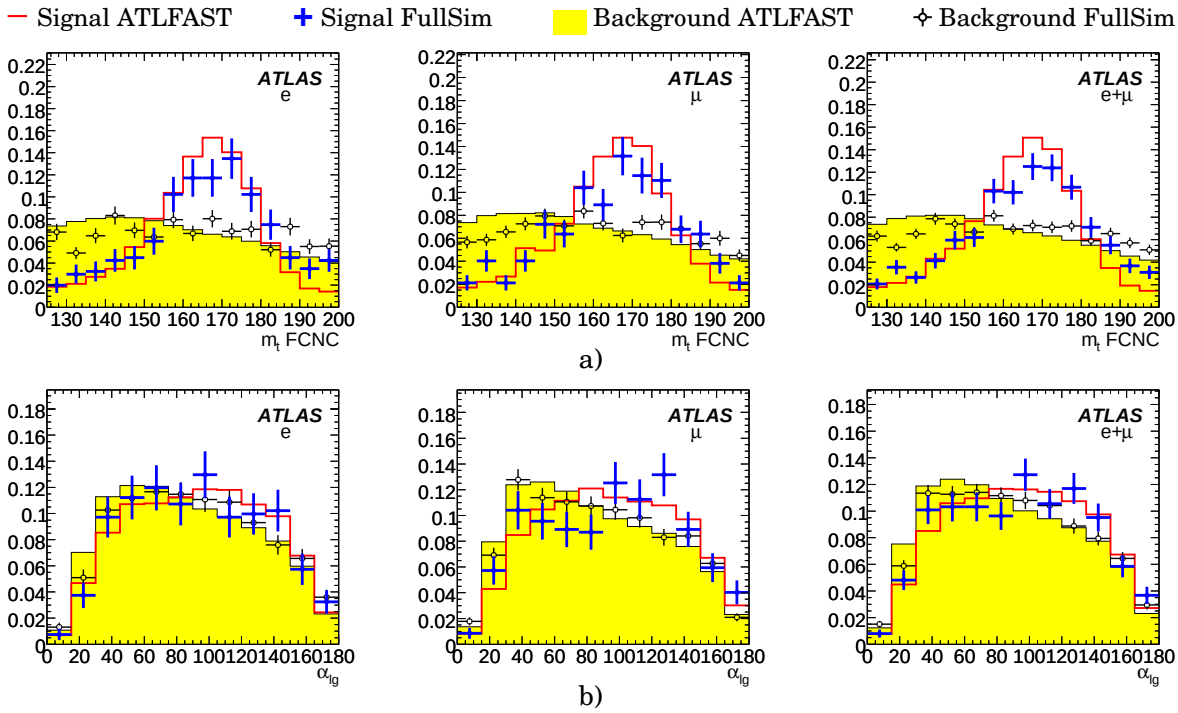

Figure 4.27: Distributions of the probability density functions for the expected background and signal after the final selection level, used in the $t \to qg$ channel, when the isolated lepton is identified as an electron (left), a muon (centre) and electron or muon (left): a) the mass of the top quark with FCNC decay (m_t^{FCNC}) and b) the angle between the lepton and the gluon ($\alpha_{\ell g}$).

Several sources of systematic uncertainties were studied, although the relatively small statistics of the MC full simulation samples do not allow for a precise determination. For this reason, the determination of the systematic uncertainties will be convoluted with the statistical errors, and thus it will be conservative. The results are shown in Table 4.14. Some of the contributions were studied using the samples listed in Table 4.2. The following sources of systematic errors were considered in this study:

- jet energy calibration: the value of the energy scale of the jets was changed from -15 to +15%, in steps of 5%, and the relative changes between the obtained FCNC BR and the reference FCNC BR were fitted with linear functions (for the $t \to qg$ channel, these fits were performed with quadratic functions), as can be seen in Figure 4.30. The systematic error was considered as the effect of a variation of 5% in the energy scale of the jets;

- luminosity: the value of the luminosity used to normalize the background samples was changed from -20% to $+20\%$, in steps of 10%. The obtained values of the relative FCNC BR changes were fitted with linear functions. Figure 4.31 shows these distributions. The systematic error was conservatively considered as the effect of a variation of 20%;

- top quark mass: the full simulation samples, with $m_t = 175$ GeV, were analysed considering the values of 170 GeV and 180 GeV for the pdf definitions (done again with ATLFAST samples), for the χ^2 evaluation of expression 4.1 and for the limit computation (since the predicted $t\bar{t}$ cross-section depends on the top quark mass). Linear functions were fitted to the relative changes of the FCNC BR limits (see Figure 4.32), and the systematic error was estimated for a top mass uncertainty of 2 GeV;

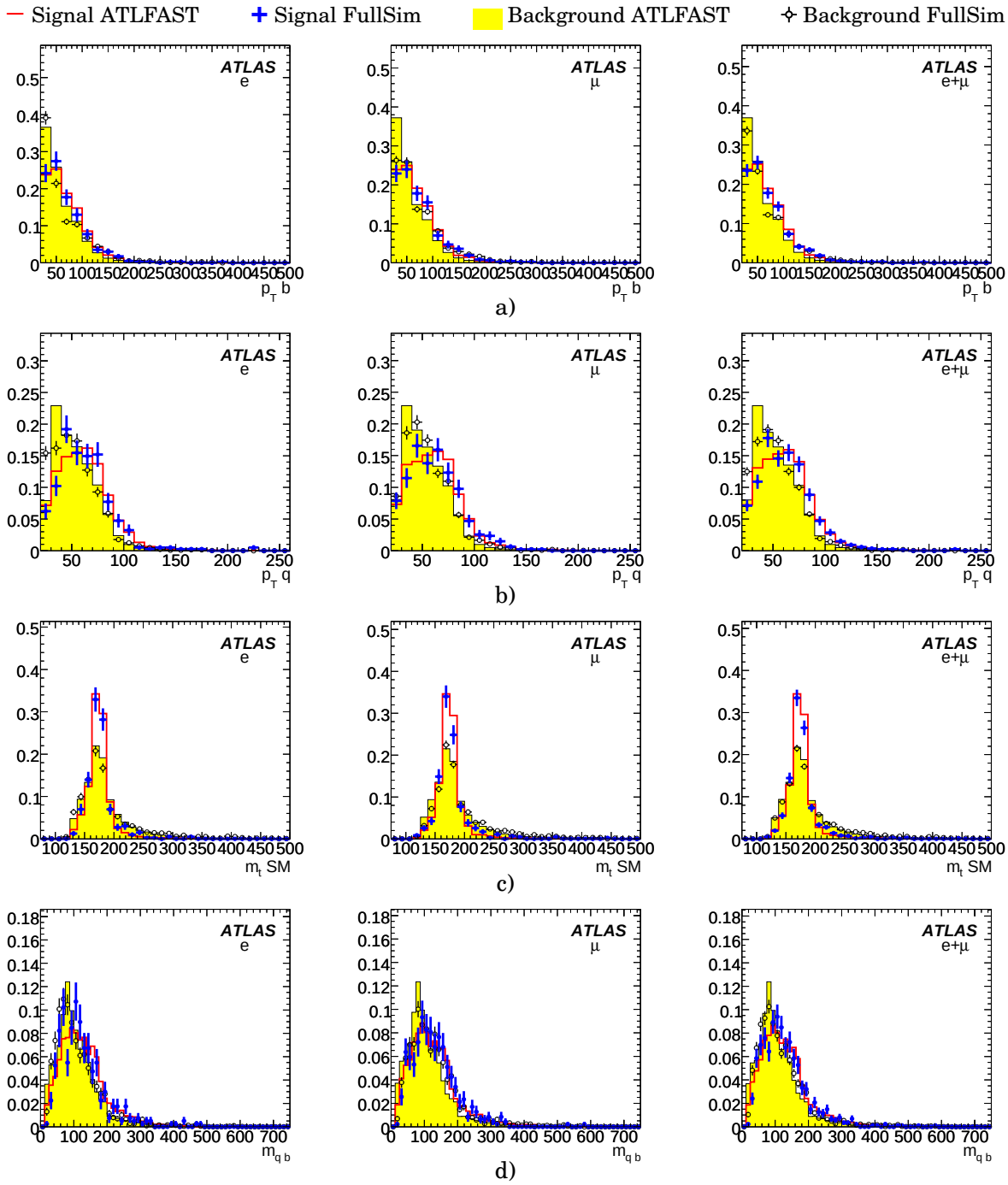

Figure 4.28: Distributions of the probability density functions for the expected background and signal after the final selection level, used in the $t \to qg$ channel, when the isolated lepton is identified as an electron (left), a muon (centre) and electron or muon (left): a) transverse momentum of the b quark (p_T^b), b) transverse momentum of the light quark (p_T^q), c) the mass of the top quark with SM decay (m_t^{SM}) and d) the reconstructed mass of the light and the b quark (m_{qb}).

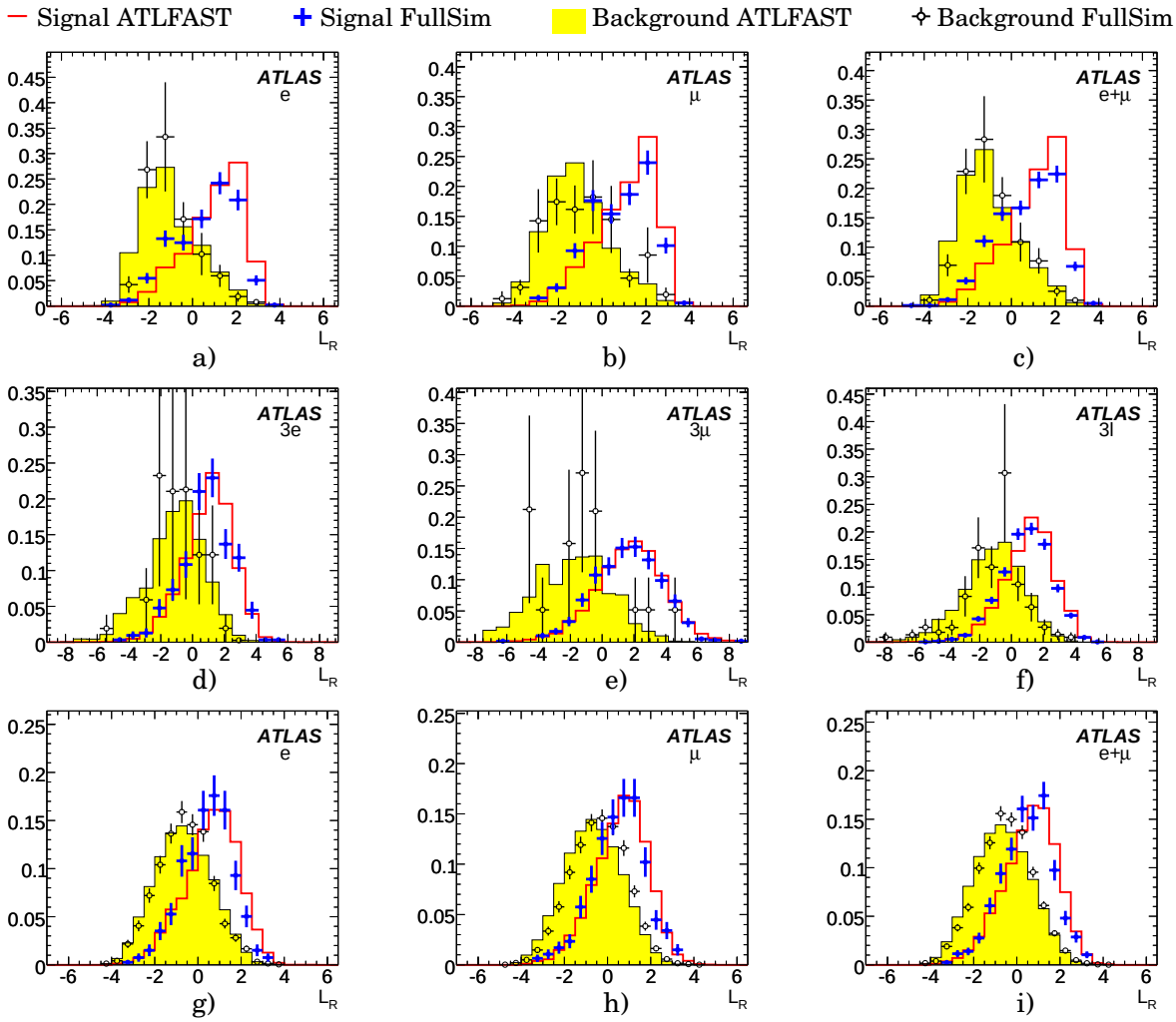

Figure 4.29: Distributions of the normalised discriminant variables for the expected background and signal after the final selection level, for $L = 1$ fb^{-1}, of the $t \to q\gamma$ channel when the isolated lepton is identified as (a) an electron, (b) a muon and (c) electron or muon; of the $t \to qZ$ channel when the 3 isolated leptons are identified as (d) electrons, (e) muons and (f) electrons or muons and of the $t \to qg$ channel, when the isolated lepton is identified as (g) an electron, (h) a muon and (i) electron or muon.

	$t \to q\gamma$			$t \to qZ$			$t \to qg$		
source	e	μ	ℓ	$3e$	3μ	3ℓ	e	μ	ℓ
systematic uncertainties:									
jet energy calibration	1%	2%	2%	3%	2%	5%	4%	4%	4%
luminosity	9%	8%	10%	3%	2%	6%	10%	8%	10%
top mass	7%	7%	6%	6%	4%	12%	7%	5%	5%
backgrounds σ	6%	10%	7%	4%	7%	12%	17%	16%	15%
ISR/FSR	21%	18%	17%	6%	29%	7%	3%	7%	9%
pile-up	37%	21%	22%	30%	14%	0%	8%	10%	13%
generator	34%	18%	4%	4%	14%	14%	5%	0%	4%
χ^2	5%	0%	4%	2%	5%	7%	3%	7%	9%
total	56%	36%	32%	32%	36%	25%	24%	24%	27%
analysis stability:									
selection criteria	17%	4%	3%	8%	12%	8%	6%	4%	5%

Table 4.14: Maximum changes (with respect to the central values of Table 4.13) of the expected 95% CL limits for each FCNC top quark decay branching ratio for different systematic error sources.

- backgrounds cross-sections: the cross-sections for the full simulation backgrounds were varied individually ($\pm$12% for $t\bar{t}$ production, $\pm$6% for single top, $\pm$50% for W+jets, $\pm$20% for Z+plus and $\pm$15% WZ pairs). The systematic error was considered as the quadratic sum of all background contributions;

- ISR/FSR: the effect of the ISR and FSR parameterisation was studied by changing the different switches of the AcerMC generator interfaced with the Pythia parton showering, which control the ISR and FSR. The available samples listed in Table 4.2 (6250 and 6251) were used to compute the maximum relative FCNC BR changes;

- pile-up: the effect of pile-up events was studied by comparing the values of the observables obtained with and without adding pile-up events (an average of 4.6 pile-up events per bunch crossing). The available samples with pile-up are listed in Table 4.2;

- MC generator: the effect of the MC generator was studied by using different $t\bar{t}$ SM background samples, obtained with the AcerMC generator;

- kinematics reconstruction: in order to study the systematic uncertainties associated to the χ^2 distribution of expression 4.1, and since no cut is applied to this distribution, the ratio $\Gamma_{m_t}/\Gamma_{m_W}$ was changed by a factor 2.

The total contributions of the studied systematic uncertainties are of the same order of magnitude of the statistical 1σ bands. The analysis stability was also cross-checked by varying the kinematic cuts by 10%, and the maximum relative change on the expected 95% CL limits was 3%, 9% and 5% for the $t \to q\gamma$, $t \to qZ$ and $t \to qg$ channels, respectively. The limits shown in Table 4.13 include the contributions from statistics and systematic uncertainties, as

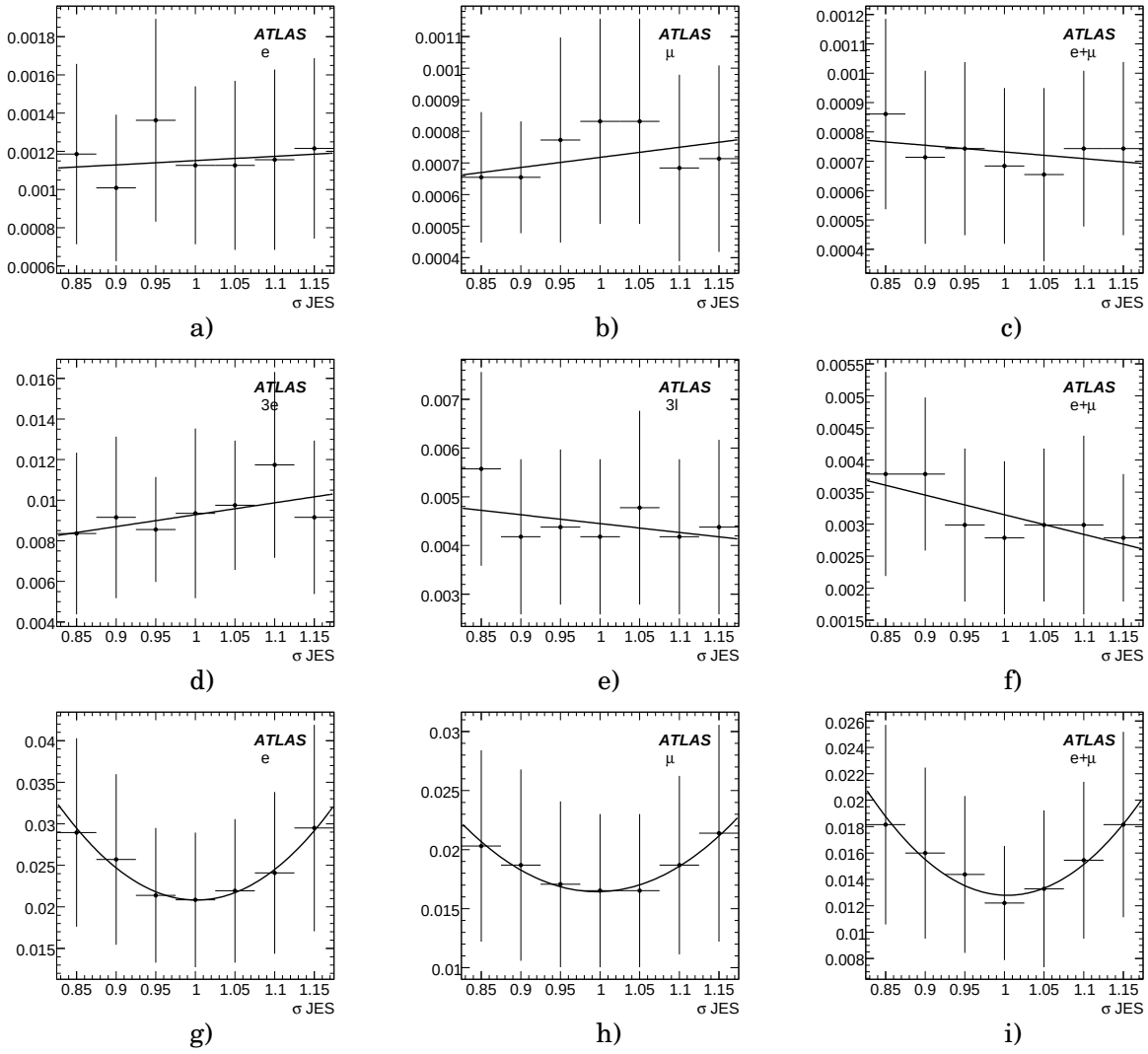

Figure 4.30: Dependence of the 95% CL expected limits on the jet energy scale for the $t \to q\gamma$ channel when the isolated lepton is identified as (a) an electron, (b) a muon and (c) electron or muon; for the $t \to qZ$ channel when the 3 isolated leptons are identified as (d) electrons, (e) muons and (f) electrons or muons and for the $t \to qg$ channel, when the isolated lepton is identified as (g) an electron, (h) a muon and (i) electron or muon.

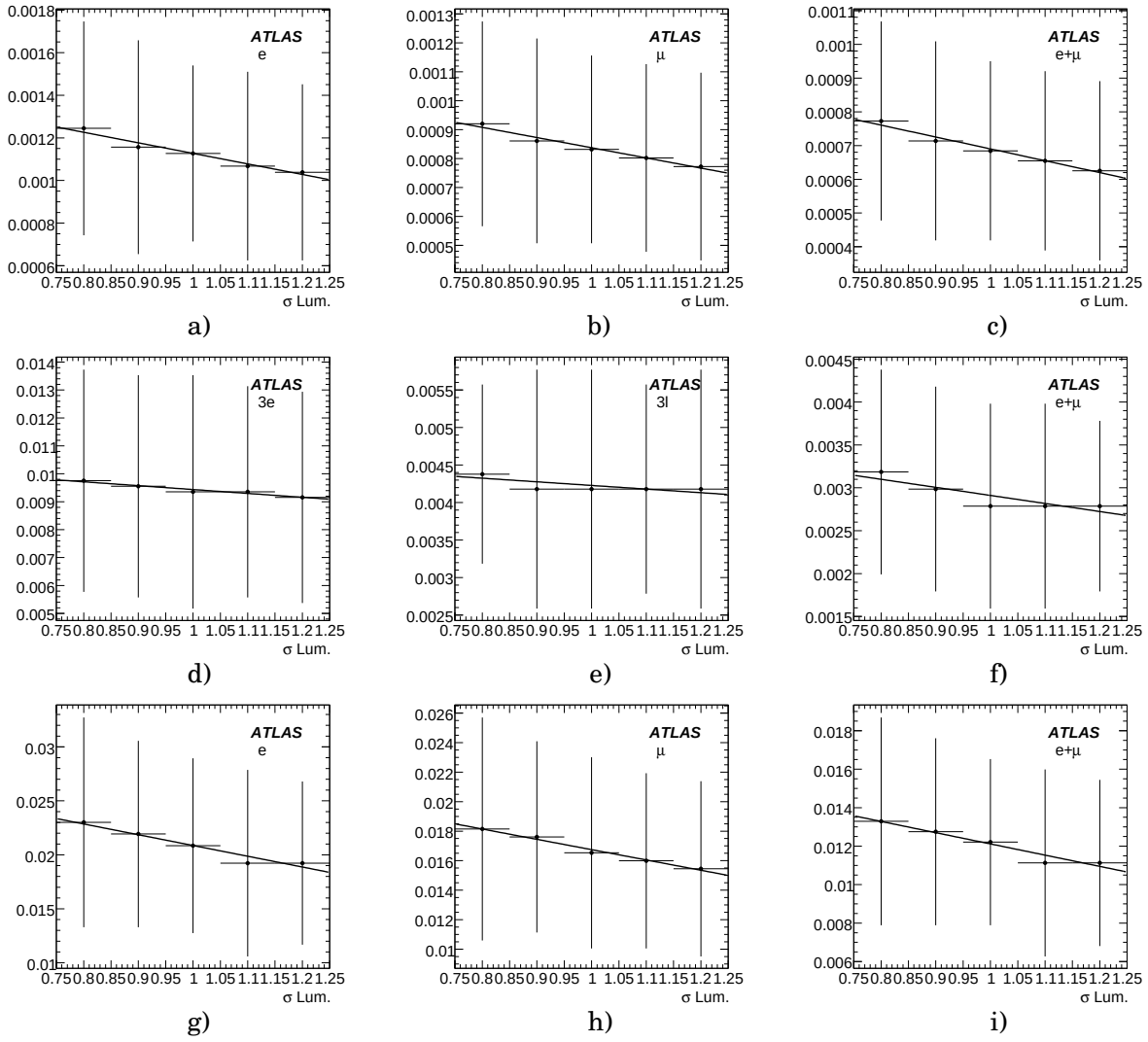

Figure 4.31: Dependence of the 95% CL expected limits on the luminosity measurement for the $t \to q\gamma$ channel when the isolated lepton is identified as (a) an electron, (b) a muon and (c) electron or muon; for the $t \to qZ$ channel when the 3 isolated leptons are identified as (d) electrons, (e) muons and (f) electrons or muons and for the $t \to qg$ channel, when the isolated lepton is identified as (g) an electron, (h) a muon and (i) electron or muon.

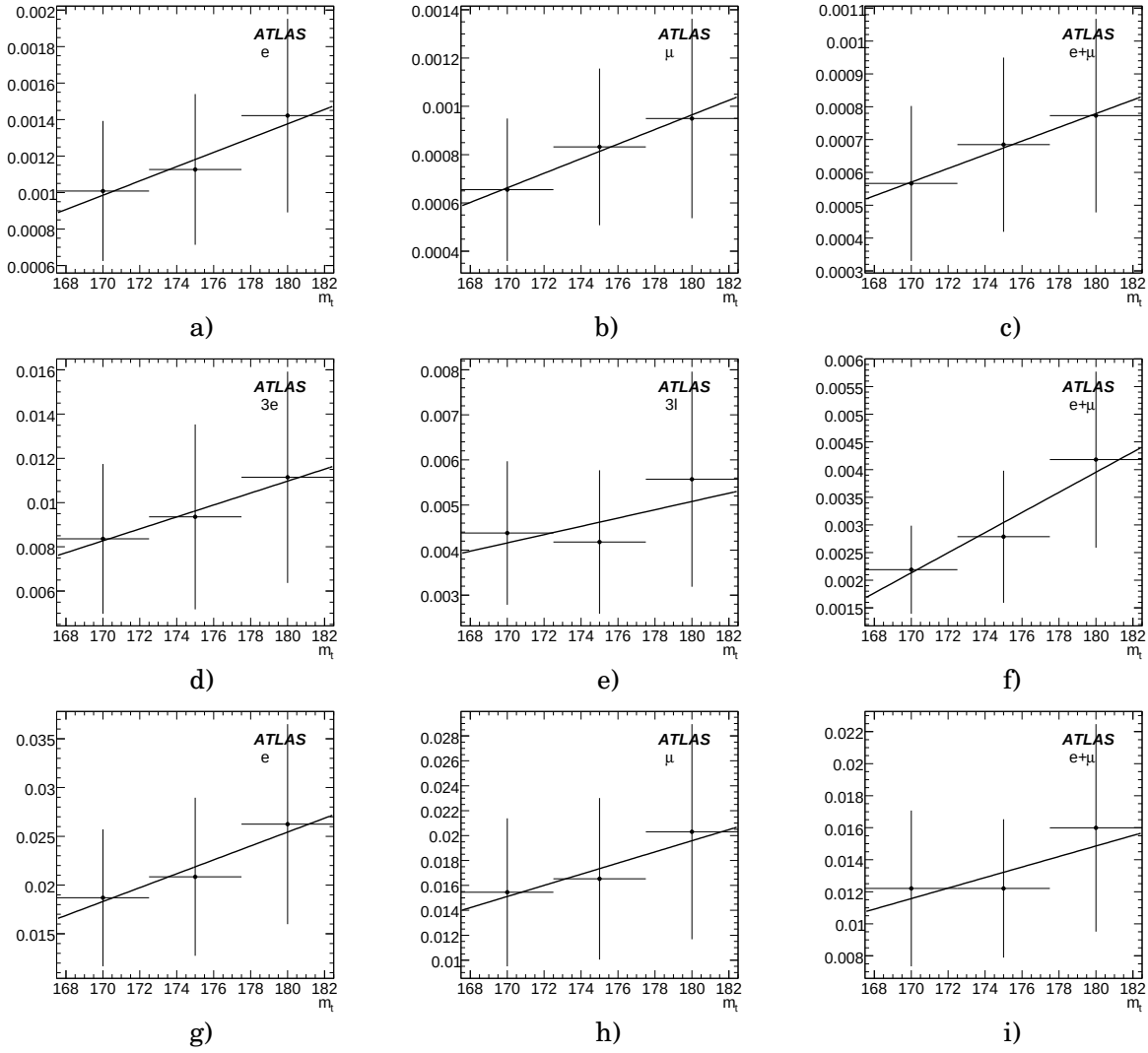

Figure 4.32: Dependence of the 95% CL expected limits on the top quark mass for the $t \to q\gamma$ channel when the isolated lepton is identified as (a) an electron, (b) a muon and (c) electron or muon; for the $t \to qZ$ channel when the 3 isolated leptons are identified as (d) electrons, (e) muons and (f) electrons or muons and for the $t \to qg$ channel, when the isolated lepton is identified as (g) an electron, (h) a muon and (i) electron or muon.

1σ bands. The contribution from the luminosity and the absolute value of background level may be reduced with data, by normalising to measured processes.

5

Discussion of the results

In this Chapter, comparisons between the results of the analyses for high and low luminosities, between these analyses and previous ones from ATLAS, as well from CMS and the present observed limits from LEP, HERA and Tevatron are draw. In the end, some considerations about future work and improvements are presented.

5.1 Comparison between high and low luminosities results

In order to compare the limits for the high (L = 10 fb^{-1} and L = 100 fb^{-1}) and low (L = 1 fb^{-1}) luminosity analyses, obtained in the two previous Chapters, it must be taken into account the differences in luminosities, lepton and photon identification efficiencies, trigger efficiencies, mistag and background cross-sections. The corrections are based on expression 3.11. A detailed description of the corrections is given in Appendix A.

The low luminosity limits converted to 10 fb^{-1} are shown in Table 5.1. As can be seen, the limits are compatible with each other, if the differences in luminosities, in lepton and photon identification efficiencies, in trigger efficiencies and in background cross-sections are taken into account. It should be noted that the difference between the limits for the $t \to q\gamma$ channel can be explained by the large uncertainty in the determination of the correction factor related to the effect from the different background cross-sections.

5.2 Comparison with other analyses

Previous complementary cut-based analyses dedicated to the study of the sensitivity of the ATLAS detector for the search of FCNC top quark decays were developed and their results are summarised in Table 5.2. Comparing these results with the ones presented in Tables 3.10 and 3.11, it can be seen that for the $t \to q\gamma$, the analysis presented here is three times better that the one of [97]. For the $t \to qZ$ channel, the results presented here are similar to those from two analyses done earlier [97, 91]. It can also be seen that the $t \to qZ$ channels with hadronic decays ($t\bar{t} \to b\ell\nu qqq$) are less sensitive than the one with pure leptonic decays ($t\bar{t} \to b\ell\nu q\ell\ell$) and which was used in this study. For the $t \to qg$ channel, the study presented here is the only one based on $t\bar{t}$ production followed by FCNC decay and is one order of magnitude better than the ones based on same-charge top pair production [119, 120] and on direct single top production [121]. The analysis presented in [122, 123] is also based on direct single top production, but its results are about one order of magnitude better than the ones presented

	-1σ	expected	$+1\sigma$
$L = 1$ fb^{-1} converted to $L = 10$ fb^{-1}:			
$t \to q\gamma$	4.6×10^{-5}	8.3×10^{-5}	1.2×10^{-4}
$t \to qZ$	2.2×10^{-4}	3.2×10^{-4}	4.8×10^{-4}
$t \to qg$	1.3×10^{-3}	2.2×10^{-3}	3.2×10^{-3}
$L = 10$ fb^{-1} (from Table 3.11):			
$t \to q\gamma$	2.5×10^{-5}	4.1×10^{-5}	6.2×10^{-5}
$t \to qZ$	2.2×10^{-4}	3.1×10^{-4}	4.3×10^{-4}
$t \to qg$ "3 jets"	1.0×10^{-3}	1.6×10^{-3}	2.3×10^{-3}

Table 5.1: The expected 95% confidence level limits on the FCNC top quark decay branching ratios in the absence of signal hypothesis obtained with the analyses for low luminosity (1 fb^{-1}) converted to high luminosity (10 fb^{-1}) are shown. See text for details. The limits computed for high luminosity (Table 3.11) are also shown for the sake of comparison. The central values are presented together with the $\pm 1\sigma$ bands, which include the contribution from the statistical and systematic uncertainties.

here, since the expected background contribution for the direct single top production analysis is much smaller.

In order to test the complementarity and the possibility to combine results, a study with single top (t-channel) events with FCNC decays was also performed [98]. Only the $t \to q\gamma$ and the $t \to qZ$ FCNC decay channels were considered, since the $t \to qg$ channel would lead to a fully hadronic event and thus would be submerged under a very large QCD background. For details about the analyses see [98]. The results are shown in Table 5.2 and are about one order of magnitude higher than the ones obtained with the top pair production. Therefore, no combination was performed between the analyses, as no real gain is expected. Nevertheless, since these analyses for single top quark events are easier and complementary to the ones for $t\bar{t}$, they should not be discarded.

Table 5.2 also shows the sensitivity studies done by the CMS collaboration for the $t \to q\gamma$ and $t \to qZ$ decay channels in top quark pair production [124]. It should be noted that their 5σ results were evaluated defining the statistical significance $\mathscr{S} = 2(\sqrt{B+S} - \sqrt{B})$. With this definition, the ATLAS 5σ limits for 10 fb^{-1} are 1.6×10^{-4} and 1.3×10^{-3} for the $t \to q\gamma$ and the $t \to qZ$ channels, respectively. Therefore, the results presented here are about three times better for the $t \to q\gamma$ channel and are similar for the $t \to qZ$ channel. The results from ATLAS and CMS were combined using the modified frequentist likelihood method and the results obtained for a 95% CL are also presented in Table 5.2. For the $t \to qZ$ channel the combined result is about $\sqrt{2}$ times better as expected by the luminosity factor, while for the $t \to q\gamma$ channel, the combined result is only slightly better because of the difference between the ATLAS and CMS individual limits.

The expected ATLAS sensitivity for the FCNC top quark decays with 1 fb^{-1} is about one order of magnitude better than the present experimental limits, for the $t \to q\gamma$ and $t \to qZ$ channels, while for the $t \to qg$ channel the limits are similar, as can be seen from Table 1.3. With 100 fb^{-1}, the ATLAS sensitivity for the $t \to q\gamma$ and $t \to qZ$ channels is at least 2 orders of magnitude better than the current limits and about one order of magnitude for the $t \to qg$. Figure 5.1 shows the ATLAS 95% CL expected sensitivity for 1 fb^{-1}, 10 fb^{-1} and 100 fb^{-1} in

Collaboration	channel	5σ BR	95% CL BR	L	ref.
$t \to q\gamma$:					
ATLAS	$t\bar{t} \to b\ell\nu q\gamma$	1.0×10^{-4}		100 fb^{-1}	[97]
ATLAS	$t \to q\gamma$ (t-channel)	1.1×10^{-3}	3.5×10^{-4}	10 fb^{-1}	[98] †
CMS	$t\bar{t} \to b\ell\nu q\gamma$	8.4×10^{-4}		10 fb^{-1}	[124]
ATLAS & CMS	$t\bar{t} \to b\ell\nu q\gamma$		3.6×10^{-5}	10 fb^{-1}	[90] †
	$t\bar{t} \to b\ell\nu q\gamma$		1.0×10^{-5}	100 fb^{-1}	
$t \to qZ$:					
ATLAS	$t\bar{t} \to b\ell\nu q\ell\ell$	4.7×10^{-4}		10 fb^{-1}	[97]
	$t\bar{t} \to bqqq\ell\ell$	1.7×10^{-3}		10 fb^{-1}	
	comb.	4.5×10^{-4}		10 fb^{-1}	
ATLAS	$t\bar{t} \to b\ell\nu q\ell\ell$	1.1×10^{-4}	6.3×10^{-5}	100 fb^{-1}	[91]
	$t\bar{t} \to bqqq\ell\ell$	5.0×10^{-4}	2.7×10^{-4}	100 fb^{-1}	
	comb.		5.5×10^{-5}	100 fb^{-1}	
ATLAS	$t \to q\ell\ell$ (t-channel)	2.4×10^{-2}	8.5×10^{-3}	10 fb^{-1}	[98] †
CMS	$t\bar{t} \to b\ell\nu q\ell\ell$	1.5×10^{-3}		10 fb^{-1}	[124]
ATLAS & CMS	$t\bar{t} \to b\ell\nu q\ell\ell$		2.0×10^{-4}	10 fb^{-1}	[90] †
	$t\bar{t} \to b\ell\nu q\ell\ell$		4.2×10^{-5}	100 fb^{-1}	
$t \to qg$:					
ATLAS	$tt \to b\ell\nu b\ell\nu$ (same sign)		7.4×10^{-3}	100 fb^{-1}	[119, 120]
ATLAS	$qg \to b\ell\nu$ (direct prod.)		5.2×10^{-3}	100 fb^{-1}	[121]
ATLAS	$qg \to b\ell\nu$ (direct prod.)	2.6×10^{-4}	8.7×10^{-5}	10 fb^{-1}	[122, 123]
	$ug \to b\ell\nu$ (direct prod.)	1.8×10^{-4}	5.8×10^{-5}	10 fb^{-1}	
	$cg \to b\ell\nu$ (direct prod.)	5.2×10^{-4}	1.7×10^{-4}	10 fb^{-1}	

Table 5.2: The previous results from the cut-based analyses performed by the ATLAS and CMS collaborations are shown. The combination between the results of the ATLAS analyses described here and the ones from CMS, as well the results from the single top quark production (t-channel) with FCNC decays are also presented and are marked with daggers (†).

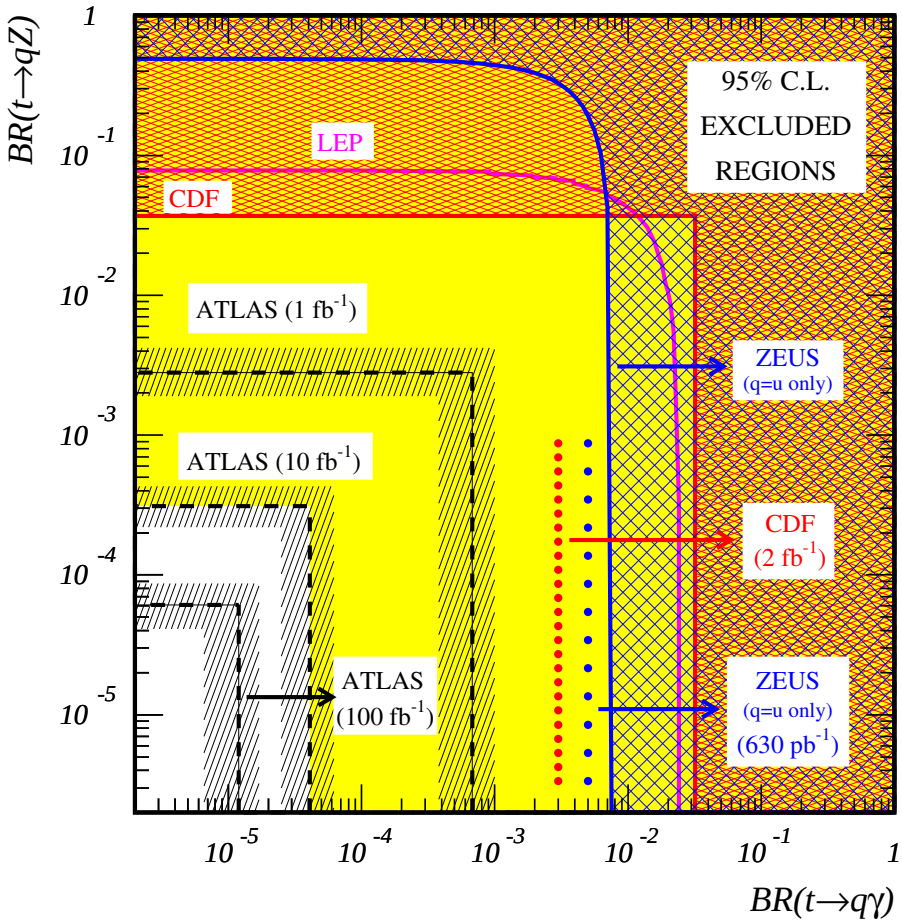

Figure 5.1: The present 95% CL observed limits on the $BR(t \to q\gamma)$ vs. $BR(t \to qZ)$ plane are shown as full lines for the LEP, ZEUS and CDF collaborations. The expected sensitivity at the HERA, Tevatron and ATLAS (together with the statistic plus systematic $\pm 1\sigma$ band) is also represented by the dotted and dashed lines.

the absence of signal (presented in this study), for the $t \to q\gamma$ and $t \to qZ$ channels taking into account the contribution from the statistical plus the systematic uncertainties. Present experimental limits from LEP, HERA and Tevatron (as well the expected sensitivity at the HERA [125] and Tevatron [126]) on the branching ratios of the FCNC top quark decays are also presented in the plot.

5.3 Future improvements

The analyses described here may be improved if new methods using Multivariate Data Analysis are used. H-Matrix and Fisher discriminants, Artificial Neural Networks or Boosted Decision Trees are such examples. Since the analyses with and without b-tag have similar performances, the inclusion of b-tag information in the χ^2 method (without cutting on the b-jet multiplicity) may also improve the results. With data, normalising the BR to measured processes may reduce the contribution from the luminosity and the absolute value of background

level to the systematic uncertainties.

Studies involving top quark FCNC vertices in single top quark production in the framework of [127, 128, 129, 130] were also initiated. Preliminary results suggest that the ATLAS sensitivity is of the same order of magnitude of the one obtained from the direct single top production study [122, 123]. Another interesting channel to study would be the $t \to qH$, for which only one analysis [131] is known.

6

Conclusions

The study of the ATLAS experience, at the LHC, sensitivity to the FCNC top quark decays was performed for high (10 fb^{-1} and 100 fb^{-1}) and low luminosities (1 fb^{-1}). The $t \to q\gamma$, $t \to qZ$ and $t \to qg$ decay channels were considered. The analyses for high luminosity took advantage of the ATLAS fast simulation in order to generate large samples, which makes possible the accurate study of systematic uncertainties. For the low luminosity, the full simulation was chosen and thus the effects of object identification criteria, efficiency and mistag, were studied and included in the analyses. Due to computational restrictions, the full simulation samples had only about three million events, a statistics about three hundred times smaller than the events in the fast simulation samples.

Cut-based analyses, followed by a likelihood-based analyses, were developed. Two different methods to reconstruct the event kinematics, with and without b-tagging, were tested and compared. After the final selection level, the signal efficiencies range between 1.1% and 7.6% and, in general, the dominant background comes from the $t\bar{t}$ and the W+jets contributions.

The results were interpreted under two different hypotheses: a 5σ significance discovery and an absence of signal (95% CL limits). The values of the 95% CL limits on the FCNC BR, computed with the MFL method (which takes into account the shape of the discriminant variables), range between 10^{-3} and 10^{-5} for a integrated luminosity of 10 fb^{-1}. The expected limits for the 1 fb^{-1} are compatible with these, if the differences in luminosities, in lepton and photon identification efficiencies, in trigger efficiencies and in background cross sections are taken into account. The total contributions of the studied systematic uncertainties are of the same order of magnitude of the statistical $\pm 1\sigma$ bands. The BR sensitivity for each FCNC channel, assuming a signal discovery with a 5σ significance, is on average 2.6 times larger than the absence of signal 95% CL limits.

The performance of the analysis for the $t \to q\gamma$ channel presented here is higher than the others from ATLAS and CMS, while for the $t \to qZ$ channel it is similar. For the other studied channel, this is the first analysis available on the $t\bar{t}$ production followed by the FCNC $t \to qg$ decay. With 10 fb^{-1}, the expected result is about one order of magnitude better than the current limit from Tevatron, although the results from the FCNC single top production analyses could be even better. The analyses may perform better if new MVA techniques are explored or if b-tag is incorporated in the new kinematics reconstruction method.

Even if the SM predicts a much lower BR for the FCNC decays of the top quark than the ones that can be measured at LHC, the expected BR obtained in these analyses are several orders of magnitude better than the present experimental limits, and with 100 fb^{-1} (one year of

data taking during the high luminosity LHC phase) some extensions of the SM can be probed.

The results obtained in this work were presented in several workshops and conferences [132, 133, 134, 135, 90, 136, 137]. They were published in ATLAS reports [89, 102] and in an international scientific journal [91], all with peer review.

A

Details of the comparison between high and low luminosities results

In order to compare the limits for the high (L = 10 fb^{-1} and L = 100 fb^{-1}) and low (L = 1 fb^{-1}) luminosity analyses, the differences in luminosities, lepton and photon identification efficiencies, trigger efficiencies, mistag and background cross-sections must be taken into account. The corrections are based on expression 3.11. Details are given below for each FCNC channel.

$t \to q\gamma$ channel

For the $t \to q\gamma$ channel the correction factors are the following. The statistical factor induced by the different luminosities is

$$\epsilon_{\text{lum.}} = \sqrt{\frac{1}{10}}. \tag{A.1}$$

In the fast simulation, no identification efficiency was applied to photons. Using the value shown in Table 4.5, the factor is

$$\epsilon_{\gamma} = \sqrt{\frac{0.666}{1}}. \tag{A.2}$$

The charged lepton efficiencies considered in the fast simulation are different from the ones obtain with the full simulation. Averaging the numbers presented in Table 4.5 for electrons and muons, the correction factor is given by:

$$\epsilon_{\ell} = \sqrt{\frac{0.8535}{0.9}}. \tag{A.3}$$

From Table 4.12, it can be seen that the trigger efficiency is not relevant for this FCNC channel. The effect of the charged leptons and photons mistags in the background estimation, can be evaluated by repeating the analysis presented in Chapter 4 using the fast simulation of the same events, which predicts 160±57 events for 1 fb^{-1}. In order to avoid the double counting of the identification efficiency of photons and leptons, the number of expected background events obtained with the full simulation must be deconvoluted. The correction factor is then:

$$\epsilon_{\text{mistag}}^{\text{back.}} = \sqrt{\frac{160}{\frac{650}{0.666\times 0.8535}}}. \tag{A.4}$$

The effect from the different cross-sections (and generated phase-space) used to evaluate the background contribution, can be estimated by comparing the predicted number of events shown in Chapter 3 with the ones obtained with the fast simulation of the same events used in Chapter 4 but analysed as those of Chapter 3 and corrected by the luminosity factor (for 1 fb^{-1}, 19.0±54 background events are expected):

$$\epsilon_{\sigma}^{\text{back.}} = \sqrt{\frac{318}{19 \times 10}}. \tag{A.5}$$

The total factor is then given by:

$$\epsilon_{\text{tot.}} = \epsilon_{\text{lum.}} \times \epsilon_{\gamma} \times \epsilon_{\ell} \times \epsilon_{\text{mistag}}^{\text{back.}} \times \epsilon_{\sigma}^{\text{back.}} = 0.122\,. \tag{A.6}$$

$t \to qZ$ channel

The correction factors for the $t \to qZ$ channel are the following ones. The statistical factor is the same as for the $t \to q\gamma$ channel. The correction factor from the charged lepton efficiencies is:

$$\epsilon_{\ell} = \sqrt{\frac{0.8535^3}{0.9^3}}. \tag{A.7}$$

The correction factor related to the trigger is (*c.f.* Table 4.12):

$$\epsilon_{\text{trigger}} = \sqrt{\frac{0.97}{1}}. \tag{A.8}$$

Using the fast simulation of the events of Chapter 4, 47±55 background events are expected for 1 fb^{-1}. Thus, the factor associated to the effect of the charged leptons and photons mistags in the background estimation is:

$$\epsilon_{\text{mistag}}^{\text{back.}} = \sqrt{\frac{47}{\frac{125}{0.8535^3 \times 0.97}}}. \tag{A.9}$$

The effect from the different cross-sections and generated phase-space in the background estimation is (64±55 background events are expected by the analysis of Chapter 3 using the fast simulation of the events of Chapter 4):

$$\epsilon_{\sigma}^{\text{back.}} = \sqrt{\frac{454}{64 \times 10}}. \tag{A.10}$$

The total factor is then given by:

$$\epsilon_{\text{tot.}} = \epsilon_{\text{lum.}} \times \epsilon_{\ell} \times \epsilon_{\text{trigger}} \times \epsilon_{\text{mistag}}^{\text{back.}} \times \epsilon_{\sigma}^{\text{back.}} = 0.115\,. \tag{A.11}$$

$t \to qg$ channel

For the $t \to qg$ channel the corrections factors for the luminosity and charged lepton efficiencies are the same as for the $t \to q\gamma$ channel. For the trigger, the correction factor is:

$$\epsilon_{\text{trigger}} = \sqrt{\frac{0.83}{1}}. \tag{A.12}$$

The factor associated to the effect of the charged leptons and photons mistags in the background estimation is (17943±342 background events are expected using the fast simulation of the events of Chapter 4):

$$\epsilon_{\text{mistag}}^{\text{back.}} = \sqrt{\frac{17943}{\frac{19252}{0.8535\times 0.83}}}. \tag{A.13}$$

The effect from the different cross-sections and generated phase-space in the background estimation is (1313±94 background events are expected by the analysis of Chapter 3 using the fast simulation of the events of Chapter 4):

$$\epsilon_{\sigma}^{\text{back.}} = \sqrt{\frac{8166}{1313\times 10}}. \tag{A.14}$$

The total factor is then given by:

$$\epsilon_{\text{tot.}} = \epsilon_{\text{lum.}} \times \epsilon_{\ell} \times \epsilon_{\text{trigger}} \times \epsilon_{\text{mistag}}^{\text{back.}} \times \epsilon_{\sigma}^{\text{back.}} = 0.180\,. \tag{A.15}$$

Bibliography

[1] **Particle Data Group** Collaboration, W. M. Yao *et. al.*, *Review of particle physics*, *J. Phys.* **G33** (2006) 1–1232.

[2] S. L. Glashow, *Partial Symmetries of Weak Interactions*, *Nucl. Phys.* **22** (1961) 579–588.

[3] A. Salam, "Weak and Electromagnetic Interactions." Originally printed in Svartholm: Elementary Particle Theory, Proceedings Of The Nobel Symposium Held 1968 At Lerum, Sweden, Stockholm, 1968.

[4] S. Weinberg, *A Model of Leptons*, *Phys. Rev. Lett.* **19** (1967) 1264–1266.

[5] G. Zweig, "An SU(3) model for strong interaction symmetry and its breaking." CERN-TH-401, 1964.

[6] F. Halzen and A. D. Martin, *Quarks and Leptons: An Introductory Course in Modern Particle Physics*. New York, Usa: Wiley, 1984.

[7] **Super-Kamiokande** Collaboration, S. Fukuda *et. al.*, *Determination of solar neutrino oscillation parameters using 1496 days of Super-Kamiokande-I data*, *Phys. Lett.* **B539** (2002) 179–187 [hep-ex/0205075].

[8] **K2K** Collaboration, M. H. Ahn *et. al.*, *Indications of neutrino oscillation in a 250-km long- baseline experiment*, *Phys. Rev. Lett.* **90** (2003) 041801 [hep-ex/0212007].

[9] **SNO** Collaboration, S. N. Ahmed *et. al.*, *Measurement of the total active B-8 solar neutrino flux at the Sudbury Neutrino Observatory with enhanced neutral current sensitivity*, *Phys. Rev. Lett.* **92** (2004) 181301 [nucl-ex/0309004].

[10] **KamLAND** Collaboration, K. Eguchi *et. al.*, *First results from KamLAND: Evidence for reactor anti- neutrino disappearance*, *Phys. Rev. Lett.* **90** (2003) 021802 [hep-ex/0212021].

[11] M. C. Gonzalez-Garcia and M. Maltoni, *Phenomenology with Massive Neutrinos*, *Phys. Rept.* **460** (2008) 1–129 [0704.1800].

[12] M. Kobayashi and T. Maskawa, *CP Violation in the Renormalizable Theory of Weak Interaction*, *Prog. Theor. Phys.* **49** (1973) 652–657.

[13] S. L. Glashow, J. Iliopoulos and L. Maiani, *Weak Interactions with Lepton-Hadron Symmetry*, *Phys. Rev.* **D2** (1970) 1285–1292.

[14] **LEP** Collaboration, G. Alexander *et. al.*, *Electroweak parameters of the Z0 resonance and the Standard Model: the LEP Collaborations*, *Phys. Lett.* **B276** (1992) 247–253.

[15] **CDF** Collaboration, F. Abe *et. al.*, *Observation of top quark production in $\bar{p}p$ collisions*, *Phys. Rev. Lett.* **74** (1995) 2626–2631 [hep-ex/9503002].

[16] **DØ** Collaboration, S. Abachi *et. al.*, *Observation of the top quark*, *Phys. Rev. Lett.* **74** (1995) 2632–2637 [hep-ex/9503003].

[17] J. F. Donoghue, E. Golowich and B. R. Holstein, *Dynamics of the Standard Model*, vol. 2. Camb. Monogr. Part. Phys. Nucl. Phys. Cosmol., 1992.

[18] W. Bernreuther, *Top quark physics at the LHC*, *J. Phys.* **G35** (2008) 083001 [0805.1333].

[19] **Tevatron Electroweak Working Group** for the CDF and DØ Collaborations, *A Combination of CDF and D0 Results on the Mass of the Top Quark*, 0803.1683.

[20] **CDF** Collaboration, "Combination of CDF top quark pair production cross section measurements with up to 760 pb^{-1}." Conf. Note 8148, 2006.

[21] **DØ** Collaboration, V. M. Abazov *et. al.*, *Measurement of the ttbar production cross section in ppbar collisions at sqrts = 1.96 TeV*, *Phys. Rev. Lett.* **100** (2008) 192004 [0803.2779].

[22] **CDF** Collaboration, "A Limit on the Top Quark Width and the Lifetime using the Template Method in the Lepton plus Jets Channel at CDF II." Conf. Note 8953, 2007.

[23] **CDF** Collaboration, "First direct limit on the top quark lifetime." Conf. Note 8104, 2006.

[24] **CDF** Collaboration, D. E. Acosta *et. al.*, *Measurement of $B(t \to Wb)/B(t \to Wq)$ at the Collider Detector at Fermilab*, *Phys. Rev. Lett.* **95** (2005) 102002 [hep-ex/0505091].

[25] **CDF** Collaboration, "First CDF Measurement of the Top Quark Charge using the Top Decay Products." Conf. Note 8967, 2007.

[26] **DØ** Collaboration, V. M. Abazov *et. al.*, *Experimental discrimination between charge $2e/3$ top quark and charge $4e/3$ exotic quark production scenarios*, *Phys. Rev. Lett.* **98** (2007) 041801 [hep-ex/0608044].

[27] **CDF** Collaboration, "Measurement of W-Boson Helicity Fractions in Top-Quark Decays Using $\cos\theta^*$." Conf. Note 9215, 2007.

[28] **DØ** Collaboration, V. M. Abazov *et. al.*, *Model-independent measurement of the W boson helicity in top quark decays*, *Phys. Rev. Lett.* **100** (2008) 062004 [0711.0032].

[29] J. L. Diaz-Cruz, R. Martinez, M. A. Perez and A. Rosado, *Flavour changing radiative decay of the t quark*, *Phys. Rev.* **D41** (1990) 891–894.

[30] G. Eilam, J. L. Hewett and A. Soni, *Rare decays of the top quark in the standard and two Higgs doublet models*, *Phys. Rev.* **D44** (1991) 1473–1484. Erratum-ibid.D59:039901,1999.

[31] B. Mele, S. Petrarca and A. Soddu, *A new evaluation of the $t \to cH$ decay width in the standard model*, *Phys. Lett.* **B435** (1998) 401–406 [hep-ph/9805498].

[32] J. A. Aguilar-Saavedra and B. M. Nobre, *Rare top decays $t \to c\gamma, t \to cg$ and CKM unitarity*, *Phys. Lett.* **B553** (2003) 251–260 [hep-ph/0210360].

[33] M. Beneke *et. al.*, *Top quark physics, in: Proceedings of the "1999 CERN Workshop on SM physics (and more) at the LHC*, hep-ph/0003033.

[34] J. A. Aguilar-Saavedra, *Top flavour-changing neutral interactions: Theoretical expectations and experimental detection*, *Acta Phys. Polon.* **B35** (2004) 2695–2710 [hep-ph/0409342].

[35] F. del Aguila, J. A. Aguilar-Saavedra and R. Miquel, *Constraints on top couplings in models with exotic quarks*, *Phys. Rev. Lett.* **82** (1999) 1628–1631 [hep-ph/9808400].

[36] J. A. Aguilar-Saavedra, *Effects of mixing with quark singlets*, *Phys. Rev.* **D67** (2003) 035003 [hep-ph/0210112]. Erratum-ibid. D **69** (2004) 099901.

[37] T. P. Cheng and M. Sher, *Mass Matrix Ansatz and Flavor Nonconservation in Models with Multiple Higgs Doublets*, *Phys. Rev.* **D35** (1987) 3484.

[38] B. Grzadkowski, J. F. Gunion and P. Krawczyk, *Neutral current flavor changing decays for the Z boson and the top quark in two Higgs doublet models*, *Phys. Lett.* **B268** (1991) 106–111.

[39] M. E. Luke and M. J. Savage, *Flavor changing neutral currents in the Higgs sector and rare top decays*, *Phys. Lett.* **B307** (1993) 387–393 [hep-ph/9303249].

[40] D. Atwood, L. Reina and A. Soni, *Probing flavor changing top - charm - scalar interactions in e+ e- collisions*, *Phys. Rev.* **D53** (1996) 1199–1201 [hep-ph/9506243].

[41] D. Atwood, L. Reina and A. Soni, *Phenomenology of two Higgs doublet models with flavor changing neutral currents*, *Phys. Rev.* **D55** (1997) 3156–3176 [hep-ph/9609279].

[42] S. Bejar, J. Guasch and J. Sola, *Loop induced flavor changing neutral decays of the top quark in a general two-Higgs-doublet model*, *Nucl. Phys.* **B600** (2001) 21–38 [hep-ph/0011091].

[43] C. S. Li, R. J. Oakes and J. M. Yang, *Rare decay of the top quark in the minimal supersymmetric model*, *Phys. Rev.* **D49** (1994) 293–298. Erratum-ibid.D56:3156,1997.

[44] G. M. de Divitiis, R. Petronzio and L. Silvestrini, *Flavour changing top decays in supersymmetric extensions of the standard model*, *Nucl. Phys.* **B504** (1997) 45–60 [hep-ph/9704244].

[45] J. L. Lopez, D. V. Nanopoulos and R. Rangarajan, *New supersymmetric contributions to $t \to cV$*, *Phys. Rev.* **D56** (1997) 3100–3106 [hep-ph/9702350].

[46] J. Guasch and J. Sola, *FCNC top quark decays: A door to SUSY physics in high luminosity colliders?*, *Nucl. Phys.* **B562** (1999) 3–28 [hep-ph/9906268].

[47] D. Delepine and S. Khalil, *Top flavour violating decays in general supersymmetric models*, *Phys. Lett.* **B599** (2004) 62–74 [hep-ph/0406264].

[48] J. J. Liu, C. S. Li, L. L. Yang and L. G. Jin, *$t \to cV$ via SUSY FCNC couplings in the unconstrained MSSM*, *Phys. Lett.* **B599** (2004) 92–101 [hep-ph/0406155].

[49] J. J. Cao *et. al.*, *SUSY-induced FCNC top-quark processes at the Large Hadron Collider*, *Phys. Rev.* **D75** (2007) 075021 [hep-ph/0702264].

[50] J. M. Yang, B.-L. Young and X. Zhang, *Flavor-changing top quark decays in R-parity violating SUSY*, *Phys. Rev.* **D58** (1998) 055001 [hep-ph/9705341].

[51] G. Eilam, A. Gemintern, T. Han, J. M. Yang and X. Zhang, *Top quark rare decay $t \to ch$ in R-parity-violating SUSY*, *Phys. Lett.* **B510** (2001) 227–235 [hep-ph/0102037].

[52] G. Lu, F. Yin, X. Wang and L. Wan, *The rare top quark decays $t \to cV$ in the topcolor-assisted technicolor model*, *Phys. Rev.* **D68** (2003) 015002 [hep-ph/0303122].

[53] C. Caso *et. al. Eur. Phys. J. C* **3** (1998) 1.

[54] W. Hollik, J. I. Illana, S. Rigolin, C. Schappacher and D. Stockinger *Nucl. Phys. B* **551** (1999) 3.

[55] **ALEPH** Collaboration, A. Heister *et. al.*, *Search for single top production in e+ e- collisions at s**(1/2) up to 209-GeV*, *Phys. Lett.* **B543** (2002) 173–182 [hep-ex/0206070].

[56] **DELPHI** Collaboration, J. Abdallah *et. al.*, *Search for single top production via FCNC at LEP at s**(1/2) = 189-GeV - 208-GeV*, *Phys. Lett.* **B590** (2004) 21–34 [hep-ex/0404014].

[57] **OPAL** Collaboration, G. Abbiendi *et. al.*, *Search for single top quark production at LEP2*, *Phys. Lett.* **B521** (2001) 181–194 [hep-ex/0110009].

[58] **L3** Collaboration, P. Achard *et. al.*, *Search for single top production at LEP*, *Phys. Lett.* **B549** (2002) 290–300 [hep-ex/0210041].

[59] The LEP Exotica WG, *Search for single top production via flavour changing neutral currents: preliminary combined results of the LEP experiments*, LEP Exotica WG 2001-01.

[60] **ZEUS** Collaboration, S. Chekanov *et. al.*, *Search for single-top production in e p collisions at HERA*, *Phys. Lett.* **B559** (2003) 153–170 [hep-ex/0302010].

[61] **CDF Collaboration** Collaboration, "Search for the Flavor Changing Neutral Current Decay $t \to Zq$ in $p\bar{p}$ Collisions at $\sqrt{s} = 1.96$ TeV with 1.9 fb^{-1} of CDF-II Data." Conf. Note 9202, 2008.

[62] **CDF** Collaboration, F. Abe *et. al.*, *Search for flavor-changing neutral current decays of the top quark in $p\bar{p}$ collisions at $\sqrt{s} = 1.8$ TeV*, *Phys. Rev. Lett.* **80** (1998) 2525–2530.

[63] A. A. Ashimova and S. R. Slabospitsky, *The constraint on FCNC coupling of the top quark with a gluon from e p collisions*, *hep-ph/0604119* (2006).

[64] **H1** Collaboration, A. Aktas *et. al.*, *Search for single top quark production in ep collisions at HERA*, *Eur. Phys. J.* **C33** (2004) 9–22 [hep-ex/0310032].

[65] **DØ** Collaboration, V. M. Abazov *et. al.*, *Search for production of single top quarks via flavor- changing neutral currents at the Tevatron*, *Phys. Rev. Lett.* **99** (2007) 191802 [hep-ex/0702005].

[66] R. P. Feynman, "The behavior of hadron collisions at extreme energies." Invited paper at the Third Conference on High-Energy Collisions, Stony Brook, New York, 5-6 Sep 1969.

[67] M. Dittmar *et. al.*, *Parton distributions: Summary report for the HERA - LHC workshop*, hep-ph/0511119.

[68] **H1** Collaboration, N. Raicevic, *Structure functions and extraction of PDFs at HERA*, hep-ex/0605050.

[69] **H1** Collaboration, K. Wichmann, *Recent Results from HERA Experiments*, 0707.2724.

[70] J. Pumplin *et. al.*, *New generation of parton distributions with uncertainties from global QCD analysis*, *JHEP* **0207** (2002) 012 [hep-ph/0201195].

[71] R. Bonciani, S. Catani, M. L. Mangano and P. Nason, *NLL resummation of the heavy-quark hadroproduction cross- section*, *Nucl. Phys.* **B529** (1998) 424–450 [hep-ph/9801375].

[72] N. Kidonakis and R. Vogt, *Next-to-next-to-leading order soft-gluon corrections in top quark hadroproduction*, *Phys. Rev.* **D68** (2003) 114014 [hep-ph/0308222].

[73] S. Moch and P. Uwer, *Theoretical status and prospects for top-quark pair production at hadron colliders*, *Phys. Rev.* **D78** (2008) 034003 [0804.1476].

[74] M. Cacciari, S. Frixione, M. L. Mangano, P. Nason and G. Ridolfi, *Updated predictions for the total production cross sections of top and of heavier quark pairs at the Tevatron and at the LHC*, *JHEP* **09** (2008) 127 [0804.2800].

[75] Z. Sullivan, *Understanding single-top-quark production and jets at hadron colliders*, *Phys. Rev.* **D70** (2004) 114012 [hep-ph/0408049].

[76] J. Campbell and F. Tramontano, *Next-to-leading order corrections to W t production and decay*, *Nucl. Phys.* **B726** (2005) 109–130 [hep-ph/0506289].

[77] E. S. Swanson, *Aspects of confinement: A brief review*, *AIP Conf. Proc.* **717** (2004) 636–645 [hep-ph/0310089].

[78] B. R. Webber, *Fragmentation and hadronization*, hep-ph/9912292.

[79] G. Marchesini and B. R. Webber, *Simulation of QCD Jets Including Soft Gluon Interference*, *Nucl. Phys.* **B238** (1984) 1.

[80] G. Marchesini and B. R. Webber, *Monte Carlo Simulation of General Hard Processes with Coherent QCD Radiation*, *Nucl. Phys.* **B310** (1988) 461.

[81] B. Andersson, G. Gustafson, G. Ingelman and T. Sjostrand, *Parton Fragmentation and String Dynamics*, *Phys. Rept.* **97** (1983) 31–145.

[82] J. M. Campbell, J. W. Huston and W. J. Stirling, *Hard interactions of quarks and gluons: A primer for LHC physics*, *Rept. Prog. Phys.* **70** (2007) 89 [hep-ph/0611148].

[83] Bruning, O. (Ed.) *et. al.*, *LHC design report. Vol. I: The LHC main ring*, CERN-2004-003-V-1.

[84] Buning, O. (Ed.) *et. al.*, *LHC Design Report. 2. The LHC infrastructure and general services*, CERN-2004-003-V-2.

[85] Benedikt, M. (Ed.) *et. al.*, *LHC Design Report. 3. The LHC injector chain*, CERN-2004-003-V-3.

[86] **ATLAS** Collaboration, *ATLAS detector and physics performance: Technical Design Report, 1*. Technical Design Report ATLAS. CERN, Geneva, 1999. CERN-LHCC-99-014, ATLAS-TDR-014.

[87] **ATLAS** Collaboration, *The ATLAS Experiment at the CERN Large Hadron Collider*, ATL-COM-PHYS-2007-102. submitted to JINST.

[88] K. Kordas *et. al.*, *The ATLAS Data Acquisition and Trigger: Concept, design and status*, *Nucl. Phys. Proc. Suppl.* **172** (2007) 178–182. ATL-DAQ-CONF-2007-022.

[89] J. Carvalho, N. Castro, A. Onofre and F. Veloso, *Study of ATLAS sensitivity to FCNC top decays*, Tech. Rep. ATL-PHYS-PUB-2005-009. ATL-COM-PHYS-2005-023, CERN, Geneva, 2005.

[90] F. del Aguila *et. al.*, *Collider aspects of flavour physics at high Q*, 0801.1800.

[91] J. Carvalho *et. al.*, *Study of ATLAS sensitivity to FCNC top decays*, *Eur. Phys. J. C* **52** (2007) 999–1019 [0712.1127].

[92] S. R. Slabospitsky and L. Sonnenschein, *TopReX generator (version 3.25): Short manual*, *Comput. Phys. Commun.* **148** (2002) 87–102 [hep-ph/0201292].

[93] T. Sjostrand, L. Lonnblad and S. Mrenna, *PYTHIA 6.2: Physics and manual*, hep-ph/0108264.

[94] **CTEQ** Collaboration, H. L. Lai *et. al.*, *Global QCD analysis of parton structure of the nucleon: CTEQ5 parton distributions*, *Eur. Phys. J.* **C12** (2000) 375–392 [hep-ph/9903282].

[95] H. L. Lai *et. al.*, *Improved parton distributions from global analysis of recent deep inelastic scattering and inclusive jet data*, *Phys. Rev.* **D55** (1997) 1280–1296 [hep-ph/9606399].

[96] E. Richter-Was, D. Froidevaux and L. Poggioli, *ATLFAST 2.0 a fast simulation package for ATLAS*, Tech. Rep. ATL-PHYS-98-131, CERN, Geneva, Nov, 1998.

[97] J. Dodd, S. McGrath and J. Parsons, *Study of ATLAS Sensitivity to Rare Top Quark Decays*, Tech. Rep. ATL-PHYS-2003-016. ATL-COM-PHYS-99-039, CERN, Geneva, May, 1999.

[98] J. Carvalho, N. Castro, A. Onofre and F. Veloso, *Study of the ATLAS sensitivity to FCNC decays in single top events*, Tech. Rep. ATL-PHYS-PUB-2005-026. ATL-COM-PHYS-2005-059, CERN, Geneva, Oct, 2005.

[99] **Particle Data Group** Collaboration, S. Eidelman *et. al.*, *Review of particle physics*, *Phys. Lett. B* **592** (2004) 1.

[100] P. Gonçalves, *Test of QED and Search for New Physics in Multi-Photonic Final States at LEP2*. PhD thesis, Instituto Superior Técnico.

[101] A. L. Read, *Modified frequentist analysis of search results (The CL(s) method)*, CERN-OPEN-2000-205. Prepared for Workshop on Confidence Limits, Geneva, Switzerland, 17-18 Jan 2000.

[102] **ATLAS** Collaboration, *Expected Performance of the ATLAS Experiment, Detector, Trigger and Physics*, Tech. Rep. CERN-OPEN-2008-020, CERN, Geneva, 2008. to appear.

[103] **ATLAS** Collaboration, *The ATLAS Computing Workbook (ATHENA 12.0.6)*, . https://twiki.cern.ch/twiki/bin/view/Atlas/WorkBook.

[104] T. Sjostrand, S. Mrenna and P. Skands, *PYTHIA 6.4 physics and manual*, *JHEP* **05** (2006) 026 [hep-ph/0603175].

[105] M. L. Mangano *et. al.*, *Alpgen, a generator for hard multiparton processes in hadronic collisions*, *JHEP0307* (2003) 001.

[106] G. Corcella *et. al.*, *HERWIG 6.5: an event generator for hadron emission reactions with interfering gluons (including supersymmetric processes)*, *JHEP0101* (2001) 010.

[107] S. Frixione and B. Webber, *The MCatNLO 3.1 Event Generator*, *hep-ph/0506182* (2005).

[108] J. M. Butterworth and J. R. Forshaw, *Photoproduction of multi-jet events at HERA: A Monte Carlo simulation*, *J. Phys.* **G19** (1993) 1657–1663.

[109] J. M. Butterworth, J. R. Forshaw and M. H. Seymour, *Multiparton interactions in photoproduction at HERA*, *Z. Phys.* **C72** (1996) 637–646 [hep-ph/9601371].

[110] B. Kersevan and R. Elzbieta, *The Monte Carlo Event Generator AcerMC version 3.4 with interfaces to PYTHIA 6.3, HERWIG 6.5 and ARIADNE 4.1*, *hep-ph/0405247* (2004).

[111] P. Golonka *et. al.*, *The tauola-photos-F environment for the TAUOLA and PHOTOS packages, release II*, *Comput. Phys. Commun.* **174** (2006) 818–835 [hep-ph/0312240].

[112] C. B. A. Moraes and I. Dawson, *Prediction for Minimum Bias and the Underlying Event at LHC Energies*, *ATL-PHYS-PUB-2005-007* (2005).

[113] P. Perrodo, *Commissioning of the ATLAS detector and combined beam test results*, *Nucl. Instrum. Meth.* **A572** (2007) 113–116.

[114] ATLAS collaboration, *ATLAS Computing Technical Design Report*. Technical Design Report ATLAS. CERN, Geneva, 2005. CERN-LHCC-2005-022, ATLAS-TDR-017.

[115] A. Shibata, *TopView - ATLAS top physics analysis package*, Tech. Rep. ATL-SOFT-PUB-2007-002, ATLAS Collaboration, CERN, Geneva, 2007.

[116] A. Shibata, *Investigation of Electroweak Production of the Top Quark at the LHC*. PhD thesis, London, Queen Mary University of London, 2007.

[117] K. Cranmer, A. Farbin and A. Shibata, *EventView - The Design Behind an Analysis Framework*, Tech. Rep. ATL-SOFT-PUB-2007-008, ATLAS Collaboration, CERN, Geneva, 2007.

[118] R. Brun and F. Rademakers, *ROOT: An object oriented data analysis framework*, *Nucl. Instrum. Meth.* **A389** (1997) 81–86. See also http://root.cern.ch/.

[119] Y. P. Gouz and S. R. Slabospitsky, *Double top production at hadronic colliders*, *Phys. Lett.* **B457** (1999) 177–185 [hep-ph/9811330].

[120] **ATLAS** Collaboration, *ATLAS detector and physics performance: Technical Design Report, 2*. Technical Design Report ATLAS. CERN, Geneva, 1999. CERN-LHCC-99-015, ATLAS-TDR-015.

[121] O. Cakir and S. A. Cetin, *Anomalous single top quark production at the CERN LHC*, *J. Phys. G* **31** (2005), no. SN-ATLAS-2004-046. 1 N1–N8. 10 p.

[122] T. L. Cheng and P. Teixeira-Dias, *Sensitivity of ATLAS to FCNC single top quark production*, Tech. Rep. ATL-PHYS-PUB-2006-029. ATL-COM-PHYS-2006-056, CERN, Geneva, Aug, 2006.

[123] T. L. Cheng, *Search for Anomalous Single Top Quark Production via Flavour-Changing Neutral Currents with the ATLAS Detector at the Large Hadron Collider*. PhD thesis, Royal Holloway, University of London.

[124] **CMS** Collaboration, G. L. Bayatian *et. al.*, *CMS technical design report, volume II: Physics performance*, *J. Phys.* **G34** (2007) 995–1579.

[125] L. Bellagamba. Private Communication.

[126] A. Juste, *Top quark current experimental status*, *PoS* **TOP2006** (2006) 007 [hep-ex/0603007]. Presentation available at http://nautilus.fis.uc.pt/personal/top2006/programme.shtml.

[127] P. M. Ferreira, O. Oliveira and R. Santos, *Flavour changing strong interaction effects on top quark physics at the LHC*, *Phys. Rev.* **D73** (2006) 034011 [hep-ph/0510087].

[128] P. M. Ferreira and R. Santos, *Strong flavour changing effective operator contributions to single top quark production*, *Phys. Rev.* **D73** (2006) 054025 [hep-ph/0601078].

[129] P. M. Ferreira and R. Santos, *Contributions from dimension six strong flavor changing operators to t anti-t, t plus gauge boson, and t plus Higgs boson production at the LHC*, *Phys. Rev.* **D74** (2006) 014006 [hep-ph/0604144].

[130] P. M. Ferreira, R. B. Guedes and R. Santos, *Combined effects of strong and electroweak FCNC effective operators in top quark physics at the LHC*, *Phys. Rev.* **D77** (2008) 114008 [0802.2075].

[131] L. Chikovani, T. Djobava and T. Grigalashvili, *The flavour-changing neutral currents decay $t \to Hq$ at ATLAS experiment*, ATL-COM-PHYS-2004-077, hep-ex/0505079.

[132] J. Carvalho *et. al.*, "Study of ATLAS sensitivity to FCNC top quark decays." Poster presented at "European School of High-Energy Physics", Kitzbühel, Austria, August 2005, 2005.

[133] J. Bastos, J. Carvalho, N. Castro, A. Onofre and F. Veloso, "Física do quark top na experiência ATLAS." Poster presented at "FÍSICA 2005 - Física para o Séc. XXI", Porto, December 2005, 2005.

[134] N. Castro *PoS* **TOP2006** (2006) 028. Proceedings of the *Top2006* Workshop, Coimbra, Portugal, January 2006.

[135] A. Onofre, *Testing the Standard Model in ttbar and single top production at the LHC*, ATL-PHYS-CONF-2007-004. Talk at *ICHEP 06* conference, Moscow, Russia, July 2006.

[136] F. Veloso, "Top quark properties: prospects at ATLAS." (proceedings of the *Top2008* Workshop, Isola d'Elba, Italy, May 2008; to be published in *Nuov. Cim.*), 2008.

[137] J. Carvalho, N. Castro, A. Onofre and F. Veloso, "Study of ATLAS sensitivity to FCNC top quark decays." (proceedings of the *Top2008* Workshop, Isola d'Elba, Italy, May 2008; to be published in *Nuov. Cim.*), 2008.